

TOPICAL REVIEW

# Nanocrystalline and nanocomposite permanent magnets by melt spinning technique

To cite this article: Chuanbing Rong and Baogen Shen 2018 *Chinese Phys. B* **27** 117502

View the [article online](#) for updates and enhancements.

# Nanocrystalline and nanocomposite permanent magnets by melt spinning technique\*

Chuanbing Rong(荣传兵)<sup>1,†</sup> and Baogen Shen(沈保根)<sup>2</sup>

<sup>1</sup>*Electric Machine and Drive system, Research and Innovation Center, Ford Motor Company, Dearborn, MI 48187, USA*

<sup>2</sup>*State Key Laboratory of Magnetism, Institute of Physics and University of Chinese Academy of Sciences, Chinese Academy of Sciences, Beijing 100190, China*

(Received 23 September 2018; published online 31 October 2018)

The melt-spinning technique offers an opportunity for tailoring magnetic properties by controlling the structures and microstructures in both single-phase and composite magnets. This review first broadly discusses the principle of cooling control, amorphization, crystallization, annealing, and consolidation of the melt-spun ribbons. The phase, microstructure, and magnetic properties of popular single-phase nanocrystalline magnets are reviewed, followed by the nanocomposite magnets consisting of magnetically hard and soft phases. The precipitation-hardened magnetic materials prepared by melt spinning are also discussed. Finally, the role of intergrain exchange coupling, thermal fluctuation, and reversible/irreversible magnetization processes are discussed and correlated to the magnetic phenomena in both single-phase and nanocomposite magnets.

**Keywords:** nanocrystalline magnets, nanocomposite magnets, melt-spinning technique

**PACS:** 75.50.Ww

**DOI:** 10.1088/1674-1056/27/11/117502

## 1. Melt-spinning technique

Melt spinning is a technique used for rapid cooling of molten liquids to produce metallic metastable solid solutions, which was introduced in 1960.<sup>[1,2]</sup> Both twin-roller and single-roller methods were introduced to produce rapidly solidified metallic ribbons, although the single-roller method is most widely used nowadays because of its simplicity and reproducibility. Figure 1 illustrates basic configuration of the single-roller melt-spinning apparatus. In a typical melt-spinning process, a rotating wheel is cooled internally, usually by water or high thermal conductive materials, such as copper. A thin stream of molten liquid is then dropped onto the surface of the rotating wheel. The heat of the molten liquid is absorbed into the roller rapidly and a cooling rate is on the order of  $10^4$ – $10^7$  K/s, which is large enough to prevent nucleation and growth of stable phases from crystallization for some materials. It should be noted that the cooling rate is not a linear function of time, which was confirmed through the measurement by utilizing a digital thermograph recording and analysis technique.<sup>[3]</sup>

The melt-spinning technique is widely used to develop materials that require extremely high cooling rates in order to form metallic glasses or materials with extremely small grains or nanocrystals. The structure of final products formed by melt-spinning depends on the cooling rate, which can be described by continuous cooling transformation (CCT) curves.<sup>[3]</sup>

Figure 2 schematically illustrates a CCT behavior for an amorphous-forming alloy and a composite alloy with crystallization processes on the time-temperature plot. For curve (a), the cooling rate is large enough to prevent any phase from crystallization and growth, therefore the rapidly solidified structure is amorphous. For curve (b), the rapidly solidified structure is a mixture of an amorphous phase and fine crystalline of phase A, because the cooling rate is not fast enough to form amorphous for phase A, but still quick enough for potential phase B. Curve (c) is the CCT behavior for a composite structure via a single quenching operation. The cooling rate must be carefully optimized in order to avoid unfavorable grain growth, which is a key to achieve the desired material properties for melt-spun ribbons.

The cooling rate of the melt-spinning process depends on the following factors: the thickness of the melt to be cooled, which is normally controlled by changing the revolution rate of the quenching roller; the pour rate of the molten alloy, which is normally controlled by the opening diameter of the ejecting nozzle and pressure; the heat transfer from the melt to the roller surface, which depends on interface energy between the melt and the roller surface, heat conductivity of the roller material, heat transfer between the roller and cooling water, and so on. After the rapidly quenched material leaves the rotating wheel, it is further cooled down by radiation and heat transfer to the surrounding gas, which is normally inert gas

\*\* Project supported by the National Natural Science Foundation of China (Grant No. 51590880) and the National Key Research and Development Program of China (Grant Nos. 2014CB643700 and 2016YFB070090).

† Corresponding author. E-mail: [crong@ford.com](mailto:crong@ford.com)

such as Ar or N<sub>2</sub> for air-sensitive materials. Therefore, all the above factors need to be considered when the experiment is designed and performed during the melt spinning process.

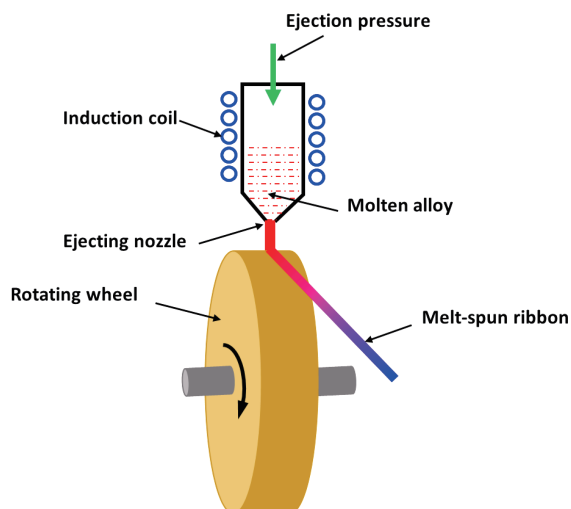


Fig. 1. (color online) Basic configuration of a single-roller melt-spinning apparatus.

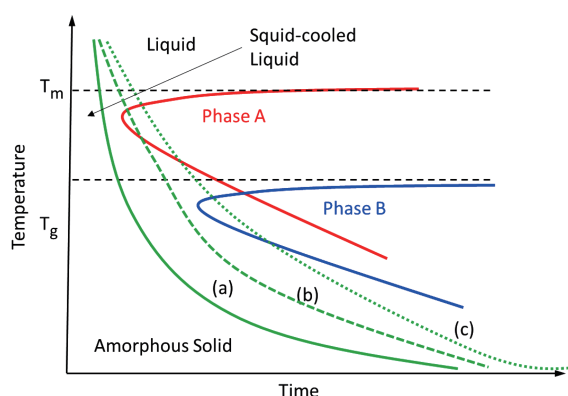


Fig. 2. (color online) Schematic illustration of CCT behaviors in melt-spinning process.  $T_m$  is melting point;  $T_g$  is glass-transition temperature.<sup>[3]</sup>

The commercial and technological interests of melt spinning have been initially paid to soft amorphous and nanocrystalline magnetic materials prior to hard magnetic materials. The first ferromagnetic melt-quenched glassy alloys Pd<sub>12</sub>Co<sub>68</sub>Si<sub>20</sub> were reported by Tsuei and Duwez.<sup>[4]</sup> The rapid quenched soft magnetic materials exhibit very low coercivity, which originates from the absence of magnetocrystalline anisotropy in these amorphous alloys.<sup>[5]</sup> Special attention has also been paid to the study of nanocrystalline phases obtained by suitable annealing of amorphous metallic ribbons. Such nanocrystalline magnetic materials exhibit excellent soft magnetic properties such as high saturated magnetization, high permeability, and low core loss simultaneously as the grain size below 10 nm, which was theoretically estimated by Herzer.<sup>[6]</sup> The melt-spinning technique is a great method to produce such nanocrystalline soft magnetic materials, and

thus leads to the successful development of Fe–Cu–Nb–Si–B alloys (a trade name of “FINEMET”).<sup>[7]</sup>

The application of melt spinning on producing permanent magnets began on the demand of reducing the particle size of polycrystalline permanent magnetic materials, where their coercivity,  $H_c$ , is strongly dependent on the size of particles or grains. It is often agreed that the coercivity increases with decreasing particle size as it approaches the single domain particle size. The two common ways to decrease particle size or grain size are ball-milling and melt-spinning processes. The ball milling route seems very attractive since it is a simple process and it may produce single crystals which can be aligned by a magnetic field. Unfortunately, the conventional milling method cannot produce particles smaller than 0.5–1  $\mu\text{m}$ . Moreover, the surface of the as-milled particles is very sensitive to air and thus having poor magnetic performance unless they are post-processed. A majority of contemporary nanocrystalline hard-magnetic materials are produced by the melt-spinning process, which is capable of producing both laboratory-scale and industrial-scale quantities of materials in the form of flakes or ribbons. The early studies on a nanoscale magnetically hard system using the melt-spinning process were made on RE–Fe–B alloys with large coercivity at room temperature, where RE represents rare earth elements such as Nd and Pr, right after the discovery of Nd–Fe–B magnets. The larger coercivity was due to the highly anisotropic 2:14:1 tetragonal phase, which was produced during melt spinning or after crystallization. It was found that coercivity of nanocrystalline RE<sub>2</sub>Fe<sub>14</sub>B-based alloys is much larger than that of the corresponding sintered magnets. For example, melt-spun Nd<sub>2</sub>Fe<sub>14</sub>B magnets can easily attain a coercivity of 1190 kA/m<sup>[8]</sup> whereas the coercivity of sintered magnets reaches only 960 kA/m.<sup>[9]</sup>

In addition to the superior of coercivity, the remanence is also enhanced in the isotropic nanocrystalline permanent magnet, which is known as remanence enhancement. Within the framework of the Stoner–Wohlfarth theory, the remanence is half of the saturated magnetization ( $M_s$ ), i.e.,  $M_r = M_s/2$ , or the normalized remanence  $M_r/M_s$  is  $1/2$ , for an assembly of non-interacting and randomly oriented single domain particles.<sup>[10]</sup> However, the intergrain exchange interaction in nanocrystalline magnets, even in single-phase magnets, usually leads to a  $M_r/M_s$  larger than  $1/2$ , i.e., remanence enhancement.<sup>[11]</sup> Numerical simulations show that a remanence could be enhanced by more than 40% as compared to the non-interacting particles if the grain size is in the order of 10–30 nm.<sup>[12]</sup>

The exchange interaction not only exists in single-phase nanocrystalline magnets, but also in nanocomposite magnets consisting of a magnetically hard phase such as Nd–Fe–B and

a magnetically soft phase such as  $\alpha$ -Fe. Actually, the inter-phase exchange interaction has bigger impacts on the remanence enhancement than the intergrain exchange interaction in single phase due to the low magnetocrystalline anisotropy of the magnetically soft phase. In the meantime, the inter-phase exchange interaction also prevents the reversal of the magnetic moments in the soft phase and thus retains a comparable coercivity to the original hard phase. This is the key idea of the nanocomposite permanent magnet which was proposed by Kneller and Hawig in 1991.<sup>[13]</sup> The theoretical prediction shows that the energy product of nanocomposite permanent magnet could be double compared to the theoretical limit of single-phase magnet.<sup>[14]</sup> Micromagnetic simulations confirm that the inter-phase exchange interaction could enhance the remanence with respect to non-interacting particles.<sup>[15–17]</sup> Extensive research has been devoted to this topic in the past 25 years for both experimental and numerical studies.

This article is organized as follows. Section 2 introduces the unique characteristics in melt-spun materials such as amorphization, crystallization, and consolidation. Section 3 reviews the melt-spun permanent magnetic materials including single-phase, nanocomposite and precipitation-hardening-type magnets. Section 4 discusses the magnetic phenomena in the melt-spun materials, including single-phase magnetic behavior, remanence enhancement, microstructure parameters of coercivity, reversible and irreversible magnetizations. The summary and outlook of melt-spun permanent magnets are given in the final section.

## 2. Uniqueness in melt-spun materials

For melt-spun materials, there are many parameters to explore in order to achieve a certain magnetic phase and optimize the magnetic performance. First of all, the composition of the alloy is of major importance, not only considering the main elements Nd, Fe, and B, but also the additives, such as Nb, Al, Cu, etc. Secondly, there are many quenching parameters to be precise, which were mentioned in section 1.2. Thirdly, the ribbons obtained by melt spinning can be used directly or with subsequent heat treatment, such as post-annealing, hot pressing, or die upsetting. In the latter case, the pressure and temperature are critical and must be carefully controlled.

This section will discuss the unique characteristics of melt-spun materials using Nd–Fe–B as an example. Figure 3 shows a typical phase diagram of Nd–Fe–B alloy system. From the phase constitution point of view, the Nd–Fe–B alloys for permanent magnets are categorized according to the Nd content: (i) near-stoichiometric alloy that corresponds to the 2:14:1 phase; (ii) alloy with high Nd content that contains the 2:14:1 phase and a Nd-rich phase such as  $\text{Nd}_{1+\epsilon}\text{Fe}_4\text{B}_4$  or

$\text{Nd}_2\text{Fe}_3\text{B}_4$  phase; and (iii) alloy with low Nd content that contains 2:14:1 and a soft magnetic phase such as  $\alpha$ -Fe or  $\text{Fe}_3\text{B}$  phase. At a slow cooling rate, the stoichiometric  $\text{Nd}_2\text{Fe}_{14}\text{B}$  alloy solidifies according to the following sequence based on the phase diagram: initial Fe nuclei forms first in a Fe-depleted liquid matrix. The Fe-depleted liquid matrix then forms the  $\text{Nd}_2\text{Fe}_{14}\text{B}$  grains and an Nd-rich phase. Therefore, the as-cast  $\text{Nd}_2\text{Fe}_{14}\text{B}$  ingot consists of  $\text{Nd}_2\text{Fe}_{14}\text{B}$  grains,  $\alpha$ -Fe residual crystals, and Nd-rich grains, so they have to be followed by a long period homogenization annealing at high temperature.

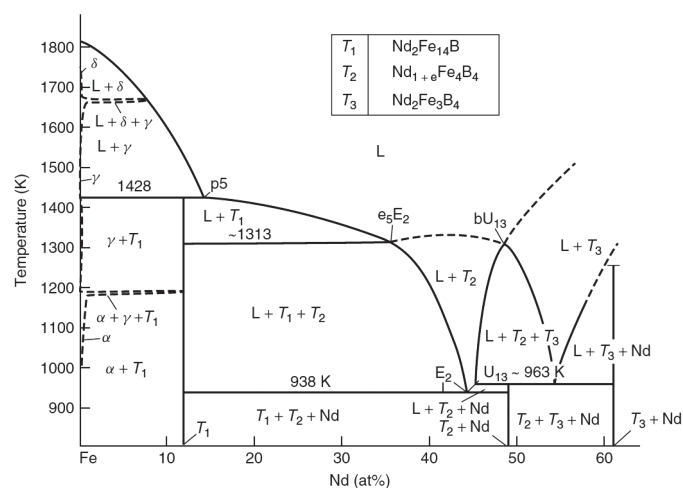
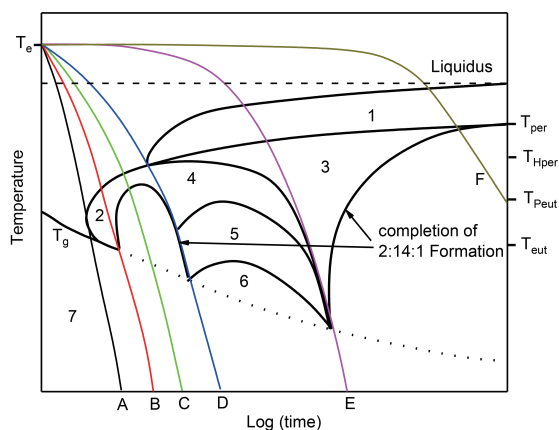


Fig. 3. A vertical section of Nd–Fe–B phase diagram.<sup>[18,19]</sup>

### 2.1. Cooling control

The melt-spinning process is different from the conventional casting and sintering process. The super high cooling rate could prevent the eutectic crystallization and thus no residual  $\alpha$ -Fe and Nd-rich grains in the quenched ribbons even in the stoichiometric  $\text{Nd}_2\text{Fe}_{14}\text{B}$  alloy. However, rapidly solidified  $\text{Nd}_2\text{Fe}_{14}\text{B}$  alloys may have different microstructural features depending on the thermal history of melt before ejection. To better understand the process of melt spinning, a CCT diagram is much better than the phase diagram since the phase diagram only indicates the equilibrium phases. Under no equilibrium conditions, kinetic as well as thermodynamic factors determine what phases and the microstructure will form. Although the development of quantitative CCT diagram is difficult for melt-spinning process due to the extremely high cooling rate, the qualitative representations of the process in Nd–Fe–B system are still possible and are conceptually useful. Branagan and McCallum developed such a CCT diagram in order to interpret the impact of cooling rate on the phase formation in the  $\text{Nd}_2\text{Fe}_{14}\text{B}$  system near stoichiometric 2:14:1 phase,<sup>[18,20]</sup> as shown in Fig. 4. Seven regions are indicated which are representative of different phase reactions and are given in Table 1.



**Fig. 4.** (color online) CCT diagram for stoichiometric  $\text{Nd}_2\text{Fe}_{14}\text{B}$ . Reproduced from Ref. [18].

**Table 1.** Reaction regions of CCT diagram for stoichiometric  $\text{Nd}_2\text{Fe}_{14}\text{B}$ .<sup>[18,20]</sup>

Region	Reaction	Type	Description
1	$\text{L} \rightarrow \text{Fe}, \text{L}_1$	Peritectic	Properitectic iron reaction
2	$\text{L} \rightarrow \text{T}_1$	Transition	Direction crystallization
3	$\text{L}, \text{Fe} \rightarrow \text{T}_1$	Peritectic	Peritectic reaction
4	$\text{L} \rightarrow \text{T}_1, \text{L}_1$	Peritectic	Hyperperitectic reaction
5	$\text{L} \rightarrow \text{T}_1, \text{T}_2, \text{L}_1$	Eutectic	Proeutectic reaction
6	$\text{L} \rightarrow \text{T}_1, \text{T}_2, \text{Nd}$	Eutectic	Ternary eutectic reaction
7	$\text{L} \rightarrow \text{Glass}$	Transition	Liquid to glass transition

Six representative cooling curves are drawn on the CCT diagram, starting from the ejection temperature ( $T_e$ ) of the melting spinning, which are summarized below.

(i) For cooling curve A, the sufficiently high cooling rate makes it possible to form a 100% amorphous structure as the alloy is cooled below the glass transition temperature before crystalline phases can nucleate.

(ii) On the other hand, the cooling curve F on the right-hand of the diagram is near equilibrium cooling. Fe begins to precipitate at the liquidus. Once the peritectic temperature is reached, the Fe and the liquid react to form the 2:14:1 phase.

(iii) In the powder metallurgy route, solidification rates during casting occur between cooling curves D and E. The solidification sequence begins with the properitectic reaction and Fe formation (region 1), followed by the peritectic reaction (region 3) which requires bulk diffusion and is very sluggish. The cooling rates are fast enough in this region to allow only limited diffusion, which causes bulk segregation in both the liquid and solid phases. The solidification sequence after the peritectic reaction occurs through the hyperperitectic (region 4), proeutectic (region 5), and ternary eutectic reaction (region 6) as shown in Fig. 4.

(iv) When the cooling rate is sufficient to undercool below the peritectic temperature, direct solidification of the 2:14:1 phase occurs. Cooling curve B gives a fully crystallized 2:14:1 single-phase microstructure, while cooling rate between A and B causes partially crystallization and represents an overquenched condition. The optimum cooling rate,

which is slightly faster than cooling curve B, will generate the ideal microstructure consisting of an almost completely crystallized nanostructure and a small amount of amorphous grain boundary phase. The grain boundary amorphous phase is important for magnetically decouple adjacent grains, similar to the Nd-rich grain boundary in sintered magnets. The 2:14:1 phase content decreases with increasing cooling rate from B to A, while the amorphous content increases.<sup>[21]</sup>

(v) In cooling curve C, a completely crystalline 2:14:1 structure can be formed but the alloy is in the under quenched condition. Therefore, the grains have time to grow above the optimum grain size during cooling.

The CCT diagram has been used to explain the effects of cooling rate and the alloy modifications on phase formation in 2:14:1 alloys through experiments by Branagan and McCallum.<sup>[18]</sup> A series of wheel speed ( $v_{ws}$ ) from 5 to 30 m/s were controlled while other melt-spinning parameters are fixed same. The analysis shows that the cooling rate achieved in the  $< 17.5$  m/s sample is equivalent to a cooling rate slower than cooling curve D. The formation of large inclusion of free iron grains is the reason for the very low coercivity in the melt-spun ribbons. Region 7 of glass formation need an approximately 30 m/s wheel speed, i.e., the cooling rate is larger than that of cooling curve A. The cooling rates equivalent to wheel speed between 17.5 and 30 m/s (i.e., between cooling curves B and D on the model CCT diagram) leads to region 2 where grain nucleation and growth of the magnetically hard phase happen along with grain growth during self-annealing. The highest coercivity of the stoichiometric 2:14:1 ribbon is obtained in the samples with wheel speed of about 20–22.5 m/s, which is consistent with some recent works in mischmetal 2:14:1 alloys.<sup>[22]</sup> It should be noted that the optimum cooling rate can be changed by more than a factor of two through appropriate alloying additions.

Besides the cooling rate, the melting temperature prior to ejection,  $T_e$ , also plays an important role on the microstructure of quenched ribbons. Tang *et al.* studied the impact of  $T_e$  varying from 1300 °C to 1500 °C, as well as the cooling rate, on the phase formation of the stoichiometric 2:14:1 alloys through thermal analysis and transmission electron microscopy (TEM) analysis.<sup>[21]</sup> It was observed that a lower melt ejection temperature around 1300 °C produced a nanocrystalline microstructure, while higher melt ejection temperatures above 1450 °C largely eliminated the presence of nuclei and associated nanophases and thus produced an amorphous product. Therefore, an increase in the ejection temperature leads to a decrease in the wheel speed necessary to attain an optimum microstructure and thus energy product, as shown in Fig. 5. In another word, the quench ability and glass phase content in the ribbons are enhanced by increasing the ejection temperature.

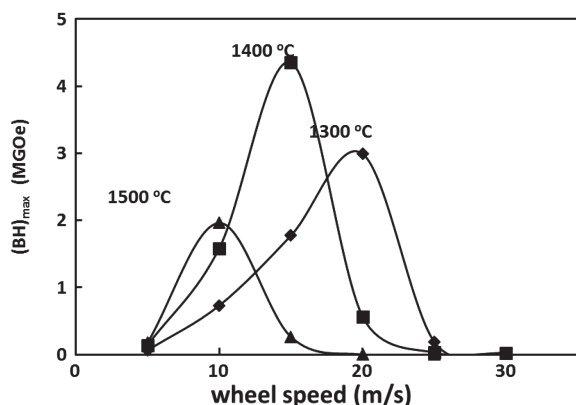


Fig. 5.  $(BH)_{\max}$  of as-spun ribbons produced under different ejection temperatures and wheel speed conditions.<sup>[21]</sup>

## 2.2. Amorphization and crystallization

Although directly quenching into nanocrystalline magnet has less processing steps, forming an amorphous or overquenched structure is easier to control for melt-spinning procedures. It also represents a wider processing zone for post-treatment after quenching. In thermomechanical processing, such as hot pressing, the overquenched materials allow more time for compaction to reach full density before the grains growth above the optimum size. Therefore, the overquenched approach is more popular than direct solidification into nanocrystalline. The glass-forming ability of alloys is then very important for this approach. Brangan *et al.* investigated the effects of Ti and/or C additions on the solidification behavior of  $Nd_2Fe_{14}B$  alloys.<sup>[18,23,24]</sup> They found that the glass-forming ability of the Ti/C added materials substantially increases, as the wheel speed drops from 30 m/s down to 12 m/s in order to form the amorphous. The addition of Ga based on the Nd–Fe–B–Ti–C alloy could further reduce the glass forming ability and refine the magnetically hard grains in the final materials.<sup>[25]</sup> Shen *et al.* found that a wheel speed of only 6.6 m/s could produce an amorphous structure in the rapidly quenched high B content Nd–Fe–B alloys.<sup>[26,27]</sup>

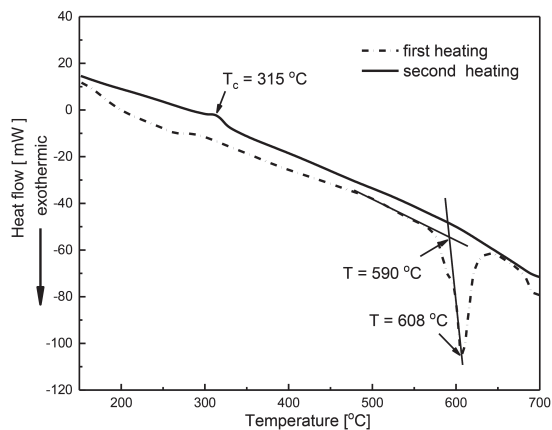


Fig. 6. DSC curves of amorphous Nd–Fe–B alloy showing the exothermic crystallization peak at 608 °C, where the onset temperature is 590 °C during the first heating. The second heating curve indicates the Curie temperature at  $T_c = 315$  °C.<sup>[28]</sup>

In addition to improving the glass forming ability of alloys, controlling the post-annealing condition is one of the key factors to optimize the microstructure and magnetic properties of the  $Nd_2Fe_{14}B$  ribbons. The annealing temperature is usually guided by the crystallization temperature of the amorphous,  $T_{cr}$ , which is typically determined by differential scanning calorimetry (DSC) curve, or differential thermal analysis CDTA curve. Figure 6 illustrates the crystallization behavior of a typical amorphous Nd–Fe–B alloy where the strong exothermic peak indicates the onset of crystallization at a temperature close to 590 °C.<sup>[28]</sup> The presence of a second-order thermodynamic phase transition around 315 °C during second heating corresponds to the Curie temperature of the 2:14:1 phase. It should be noticed that  $T_{cr}$  is affected by many factors, such as preparation methods,<sup>[29]</sup> composition, and ejection temperature during melt-spinning.<sup>[21,30]</sup> For example,  $T_{cr}$  of melt-spun ribbons is 20–40 °C higher than that of ball-milled powders with the same composition, while  $T_{cr}$  of the Nd-based alloys is 25–50 °C higher than that of Pr-based alloys. Shen *et al.* systematically studied the effect of composition on the crystallization temperature of  $Nd_y(Fe_{1-x}B_x)_{100-y}$  alloys,<sup>[27,31–34]</sup> as given in Fig. 7. It is observed that  $T_{cr}$  depends strongly on B content. The substitution of B for Fe significantly enhances the thermal stability of amorphous Nd–Fe–B alloys.

Table 2. Impact of additives on crystallization temperature of  $Nd_2Fe_{14}B$  alloys.

Additive element	Additive amount/at%	$\Delta T_{cr}/^{\circ}C$	Reference
Nb	1	16	[36]
Zr	1	21	[36]
Dy	4	11	[37]
Si	3	30	[38]
Cr	10	10	[39]
Co	5	–26	[40]

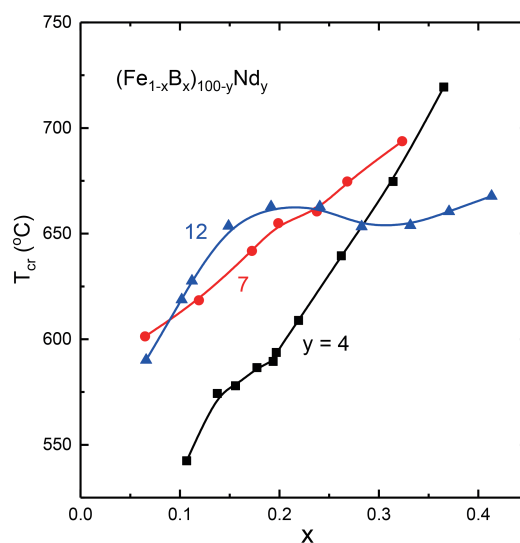


Fig. 7. (color online) Dependence of crystallization temperature of amorphous  $Nd_y(Fe_{1-x}B_x)_{100-y}$  alloys on B content with  $y = 4, 7,$  and  $12$ .<sup>[27,31–34]</sup>

A maximum crystallization temperature is observed in the  $\text{Nd}_{12}\text{Fe}_{73}\text{B}_{15}$ , which is exactly the eutectic composition of the ternary Nd–Fe–B system. It is believed that a small amount of Nd addition into the Fe–B alloys leads to the increase of alloy viscosity and reduction of diffusion coefficient, and thus the enhancement of thermal stability of amorphous alloys. This is why the crystallization temperature of Nd–Fe–B is about 120–210 °C higher than that of Fe–B alloys.<sup>[31,35]</sup> The effects of other elements on the crystallization temperature have also been studied, with some of the results are summarized in Table 2.

### 2.3. Phase formation

The optimum annealing temperature for overquenched RE–Fe–B ribbons is slightly higher than the crystallization temperature, i.e., in the range of 650–800 °C, which leads to the formation of an optimum microstructure for magnetic hardening. Particularly, it eliminates  $\alpha$ -Fe or  $\text{Fe}_3\text{B}$  phase, which is usually the first product of the crystallization process. Gu *et al.* studied the crystallization and magnetic properties of amorphous  $\text{Nd}_x\text{Fe}_{81}\text{B}_{19-x}$  alloys systematically.<sup>[41]</sup>

Table 3 summarizes the phase components in the annealed ribbons from amorphous alloys, which are confirmed by the nuclear magnetic resonance (NMR) and Mossbauer effect reported by Cheng *et al.*<sup>[42]</sup> As one can see that the amorphous-crystalline transition occurs at temperature as low as 600 °C. The crystalline phases vary with both annealing temperature and materials composition, while the ribbons have multiple phases in most cases. A single-phase  $\text{Nd}_2\text{Fe}_{14}\text{B}$  magnet with the highest coercivity was obtained by a 800 °C annealing of the  $\text{Nd}_{12}\text{Fe}_{81}\text{B}_7$  ribbon, which is close to the stoichiometric composition of the 2:14:1 phase.

Besides annealing temperature, the annealing time affects the phase formation as well. A melt-spun amorphous exhibits formation of various phase as time elapses in isothermal annealing and are shown in Table 4.<sup>[3]</sup> The result clearly indicates that the coexistence of  $\text{Fe}_3\text{B}$  and  $\text{Nd}_2\text{Fe}_{14}\text{B}$  is only metastable and the thermodynamically stable phases are  $\text{NdFe}_4\text{B}_4$  and  $\alpha$ -Fe. Therefore, both annealing temperature and time should be carefully controlled in order to obtain magnetically hard  $\text{Nd}_2\text{Fe}_{14}\text{B}$  phase.

Table 3. Phase components in annealed  $\text{Nd}_x\text{Fe}_{81}\text{B}_{19-x}$  alloys.<sup>[41]</sup>

$X$	600 °C	700 °C	800 °C	900 °C
0	$\alpha$ -Fe, $\text{Fe}_3\text{B}$	$\alpha$ -Fe, $\text{Fe}_3\text{B}$	$\alpha$ -Fe, $\text{Fe}_3\text{B}$	$\alpha$ -Fe, $\text{Fe}_3\text{B}$ , $\text{Fe}_2\text{B}$
3	$\alpha$ -Fe, $\text{Fe}_3\text{B}$	$\alpha$ -Fe, $\text{Fe}_3\text{B}$	$\alpha$ -Fe, $\text{Fe}_3\text{B}$ , $\text{T}_2$	$\alpha$ -Fe, $\text{Fe}_3\text{B}$ , $\text{T}_2$
8	am, $\alpha$ -Fe, $\text{T}_1$	$\alpha$ -Fe, $\text{T}_1$ , UP	$\alpha$ -Fe, $\text{T}_1$ , $\text{T}_2$	$\alpha$ -Fe, $\text{T}_1$ , $\text{T}_2$
10	$\alpha$ -Fe, $\text{T}_1$	$\alpha$ -Fe, $\text{T}_1$	$\alpha$ -Fe, $\text{T}_1$	$\alpha$ -Fe, $\text{T}_1$
12	$\alpha$ -Fe, $\text{T}_1$	$\alpha$ -Fe, $\text{T}_1$	$\text{T}_1$	$\alpha$ -Fe, $\text{T}_1$
15	am, $\alpha$ -Fe	$\alpha$ -Fe, $\text{T}_1$ , $\text{Nd}_2\text{Fe}_{17}$ , Nd	$\text{T}_1$ , $\text{Nd}_2\text{Fe}_{17}$ , Nd	$\text{T}_1$ , $\text{Nd}_2\text{Fe}_{17}$ , Nd
15	$\alpha$ -Fe, $\text{Nd}_2\text{Fe}_{17}$ , Nd	$\alpha$ -Fe, $\text{Nd}_2\text{Fe}_{17}$ , Nd	$\text{Nd}_2\text{Fe}_{17}$ , Nd	$\text{Nd}_2\text{Fe}_{17}$ , Nd

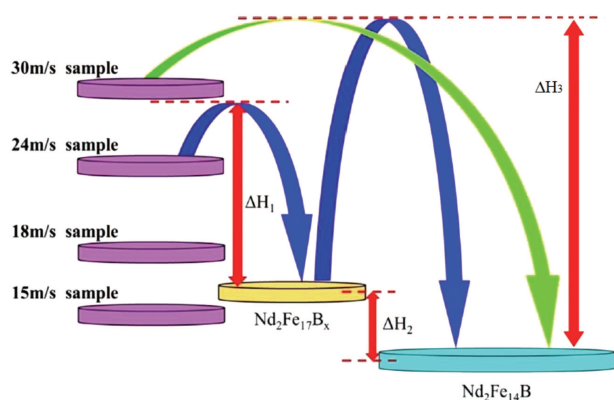
Note: am, UP,  $\text{T}_1$ , and  $\text{T}_2$  represent amorphous, unidentified phase,  $\text{Nd}_2\text{Fe}_{14}\text{B}$ , and  $\text{Nd}_{1.1}\text{Fe}_4\text{B}_4$ , respectively.

Table 4. Crystalline phases in  $\text{Nd}_{4.5}\text{Fe}_{77}\text{B}_{18.5}$  during isothermal annealing.<sup>[3]</sup>

Temperature	Time (minutes)		
	10	180	360
600 °C	$\alpha$ -Fe, $\text{Fe}_3\text{B}$ , $\text{T}_1$ , $\text{Nd}_2\text{Fe}_{23}\text{B}_3$	$\alpha$ -Fe, $\text{Fe}_3\text{B}$ , $\text{T}_1$	$\alpha$ -Fe, $\text{Fe}_3\text{B}$ , $\text{T}_1$
630 °C	$\text{Fe}_3\text{B}$ , $\text{T}_1$ , $\text{Nd}_2\text{Fe}_{23}\text{B}_3$	$\alpha$ -Fe, $\text{Fe}_3\text{B}$ , $\text{T}_1$	$\alpha$ -Fe, $\text{Fe}_3\text{B}$ , $\text{T}_1$
680 °C	$\alpha$ -Fe, $\text{Fe}_3\text{B}$ , $\text{T}_1$	$\alpha$ -Fe, $\text{Fe}_3\text{B}$ , $\text{NdFe}_4\text{B}_4$	$\alpha$ -Fe, $\text{Fe}_3\text{B}$ , $\text{NdFe}_4\text{B}_4$

The crystallization also depends on the initial phase structure of the quenched ribbons. Men *et al.* prepared a set of ribbons with different initial phase structure, i.e., amorphous, TbCu<sub>7</sub>-type  $\text{Nd}_2\text{Fe}_{17}\text{B}_x$ ,  $\alpha$ -Fe, and their mixture, by varying wheel speed from 15 to 40 m/s.<sup>[43]</sup> They used the theory of energy barrier to interpret the crystallization process, as schematized in Fig. 8. It is known that the metastable  $\text{Nd}_2\text{Fe}_{17}\text{B}_x$  or  $\text{Nd}_2\text{Fe}_{23}\text{B}_3$  phase has a higher energy than  $\text{Nd}_2\text{Fe}_{14}\text{B}$  phase and the larger amorphous content leads to a higher system energy. Like other chemical reactions, the crystallization process has to absorb enough external energy to overcome the potential barrier until a more stable state is formed. Assuming

the system energy of the sample prepared at 15 m/s is lower than that of pure  $\text{Nd}_2\text{Fe}_{17}\text{B}_x$  phase, reaction (1) can hardly occur while reaction (2) do happen. The amorphous content increases while the  $\text{Nd}_2\text{Fe}_{17}\text{B}_x$  phase content decreases with increasing wheel speed from 18 to 27 m/s. Therefore, the proportion of reaction (1) increases correspondingly. A ribbon with complete amorphous, which is prepared by wheel speed above 27 m/s, requires a higher energy than the potential barriers of the transition from  $\text{Nd}_2\text{Fe}_{17}\text{B}_x$  or  $\text{Nd}_2\text{Fe}_{14}\text{B}$  phase. Hence, the crystallization process follows reaction (3) instead of the reactions (1) or (2).



**Fig. 8.** (color online) The crystallization mechanism of as-quenched ribbons with different initial phase structure.  $\Delta H_1$ ,  $\Delta H_2$ , and  $\Delta H_3$  are the enthalpy change of the reactions: (1) amorphous  $\rightarrow$   $\text{Nd}_2\text{Fe}_{17}\text{B}_x$ , (2)  $\text{Nd}_2\text{Fe}_{17}\text{B}_x \rightarrow \text{Nd}_2\text{Fe}_{14}\text{B}$ , and (3) amorphous  $\rightarrow$   $\text{Nd}_2\text{Fe}_{14}\text{B}$ , respectively.<sup>[43]</sup>

## 2.4. Consolidation

Most applications required a bulk-shaped permanent magnet, instead of ribbons, flakes or powders. Bulk nanostructured magnets can be produced through direct casting, compression molding, injecting molding, hot compaction, hot-deformation and other technologies. The direct casting process requires the remarkable glass-forming ability of the alloys in order to cast them into amorphous or nanocrystalline tubes or rods with 0.5–2 mm in diameter, followed by crystallization annealing to form the appropriate nanocrystalline structure and hard magnetic properties.<sup>[44–47]</sup> Although it is feasible to make bulk magnets through direct casting, the popular bulk nanostructured permanent magnets are still bonded magnets and hot-deformed magnets.

Bonded magnets can be manufactured by compression molding, extrusion, injection molding or calendaring processes. In their most basic form bonded magnets consist of two components: a hard magnetic powder and a non-magnetic polymer or rubber binder.<sup>[48]</sup> For bonded magnets utilizing melt-spun products, the powders are general in a small flake shape such as the Magnequench powders. The binder that holds the magnetic particles in place can produce either a flexible or rigid magnet. Bonded magnets are usually isotropic due to the naturally isotropic grain structure of the melt-spun ribbons. However anisotropic bonded could be produced as well, if the texture is obtained in the melt-spun ribbons,<sup>[49]</sup> or if single crystal powders can be produced by special crashing methods.<sup>[50]</sup> The processes and magnetic properties of *RE* bonded magnets have been thoroughly reviewed by Liu and Walmer.<sup>[51]</sup>

Compression molding is the process which produces the best magnetic properties. The processed melt-spun powders are coated by a thin film of thermoset epoxy, hardener and other additives. The encapsulated powders are then fed into a press cavity and compacted under pressure, followed by curing

at a temperature about 150–175 °C. One major advantage of compression bonding is that the volume of magnetic powders can be as high as 85%, resulting in a higher flux density than other methods. The maximum energy product of compression molded isotropic Nd–Fe–B magnets is about 10–12 MGOe. Injection molding is the process of injecting a molten, highly filled thermoplastic compound into mold cavities where it is allowed to cool and solidify. Both Nd–Fe–B, Sm–Co, and ferrite powders are commonly used as the magnetic powder in the compound. The injection molding process has the advantage of producing complex-shaped components with consistent accuracy. Typical magnetic powder volume is around 65%, with an energy product of about 5–6 MGOe for isotropic Nd–Fe–B bonded magnet. Extrusion and calendaring are commonly used for flexible bonded ferrite magnets, while it may be used for melt-spun powders as well. The advantage of these processes is the continuous production of magnets of two-dimensional geometries, such as strips or sheets of virtually unlimited length with a typical sheet thickness of 0.3 – 6 mm.

While bonded magnets could be made from different magnetic powders, hot compaction is more suitable to nanocrystalline magnetic powders, especially for isotropic magnets. Hot compaction is a high-pressure, low-strain-rate powder metallurgy process for forming of powder compact at a temperature high enough to induce sintering or creeping processes. Within hot compaction technology, three distinctly different types of heating can be applied: inductive heating, indirect resistance heating, and direct heating. Among these three methods, inductive heating, where the heat is generated by using an induction coil, is rarely used for hot compaction of permanent magnetic materials.

With indirect resistance heating technology, the mold is placed in a heating chamber, which is powered by heating elements, as shown in Fig. 9(a). This is the most common method used in hot compaction of bulk nanocrystalline magnets. To produce a fully dense magnet, the typical compaction temperature is about 700 °C under 100–500 MPa pressure.<sup>[52,53]</sup> Typical grain size is about 30–100 nm and maximum energy product could reach  $\sim$  20 MGOe in such hot-compacted Nd–Fe–B magnets.

For direct hot pressing, the mold is directly connected to electrical power. The resistivity of the mold and the powder part generates the heat directly in the mold, as shown in Fig. 9(b). It results in very high heating rates and a significant increase in fine metal powder aggregation which makes compaction time of a few minutes possible. Further, this process lowers the compaction temperature and pressure compared to that required in conventional sintering processes. Spark plasma sintering (SPS) is one of the direct heating methods which has been used to compact the nanocrystalline permanent

magnetic powders. The main characteristic of SPS is that the pulsed DC current directly passes through the graphite die, as well as the powder compact, in the case of conductive samples. The magnetic properties and structure of the SPS compacted Nd–Fe–B magnets have been compared with those of conventional hot compaction recently.<sup>[54–57]</sup> Although the pressure of SPS is usually lower than that of conventional hot compaction due to the limitation of graphite die, the unique feature of the direct heating still results in fast consolidation of the powders at similar or lower compaction temperature. More importantly, the shortened cycle time of the SPS technique then effectively avoids grain growth which makes it specially suitable to prepare nanocrystalline permanent magnets. The grain size of 20 nm or even smaller can be achieved in nanocrystalline Nd–Fe–B magnets, which ensures the effective exchange coupling in the materials. The SPS technique has also been approved useful to compact other magnetic materials, such as Fe–Pt nanoparticles,<sup>[58]</sup> and Sm–Co powders.<sup>[59]</sup>

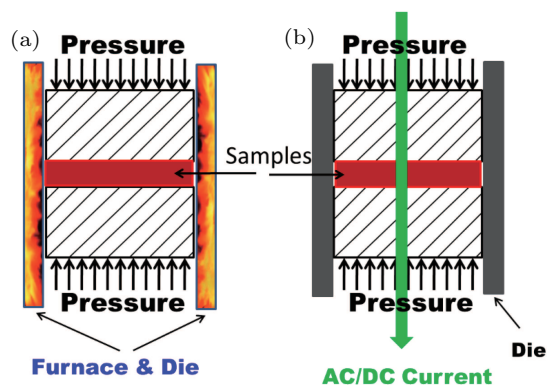


**Fig. 9.** (color online) Schematic of hot compaction through two different heating methods: (a) indirect resistance heating; (b) direct heating such as Joule-heating or SPS heating.

Instead of using pulsed DC current in SPS technique, Rong *et al.* developed a similar but simplified hot press using AC current as a heating source, which could reach a heating rate of 300 °C/min. The fast heating benefits the controlling of grain size and nanostructure in the compaction processes, especially for the hard/soft nanocomposite magnets where the grain size of the magnetically soft phase is critically important. Another improvement of this instrument is the much higher pressure up to 2 GPa, comparing to the SPS press with graphite die.<sup>[60,61]</sup> The higher pressure could further lower the compaction temperature, which is in turn to prevent excessive grain growth. A maximum energy product of 18.5 MGOe is obtained in the fully dense SmCo<sub>5</sub>/α-Fe nanocrystalline magnet with magnetically soft grains of 8–15 nm by compaction at a temperature as low as 540 °C.<sup>[60]</sup>

The explosive or shock compaction is a technique of consolidating powders using high-pressure shock waves, which is considered as a potential method to consolidate hard-to-sinter

powders and amorphous or fine nanocrystalline powders. Extremely high pressures up to 20 GPa can be applied to the powders in a very short time, even within several milliseconds.<sup>[62]</sup> The amorphous or nanocrystalline has no time to gain growth in such a short period. The shock compaction has been successfully used to produce bulk nanocrystalline permanent magnets in the past 20 years, including Nd<sub>2</sub>Fe<sub>14</sub>B,<sup>[63]</sup> Pr<sub>2</sub>Fe<sub>14</sub>B/α-Fe,<sup>[64]</sup> Sm–Fe–N,<sup>[65]</sup> and Fe<sub>16</sub>N<sub>2</sub>.<sup>[66]</sup>

Besides sintering technology, hot-deformation-induced texturing of nanocrystalline materials is another option for producing fully dense, anisotropic magnets with maximized energy products. Hot deformed Nd–Fe–B magnets have attracted attention not only because of their good magnetic properties but also due to their exceptional corrosion resistance, thermal stability, and fracture toughness compared to sintered magnets.<sup>[67]</sup> The hot deformation process usually starts from the preparation of a fully dense isotropic precursor. The precursor is then placed in an oversized die-cavity where die-upsetting is carried out at similar temperatures, as schematized in Fig. 10(a). It was found that grain growth occurs much more rapidly to the perpendicular direction of crystallographic *c*-axis than the parallel direction during die upsetting. This anisotropic grain growth results in platelet-shaped Nd<sub>2</sub>Fe<sub>14</sub>B grains, surrounded by continuous films of a Nd-rich grain boundary phase. The Nd-rich phase is molten during die upsetting and thus serves to enhance grain boundary sliding and allows the platelet-shaped grains to slip until they end up with their wide flat faces normal to the axis of compression.<sup>[68,69]</sup> Therefore, the anisotropic magnet is obtained with the alignment of the crystallographic *c*-axis parallel to the pressing direction after die upsetting. A typical microstructure is given in Fig. 10(c). Up to now, the largest reported value of (BH)<sub>max</sub> for hot deformed magnets is ~50 MGOe, which was achieved in a Nd–Fe–Co–Ga–B alloy.<sup>[70]</sup>

Alternatively, backward extrusion can be utilized to produce near-net shape ring magnets, especially for small dimensions. Backward extrusion offers many advantages, including lower materials consumption, higher dimensional accuracy, and surface quality, adequate mechanical properties and the elimination of subsequent operations. The ring magnets produced by backward extrusion have superior magnetic properties to sintered magnets, which have been already used in electrified vehicles directly. Similar to die upsetting, a fully dense precursor need to be produced by hot compaction before backward extrusion, as schematized in Fig. 10(b). The preferential orientation of platelet-shaped Nd<sub>2</sub>Fe<sub>14</sub>B grains is radially-oriented after extrusion. Small variations in the magnetic properties have been observed along the cross-section and along the axial direction of the ring magnets which were attributed to inhomogeneities in materials flow inherent to the deformation process.<sup>[71,72]</sup>

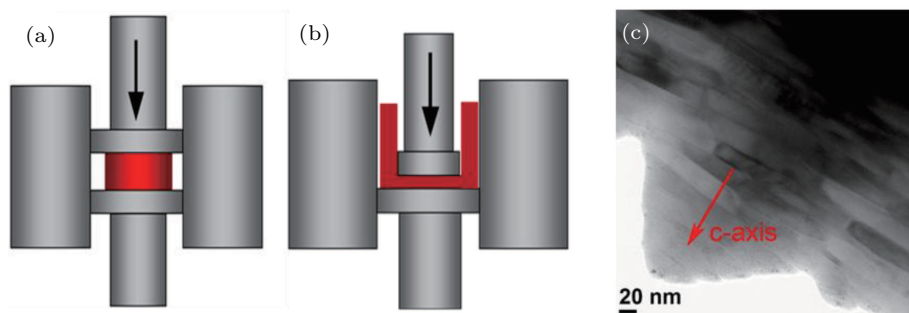


**Fig. 10.** (color online) Schematic of hot deformation: (a) Die-upsetting; (b) backward extrusion; (c) typical microstructure of hot-deformed magnet.<sup>[61]</sup>

### 3. Melt-spun materials

#### 3.1. Single-phase nanocrystalline magnets

The single-phase magnetic materials usually have a chemical composition very close to the stoichiometric composition to minimize the presence of secondary phases. The nanostructure is obtained either by direct quenching into nanocrystalline through optimum melt-spinning parameters, or by crystallization of the precursor amorphous alloys formed through over quenching process. The single-phase magnets with different phase structure are reviewed below.

##### 3.1.1. 2:14:1 phase

The 2:14:1 phase has a  $P4_2/mnm$  tetragonal space group with four formula units or 68 atoms per unit cell.  $Nd_2Fe_{14}B$  is the most common studied material with 2:14:1 phase structure. The microstructure of single-phase  $Nd_2Fe_{14}B$  melt-spun materials is fairly uniform, consisting of randomly oriented grains of the magnetically hard phase as shown in Fig. 11(a). In the single-phase stoichiometric  $Nd_2Fe_{14}B$  magnets, the

magnetically hard grains are directly connected without grain boundary phase and therefore they are magnetically coupled by exchange interaction, which is symbolized by a spring in Fig. 12(a).<sup>[73,74]</sup> High coercivity can be easily obtained in the single-phase  $Nd_2Fe_{14}B$  magnets with grain sizes below 80 nm. This grain size is far below the single domain particle size, which is a fraction of 1  $\mu m$  for most of the high anisotropy materials. Figure 11(b) shows the high-resolution TEM micrograph of a stoichiometric  $Nd_2Fe_{14}B$  magnet with an average grain size of 20 nm.<sup>[75]</sup> No grain boundary phase is observed. Since the magnetically hard grains are directly contacted in the stoichiometric magnets, a significantly enhanced remanence ( $m_r$  is larger than 0.5) and a slightly reduced coercivity are observed as a consequence of exchange coupling between the grains, as shown in Fig. 12(d), which will be discussed in details in Section 4. As the exchange interaction is a short-range interaction, which is in the order of  $\sim 4$  nm for  $Nd_2Fe_{14}B$ , the grain size should be smaller than 50 nm in order to notice the remanence enhancing effect macroscopically.<sup>[17]</sup>

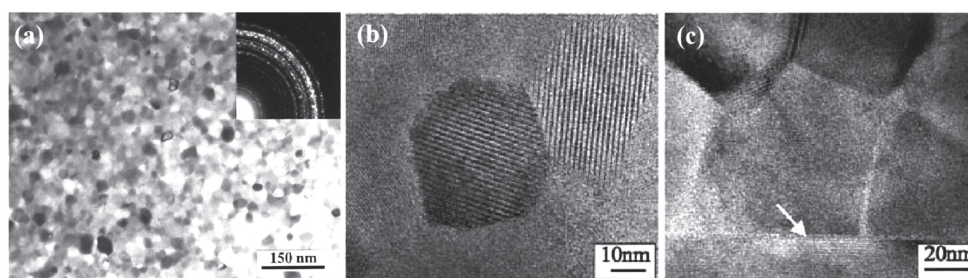


**Fig. 11.** (a) Typical microstructure of nanocrystalline  $Nd_2Fe_{14}B$ ;<sup>[76]</sup> high-resolution TEM of (b) stoichiometric and (c) decoupled 2:14:1 magnets.<sup>[75]</sup>

To achieve even higher coercivity in a permanent magnet, the magnetically hard grains need to be decoupled. Although an amorphous grain boundary can be formed by optimum the cooling conditions in the as-spun ribbons, most commercial alloys contain excess Nd. The resulting microstructure obtained by melt-spinning qualitatively agrees with the situation in sintered permanent magnets where the single crystallites of the magnetically hard phase are more or less magnetically decoupled by a paramagnetic  $RE$ -rich boundary phase. How-

ever, the scale of the melt-spun microstructure is about a factor of 100 smaller than sintered magnet and the easy axes of the nanograins are isotropically distributed instead of aligned. The high-resolution TEM micrograph in Fig. 11(c) presents the intergranular film with a thickness of about 2 nm as a bright region between the nanograins.<sup>[75]</sup> Figure 12(b) schematizes the decoupling  $RE$ -rich grain boundaries. The grain size in such decoupled magnet ranges from 50 to 200 nm, which guarantees that mainly single-domain particles exist. There-

fore, a coercivity higher than 2.5 T can be achieved, which is larger than the stoichiometric single-phase magnet, as schematized in Fig. 12(d). However, since the easy-axis direction of the grains are isotropically distributed and magnetically decoupled, the maximum normalized remanence of 0.5 can only be achieved in such magnets according to Stoner–Wohlfarth model.<sup>[10]</sup>

If the alloy composition is chosen near to the two-phase line Fe–T<sub>1</sub> on the left region bordering the stoichiometric T<sub>1</sub> phase (as shown in Fig. 3), a so-called composite magnet can

be obtained, showing a further significant remanence enhancement, accompanied by a reduction of the coercivity as can be seen from Fig. 12(d). In such two-phase magnets, nanocrystalline soft magnetic  $\alpha$ -Fe grains arise in addition to the magnetically hard 2:14:1 grains from the melt-spinning process as a consequence of the over-stoichiometric  $\alpha$ -Fe, as schematized in Fig. 12(c). Thus, the remanence enhancement is due to the exchange coupling among the grains but also to the very large spontaneous polarization of the  $\alpha$ -Fe grains. The composite magnets will be discussed in Section 3.2 in details.

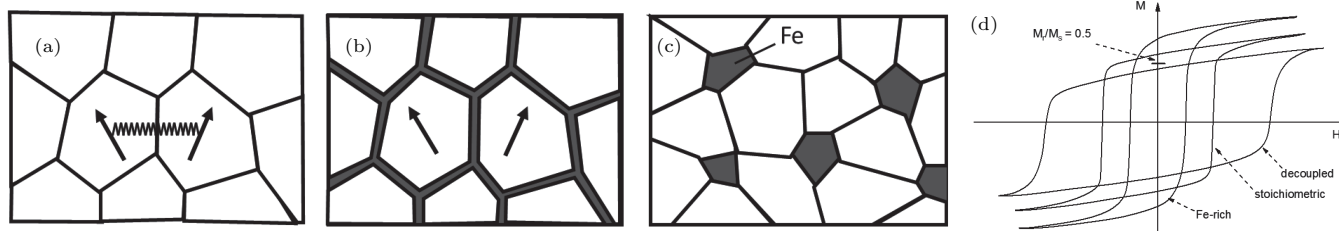


**Fig. 12.** Schematic of microstructure for the remanent state of (a) stoichiometric and (b) decoupled 2:14:1 based nanocrystalline magnets, (c) nanocomposite magnet, and (d) their hysteresis loops at room temperature.

The Nd<sub>2</sub>Fe<sub>14</sub>B phase is the most widely studied permanent magnetic materials by melt spinning as well as other techniques due to the excellent magnetic properties, i.e., high anisotropy field (> 7 T), and high saturated magnetization (~1.6 T). Croat *et al.* reported the single-phase Nd<sub>2</sub>Fe<sub>14</sub>B melt-spun materials having coercivity of about 1.5 T and energy product of about 14 MGOe under an optimum wheel speed of 16–20 m/s as early as 1984.<sup>[8]</sup> However, the Nd<sub>2</sub>Fe<sub>14</sub>B magnets have two major disadvantages compared to other permanent magnets. The Curie temperature of Nd<sub>2</sub>Fe<sub>14</sub>B magnet is only about 315 °C, which results in large negative temperature coefficients of remanence and coercivity, and therefore limits their application to 80 °C or lower. The material cost of Nd–Fe–B magnet is still far higher than that of ferrite magnets. Therefore, many 2:14:1-type magnets derived from Nd<sub>2</sub>Fe<sub>14</sub>B are developed through elemental additions or substitutions. They can be classified into the following categories based on the type of element substitutions:

(i) RE substitution for Nd

Replacing Nd by HRE such as Dy or Tb is an effective to raise the coercivity for higher temperature application since Dy<sub>2</sub>Fe<sub>14</sub>B and Tb<sub>2</sub>Fe<sub>14</sub>B have much higher anisotropy field comparing to Nd<sub>2</sub>Fe<sub>14</sub>B magnets, as seen in Table 5. Larger coercivity of up to 64 kOe at room temperature are reported for Dy<sub>2</sub>Fe<sub>14</sub>B and Tb<sub>2</sub>Fe<sub>14</sub>B alloys magnetically hardened by melt spinning technique,<sup>[77]</sup> which is over three times larger than that of Nd<sub>2</sub>Fe<sub>14</sub>B ribbons. Even though they may have similar negative temperature coefficient of coercivity as Nd<sub>2</sub>Fe<sub>14</sub>B, they can provide relatively large coercivity to satisfy the higher temperature applications. However, it has to be borne in mind that there is normally a trade-off between

higher coercivity and higher costs for the HRE substitutions. In addition, the antiferromagnetic HRE sublattice may lead to a strong magnetization reduction, as also given in Table 5.

Besides high-temperature application, element substitution is also useful for low-temperature application. For example, Pr<sub>2</sub>Fe<sub>14</sub>B magnets can be used at low temperature because there is no spin reorientation, while they have similar magnetic properties to those of Nd<sub>2</sub>Fe<sub>14</sub>B. Hadjipanayis *et al.* reported a coercivity of 2 T and energy product of 12 MGOe in the melt-spun single-phase Pr<sub>2</sub>Fe<sub>14</sub>B ribbons.<sup>[78]</sup>

Although RE elements are not truly rare geologically, they are expensive due to the extraction process, which makes the rare-earth magnets much more expensive than those of ferrite magnets. In order to reduce the material cost while utilize the still high magnetocrystalline structure of 2:14:1 phase, La/Ce based RE<sub>2</sub>Fe<sub>14</sub>B magnets attract the interests recently. Significant cost reduction can be achieved due to the much cheaper price of La/Ce by slightly sacrificing magnetic properties. An energy product of 8.6 MGOe is achieved in the Ce–Fe–B melt-spun ribbons as reported by Zhou *et al.*<sup>[79]</sup> If Nd is only half replaced by Ce, the energy product of 14.3 MGOe can be obtained through melt spinning as reported by Li *et al.*<sup>[80]</sup> The magnetic properties of the Ce-substituted Nd<sub>2</sub>Fe<sub>14</sub>B ribbons are summarized in Table 6. More commonly, the so-called mischmetals (MM) which contains ~ 50 wt% Ce and ~ 25 wt% La, are used to prepare 2:14:1-type magnets in order to further reduce cost by avoiding the extraction of Ce/La from each other. Zhang *et al.* reported an energy product of about 8.3 MGOe in the single-phase (La<sub>0.35</sub>Ce<sub>0.65</sub>)<sub>2</sub>Fe<sub>14</sub>B ribbons prepared at a wheel speed of 20 m/s.<sup>[81]</sup> Hussain *et al.* recently reported a La/Ce/La<sub>0.5</sub>Ce<sub>0.5</sub>

substituted Fe-rich 2:14:1 ribbons with improved magnetic properties ( $\mu_0 M_r = 1.07$  T,  $\mu_0 H_c = 0.59$  T, and  $(BH)_{\max} = 18.4$  MGOe), although it is a nanocomposite instead of single-phase magnet.<sup>[82]</sup> The relatively high coercivity in these ribbons may be attributed to the phase segregation with certain La or LaCe content.

**Table 5.** Intrinsic properties theoretical  $(BH)_{\max}$  limits of 2:14:1 compounds.<sup>[83–86]</sup>

RE	$T_c/^\circ\text{C}$	$\mu_0 M_s/\text{T}$	$K_1/\text{MJ}\cdot\text{m}^{-3}$	$\mu_0 H_A/\text{T}$	Theo. $(BH)_{\max}/\text{MGOe}$
<i>RE<sub>2</sub>Fe<sub>14</sub>B</i>					
Y	298	1.38	1.06	1.9	48
La	243	1.38	1.10	2.0	48
Ce	260	1.17	1.7	3.7	34
Pr	292	1.56	5.6	9.0	61
Nd	315	1.60	5	7.6	64
Sm	345	1.50	-12	-20.1	56
Gd	387	0.84	0.67	2.0	18
Tb	356	0.70	5.9	21.2	12
Dy	320	0.71	4.5	15.9	13
Ho	301	0.81	2.5	7.8	16
Er	284	0.90	-0.03	-0.1	20
Tm	267	1.15	-0.03	-0.1	33
Lu	266	1.17	1.17	2.6	34
<i>RE<sub>2</sub>Fe<sub>14</sub>C</i>					
Pr	239	1.67	9.8	14.8	70
Nd	262	1.65	6.2	9.5	68

**Table 6.** Magnetic properties of melt-spun  $\text{Nd}_{12-x}\text{Ce}_x\text{Fe}_{82}\text{B}_6$  ribbons.<sup>[80]</sup>

$x$	$T_c/^\circ\text{C}$	$\mu_0 M_r/\text{T}$	$\mu_0 H_c/\text{T}$	$(BH)_{\max}/\text{MGOe}$
0	366	0.98	1.09	20.9
1	357	0.93	1.04	18.0
2	348	0.91	0.96	17.2
4	331	0.87	0.84	16.0
6	313	0.84	0.77	14.3
8	298	0.77	0.68	12.1
10	279	0.74	0.52	10.8
11	268	0.68	0.41	8.04
12	253	0.64	0.32	5.54

#### (ii) Co substitution for Fe

Replacing Fe by Co substitution is an effective way to raise Curie temperature and potentially reduces temperature coefficients of coercivity and remanence. It is known that  $\text{Nd}_2(\text{Co}_x\text{Fe}_{1-x})_{14}\text{B}$  pseudo-ternary systems form the 2:14:1-type crystal structure for all levels of cobalt substitution, with  $T_c$  increasing monotonically to  $\sim 722$  °C for  $\text{Nd}_2\text{Co}_{14}\text{B}$ .<sup>[87]</sup> It is found that the desirable enhancement of  $T_c$  is accompanied by improved temperature stability of the remanence in the  $\text{Nd}_2(\text{Co}_x\text{Fe}_{1-x})_{14}\text{B}$  melt-spun ribbons if the Co content is less than 30%.<sup>[88]</sup> However, the coercivity deteriorates dramatically as the Co content increases above 40% due to the easy formation of  $\text{Nd}_2\text{Co}_{17}$  rather than  $\text{Nd}_2\text{Co}_{14}\text{B}$ . By systematically varying the composition of Nd–Co–B alloys, Fuerst

and Herbst successfully developed melt-spun  $\text{Nd}_2\text{Co}_{14}\text{B}$  ribbons with a coercivity of 1.02 T and energy product of 5.2 MGOe.<sup>[89]</sup> The authors also fabricated the ribbons comprised principally of  $\text{Pr}_2\text{Co}_{14}\text{B}$  with a coercivity of 2.5 T and energy product of 5.5 MGOe.<sup>[90]</sup> It should be mentioned that  $\text{RE}_2\text{Co}_{14}\text{B}$  compounds do not form for all rare earths but only for  $R = \text{Y, La, Pr, Nd, Sm, Gd, and Tb}$ . Unfortunately, none of them has attracted much attention due to their unsatisfied properties for permanent magnetic applications. In advanced Nd–Fe–B permanent magnets, Fe is only partially substituted by Co.

#### (iii) C substitution for B

The magnetic properties of the carbide and boride 2:14:1 compounds are almost same. Typically, carbides have slightly lower Curie temperatures and saturation magnetizations, slightly higher magnetocrystalline anisotropies, as shown in Table 5. The interest of  $\text{RE}_2\text{Fe}_{14}\text{C}$  phases is not only because of their intrinsic properties but also the presence of solid-state transformation, which offers the possibility of generating small-particle microstructures by controlling transformation of the high-temperature phase into the low-temperature phase. In another words, the nucleation and grain growth of the 2:14:1 phase in the  $\text{RE–Fe–C}$  systems is lower than that of  $\text{RE–Fe–B}$  systems, which should lead to finer microstructures. It has been found that  $\text{Nd}_2\text{Fe}_{14}\text{C}$  fabricated by melt spinning could easily provide a relatively high coercivity ( $\sim 10$  kOe) without the aid of other additives.<sup>[91]</sup> With a small portion of Co, Dy adoption, Zhang *et al.* reported an energy product of 11.5 MGOe with a coercivity of 2.7 T in the  $\text{Nd}_{13}\text{Dy}_2\text{Fe}_{67}\text{Co}_{10}\text{C}_6\text{B}_2$  melt-spun ribbons.<sup>[92]</sup> The energy product was further improved to 14.4 MGOe through optimizing post-annealing conditions.<sup>[93]</sup> Zhang *et al.* also studied the magnetic properties of  $\text{Pr}_{15}\text{Fe}_{77}\text{C}_{8-x}\text{B}_x$  ( $x = 0-8$ ) ribbons and found the high coercivity of 2.4 T in the  $\text{Pr}_{15}\text{Fe}_{77}\text{C}_4\text{B}_4$  ribbons without any heat treatment.<sup>[94]</sup>

#### (iv) Other additives

With no substantial cost increase, researchers found that the magnetic properties are improved by means of small amounts of additives in the 2:14:1 base materials. The most common additives are Ti, V, Cr, Mn, Co, Ni, Cu, Zr, Nb, Mo, Ru, W, Al, Ga, Si, etc. According to the summary in Ref. [83], the additions of Co, Ni, Cu, Ga, and Si increase the Curie temperature, while the additions of Nb, Al, and Si increase the magnetocrystalline anisotropy of  $\text{Nd}_2\text{Fe}_{14}\text{B}$  phase. More importantly, the additives can modify the microstructure in order to achieve desirable magnetic properties. For example, Herbst *et al.* found that the addition of 0.5 at.% Cu enhances the intrinsic coercivity as much as 30% over that of Cu-free materials, which is attributed to the Cu preferential segregation in the intergranular regions.<sup>[95]</sup> El-Moneim *et al.* observed that partial substitution of Fe with Co and Ga leads to an improvement

in corrosion resistance.<sup>[96]</sup> Chen *et al.* found that a small substitution of Nb for Fe results in a uniform microstructure with average grain size of only 10–20 nm, which is much smaller than the Nb-free ribbons.<sup>[97]</sup>

It should be emphasized again that the melt-spun materials based on 2:14:1 phase are typically isotropic which limits the maximum achievable energy products far lower than the theoretical value given in Table 5. Therefore, 2:14:1 phase usually exists as the magnetically hard phase in their nanocomposite magnets, which are discussed in section 3.2.

### 3.1.2. 1:5 phase

The CaCu<sub>5</sub>-type 1:5 phase can be formed in the RE–Co and RE–Ni compounds with the composition of RE(Co, Ni)<sub>5</sub>. However, the highest Curie temperature of –240 °C is found in the RENi<sub>5</sub> series for GdNi<sub>5</sub>, which makes them not practical for permanent magnet applications. On the other hand, Curie temperatures of most RECo<sub>5</sub> compounds are higher than 500 °C, as shown in Table 7. In addition, the extra-large magnetocrystalline anisotropy and the large magnetic moment of Co in the RECo<sub>5</sub> compounds make them good candidates for permanent magnets.

**Table 7.** Intrinsic magnetic properties and theoretical (BH)<sub>max</sub> limits of 1:5, 2:17 and other phases.<sup>[19,98,99]</sup>

Compound	$T_c/^\circ\text{C}$	$\mu_0 M_s/\text{T}$	$K_1/\text{MJ}\cdot\text{m}^{-3}$	$\mu_0 H_A/\text{T}$	Theo. (BH) <sub>max</sub> /MGOe
YCo <sub>5</sub>	630	1.06	5.5	13.0	28
LaCo <sub>5</sub>	567	0.91	6.3	17.5	20
CeCo <sub>5</sub>	380	0.77	6.4	21.0	15
PrCo <sub>5</sub>	620	1.20	8.1	17.0	36
NdCo <sub>5</sub>	637	1.22	0.24	5.0	37
SmCo <sub>5</sub>	727	1.14	11–20	25.0–44.0	32
SmCo <sub>4</sub> B	237	1.25	3.2	6.5	39
Sm <sub>2</sub> Co <sub>17</sub>	920	1.25	3.2	6.5	39
Sm <sub>2</sub> (Co <sub>0.7</sub> Co <sub>0.3</sub> ) <sub>17</sub>	840	1.45	3.0	5.2	52
Sm <sub>2</sub> Fe <sub>17</sub> N <sub>2.94</sub>	473	1.51	8.4	21.0	57
Sm <sub>2</sub> Fe <sub>17</sub> C	279	1.24	2.6	5.3	38
SmFe <sub>11</sub> Ti	312	1.16	3.4	7.36	34
SmFe <sub>10</sub> V <sub>2</sub>	337	1.10	2.1	4.80	30
Sm <sub>3</sub> (Fe, Ti) <sub>29</sub> N	475	1.18	5.6	12	35
Sm <sub>5</sub> Fe <sub>17</sub>	280	0.95	> 3.4	> 9.0	23

#### 3.1.2.1. SmCo<sub>5</sub>

Among RECo<sub>5</sub> compounds, SmCo<sub>5</sub> compounds are obvious candidates for developing coercivity, owing to their extraordinary magnetocrystalline anisotropy. However, the CaCu<sub>5</sub>-type 1:5 phase is stable only at temperature above 805 °C according to Sm–Co phase diagram,<sup>[100]</sup> below which it decomposes into Sm<sub>2</sub>Co<sub>7</sub> and Sm<sub>2</sub>Co<sub>17</sub> phases. The magnetocrystalline anisotropies of the 2:7 and 2:17 phases (~ 20 T and ~ 6–11 T, respectively) are less than that of 1:5 phase (25–44 T). In addition, the 2:7 phase can act as nucleation site of reversing domain wall, which decreases the coercivity of the SmCo<sub>5</sub> magnets. Therefore, fast cooling rate is necessary to obtain a pure single phase SmCo<sub>5</sub> magnet by suppressing the formation of the 2:7 and 2:17 phases, which makes the melt-spinning technique very suitable to fabricate the 1:5-type magnets.

Takahashi *et al.* prepared the melt-spun SmCo<sub>5</sub> ribbons in 1985,<sup>[101]</sup> where they found that the columnar structure with *c*-axis aligned parallel to the ejecting direction of the ribbons at relatively low wheel speed below 18 m/s. This is the so-called preferred crystallographic orientation or texture. In the ribbons fabricated at higher wheel speed, only homogenous spherical fine particles with random orientation of *c*-axis were

observed. Since the Co-rich part of the Sm–Co phase diagram does not have a deep eutectic, the melt spinning does not lead to an amorphous structure or even a very fine crystallized microstructure, which is the requirement for high coercivity. The coarse microstructure in typical Sm–Co melt-spun ribbons leads to a coercivity lower than that expected for a material with such a large anisotropy field. Therefore, it is understandable that the above work only achieves a coercivity up to 1.5 T,<sup>[101]</sup> which is even lower than that of the melt-spun Nd<sub>2</sub>Fe<sub>14</sub>B ribbons, although SmCo<sub>5</sub> has much higher magnetocrystalline anisotropy. Ding *et al.* optimized the melt spinning process for SmCo<sub>5</sub> ribbons and confirmed the dendritic structure with needle-like crystallites aligning preferentially in the ribbon plane in the low-speed prepared ribbons ( $v_{ws} < 20$ –30 m/s).<sup>[102]</sup> The coercivity of ribbons with such structure only have a low value of 0.96 T. Increasing wheel speed to  $\geq 30$  m/s leads to significantly increase of coercivity to 3.1 T due to the decrease of crystallite size, while with the sacrifice of texture in the ribbons. Suresh *et al.* reported a high coercivity of 5.3 T in the SmCo<sub>5</sub> ribbon melt-spun at 50 m/s, which has a small grain size of about 55 nm.<sup>[103]</sup>

Between the texture and the coercivity of melt-spun SmCo<sub>5</sub> ribbons, texture attracts more attention due to the demand of higher energy products. Therefore, most of the re-

cent efforts were focused on solidification at relatively low speeds. Actually, Ding *et al.* reported an energy product of 18 MGOe in the  $\text{SmCo}_5$  ribbons prepared at wheel speed of 6 m/s.<sup>[102]</sup> Yan *et al.* also reported the formation of crystallographic texture during melt-spinning process using low wheel speed.<sup>[104]</sup> The degree of the preferential alignment decreases at high wheel speed, while the ribbons prepared at  $v_{ws} > 20$  m/s are completely isotropic. Figure 13 shows the typical x-ray diffraction (XRD) patterns of the melt-spun  $\text{SmCo}_5$  ribbons prepared at low and high wheel speeds. The low-speed prepared ribbons clearly give very strong reflections of (200) and (110), while those of (111) and (002) are greatly weakened, comparing to the isotropic sample. This implies that the *c*-axis of crystallites prefers to be parallel to the longitudinal axis of the ribbon, which is different from the results reported for the  $\text{Nd}_2\text{Fe}_{14}\text{B}$  ribbon with the easy magnetization oriented normal to the ribbon plane.<sup>[105]</sup> However, a higher wheel speed leads to an XRD pattern with isotropic characteristic, as shown in Fig. 13(b). The authors also found that post-annealing significantly improves the magnetic properties. Owing to this texture, the performance of the ribbons is comparable with that of the anisotropic sintered  $\text{SmCo}_5$  magnets with  $\mu_0 M_r = 0.91$  T,  $\mu_0 H_c = 1.62$  T, and  $(\text{BH})_{\text{max}} = 18.2$  MGOe.

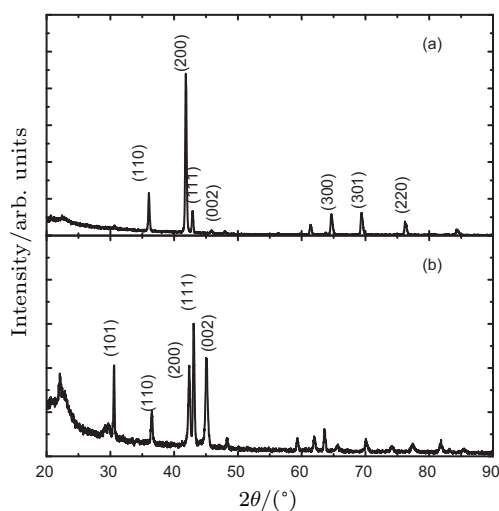


Fig. 13. XRD patterns of  $\text{SmCo}_5$  ribbons prepared at (a) 5 m/s and (b) 25 m/s.<sup>[104]</sup>

The element substitutions in  $\text{SmCo}_5$  ribbons influence both the microstructure and magnetic properties. Zhang *et al.* reported that Gd substitution of Sm could effectively suppresses the formation of 2:7 phase,<sup>[106]</sup> which usually exists in the anisotropic  $\text{SmCo}_5$  ribbons without element substitution.<sup>[107]</sup> The improved microstructure leads to the increase of both coercivity and squareness of the  $M$ - $H$  curve significantly. A high remanence ratio of 0.95 has been attained in  $\text{Sm}_{0.5}\text{Gd}_{0.5}\text{Co}_5$  ribbon with an energy product of 16 MGOe at room temperature. In addition, the temperature coefficient of remanence increases from  $-0.09\%$  per  $^\circ\text{C}$  for  $\text{SmCo}_5$  to  $+0.02\%$  per  $^\circ\text{C}$

for  $\text{Sm}_{0.5}\text{Gd}_{0.5}\text{Co}_5$  ribbons. This behavior could be attributed to the ferromagnetic coupling between HRE and Co atoms, which results in an increase of magnetization with increasing temperature in a given temperature range.

Enhanced saturated magnetization can be expected through Fe substitution to Co, as Fe has larger magnetic moment than Co. Tung *et al.* found that  $M_s$  of as-spun  $\text{SmCo}_5$  ribbons is only 0.42 T, while that of as-spun  $\text{SmCo}_3\text{Fe}_2$  ribbons is 1.20 T.<sup>[108]</sup> This huge enhancement cannot be only attributed the large magnetic moment of Fe. The TEM and energy dispersive analysis (EDX) analyses shows that a large portion of  $\text{SmCo}_3$  grain exists in the  $\text{SmCo}_5$  ribbons, which leads to low saturated magnetization in the ribbons. For the  $\text{SmCo}_3\text{Fe}_2$  ribbons, the majority phase is  $\text{Sm}(\text{Co}, \text{Fe})_5$  with a small portion of  $\text{Sm}_2(\text{Co}, \text{Fe})_7$  and  $\text{Sm}(\text{Co}, \text{Fe})_3$  phases at the grain boundaries. In addition, XRD suggests the existence of  $\alpha$ -Fe(Co) grains although it is not detected by TEM. Combining the grain refinement induced by the Fe substitution, a coercivity of 0.82 T and an energy product of 16 MGOe are obtained in the as-spun  $\text{Sm}(\text{CoFe})_5$  ribbons without post-annealing.

The nonmagnetic element substitution for Co has also been studied in the  $\text{SmCo}_5$  ribbons. Yan *et al.* studied the effects of Cu and Sm doping on the magnetic properties of the oriented melt-spun ribbons with composition  $\text{Sm}_{1+y}(\text{Co}_{1-x}\text{Cu}_x)_5$ , fabricated with a wheel speed of 5 m/s, followed by an optimized post-annealing.<sup>[109,110]</sup> The room temperature coercivity is significantly enhanced to 2.1 and 1.24 T by Sm additions and Cu substitution, respectively. Interestingly, it is found that the coercivity mechanism of the Sm-doped and Cu-substituted ribbons are completely different, i.e., the Sm-doped ribbon has a nucleation-type while Cu-substituted ribbon has a domain-wall pinning type coercivity mechanism. In addition, compared with the Sm-doped ribbons, Cu-doped ribbons exhibit a better thermal stability of coercivity and a high coercivity of 0.52 T even at 300  $^\circ\text{C}$ . Fukuzaki *et al.* investigated the effect of nonmagnetic element  $M$  ( $M = \text{Zr}, \text{V}, \text{Nb}, \text{Mo}, \text{and Ta}$ ) substitutions on magnetic properties and microstructure of  $\text{Sm}(\text{Co}_{0.7}\text{Cu}_{0.3})_5\text{Fe}_{0.54-x}\text{M}_x$  ribbons.<sup>[111]</sup> It is observed that the coercivity increases initially with increasing the substitution content, reaches a maximum value at  $x = 0.2$ – $0.3$ , and then decreases for all studied element except Zr, as shown in Fig. 14. The high melting point of Mo and Ta prevents the diffusion of these substitution elements from grain boundaries to  $\text{SmCo}_5$  grains, resulting to a high coercivity of 2.45 T in the Mo and Ta substituted ribbons.

Boron substitution of Co not only promotes amorphization in rapidly solidified Sm-Co alloys but also the formation of Sm-Co boride structures. The  $\text{SmCo}_4\text{B}$  compound, in which the B atoms replacing Co in the parent  $\text{SmCo}_5$  structure, has a magnetocrystalline anisotropy even higher than

SmCo<sub>5</sub>.<sup>[19]</sup> This makes SmCo<sub>4</sub>B a promising candidate for nanocrystalline hard magnet.

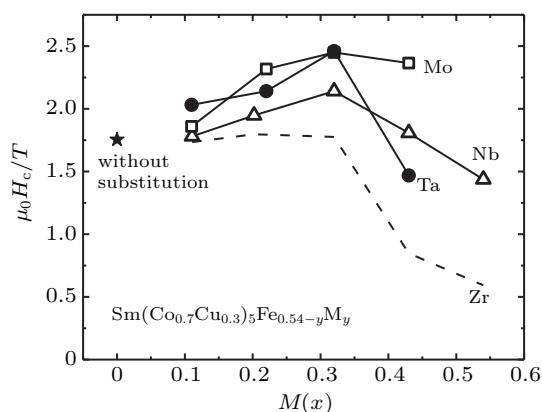


**Fig. 14.** Coercivity of Sm(Co<sub>0.7</sub>Cu<sub>0.3</sub>)<sub>5</sub>Fe<sub>0.54-x</sub>M<sub>x</sub> ( $M = \text{Zr, Nb, Mo, Ta}$ ) ribbons as a function of substitution element content.<sup>[111]</sup>

Unfortunately, the Curie temperature of SmCo<sub>4</sub>B is far lower than that of SmCo<sub>5</sub>. Two methods are utilized in order to improve the Curie temperature. Saito *et al.* found that melt spinning can stabilize the disordered SmCo<sub>5-x</sub>B<sub>x</sub> structure even with  $x < 1$ .<sup>[112]</sup> The value of  $T_c$  for the disordered compounds rapidly increases with decreasing B content from 197 °C at  $x = 1.0$  to 557 °C at  $x = 0.6$ . Besides the adjustment of B content, Satio *et al.*<sup>[112]</sup> and Gong *et al.*<sup>[113]</sup> both observed the increase of Curie temperature with Fe substitution for Co. Particularly,  $T_c$  of 472 °C is obtained in the SmCo<sub>2</sub>Fe<sub>2</sub>B ribbons. Therefore, there is a possibility of optimum hard-magnetic properties in metastable Sm(FeCo)<sub>5-x</sub>B<sub>x</sub> nanocrystalline alloys, though the realization of high-energy production is not likely to happen in these materials.

### 3.1.2.2. PrCo<sub>5</sub>

Hexagonal PrCo<sub>5</sub> has comparable anisotropy field and saturated magnetization to those of SmCo<sub>5</sub>, as shown in Table 7. It is the second choice among the RECo<sub>5</sub> compounds for permanent magnetic applications because of its large theoretical energy product of 36 MGOe and moderately high Curie temperature of 620 °C. However, the coercivity of PrCo<sub>5</sub> materials is rather low in comparison with the anisotropy field. A coercivity of only 0.6 T is achievable in the melt-spun PrCo<sub>5</sub> ribbons, as reported by Fuerst *et al.*<sup>[114]</sup> This mainly arises from the existence of impurity Pr<sub>2</sub>Co<sub>17</sub> and Pr<sub>5</sub>Co<sub>19</sub> phases with low anisotropy field, which are generated by the eutectoid reaction at 846 °C, according to the Pr–Co phase diagram.<sup>[115]</sup> Carbon addition could retard the formation of impurity phases and thus significantly improves coercivity, but decreases remanence. The highest coercivity obtained in the PrCo<sub>5</sub> and its carbon-doped ribbons is only 1.65 T with a rather low energy product of 7.4 MGOe so far.<sup>[114]</sup> To understand the reason for the low coercivity and investigate the possibility to improve it, Zhang *et al.* designed an melt spinning experiment with a

wheel speed up to 70 m/s.<sup>[116]</sup> Figure 15 compares the TEM images of melt-spun ribbons prepared by 30 m/s and 70 m/s and the corresponding statistical grain size distributions. The 30 m/s prepared ribbons give two characteristic maxima in the grain-size distribution where the first maximum represents impurity phases Pr<sub>2</sub>Co<sub>17</sub>/Pr<sub>5</sub>Co<sub>19</sub> with average grain size of about 110 nm and the second maximum originates from PrCo<sub>5</sub> phase with average grain size of about 290 nm. With increasing wheel speed to 70 m/s, only one maximum is observed in the grain size distribution, implying that the ribbons only consist of PrCo<sub>5</sub> phase with an average grain size of 19 nm. This indicates that the large increase of wheel speed fully impedes the formation of impurity phases and refines the nanostructure. Therefore the energy product of the 70 m/s ribbons increases almost twice compared to that of 30 m/s ribbons. A coercivity of 1.03 T and an energy product of 13.7 MGOe are achieved, which are the highest among the isotropic PrCo<sub>5</sub> ribbons. The coercivity value is close to that of nanocrystalline Pr<sub>2</sub>Fe<sub>14</sub>B, while the energy product is lower due to the lower saturated magnetization of PrCo<sub>5</sub> phase. However, PrCo<sub>5</sub> has much higher  $T_c$  than that of Pr<sub>2</sub>Fe<sub>14</sub>B, making melt-spun PrCo<sub>5</sub> ribbon a potentially good candidate for high-temperature application.

It is interesting to know that the texture could be developed through die-upsetting method for the PrCo<sub>5</sub> ribbons, which is similar to that of the Nd–Fe–B ribbons through plastic hot deformation procedure. Fuerst and Brewer observed this behavior in both Pr–Co and Pr–Co–C nanocrystalline ribbons with PrCo<sub>5</sub> as the major phase.<sup>[117,118]</sup> Although the texture is not as perfect as that in Nd–Fe–B magnets, it induces marked increase of remanence. The greatest alignment was obtained in the die-upset magnets with low-carbon compositions; in particular, Pr<sub>18</sub>Co<sub>81</sub>C produced a remanence of 0.87 T and an energy product of 16.9 MGOe.<sup>[117]</sup> Through further partially substituting Sm with Pr, coercivities near ~ 2.0 T were achieved in thermally quenched die-upset (Pr<sub>0.6</sub>Sm<sub>0.4</sub>)<sub>18</sub>Co<sub>81</sub>C magnets, while maintaining remanences above 0.8 T.<sup>[118]</sup> However, for unknown reasons, the Sm–Co alloys with much higher coercivity do not develop texture during die upsetting.

### 3.1.3. The 1:7 phase

1:7-type RECo<sub>7</sub> is a metastable phase in the RE–Co binary systems such as Sm–Co and Pr–Co. It has a TbCu<sub>7</sub> crystal structure which can be derived from RECo<sub>5</sub> when RE atoms are randomly substituted by Co pairs, confirmed by TEM study performed by Yu *et al.*<sup>[119]</sup> It should be noted that RE<sub>2</sub>Co<sub>17</sub> can also have the 1:7-type structure when they are prepared appropriately. A third doping element such as Ti, Zr, Cu, is helpful to stabilize the 1:7-type phase if they are used to substitute Co. Among the 1:7-type RE–Co alloys, SmCo<sub>7</sub>

is the most studied materials. The  $\text{SmCo}_7$  compound has saturation magnetization and Curie temperature lower than a  $\text{Sm}_2\text{Co}_{17}$  but higher than a  $\text{SmCo}_5$  compound. The anisotropy field of  $\text{TbCu}_7$ -type Sm-Co alloys is reported to be 10.5–14.0 T, which is about more than 1.6 times of the  $\text{Sm}_2\text{Co}_{17}$  phase.<sup>[120]</sup> In fact, the metastable  $\text{SmCo}_7$  phase can be obtained by various methods, such as arc melting,<sup>[121]</sup> mechanical alloying,<sup>[122]</sup> and melt spinning which is summarized here.

Various additions were tried to stabilize the 1:7 phase and refine the microstructure of  $\text{SmCo}_7$  ribbons. Guo *et al.* investigated the effect of transition metals (TM), such as Nb, Ta, Cr, and Mo, on the crystal structure and magnetic properties of melt-spun  $\text{SmCo}_{7-x}\text{TM}_x$ .<sup>[123,124]</sup> It was found that a pure  $\text{TbCu}_7$ -type structure is formed in the  $\text{SmCo}_{7-x}\text{Nb}_x$  and  $\text{SmCo}_{7-x}\text{Ta}_x$  ribbons, while minor amount of impurity 2:17

phase appears for the that of Cr or Mo substituted ribbons, implying that the elements in VIB group (Cr and Mo) are inferior to the element in VB group (Nb and Ta) in stabilizing metastable 1:7 phase. The impact of phase impurity is also reflected by the coercivity in the TM-substituted ribbons. The Nb/Ta substitution leads to the coercivity enhancement of 0.83–0.94 T, while Cr/Mo only leads to an enhancement of 0.47–0.56 T. The effect of Si and Al substitution in  $\text{SmCo}_7$  alloys has been investigated but the coercivity enhancement is much lower than that of Nb, Ta, Cr, and Mo.<sup>[125]</sup> Recent study shows that the coercivity can be highly enhanced in the  $\text{SmCo}_{7-x}\text{Zr}_x$  ribbons only if the wheel speed is high enough. Particularly, a high coercivity of 1.72 T is achieved in the  $\text{SmCo}_{6.7}\text{Zr}_{0.3}$  ribbon with a fine grain structure around 3  $\mu\text{m}$  if the wheel speed is 60 m/s and above.<sup>[126]</sup>

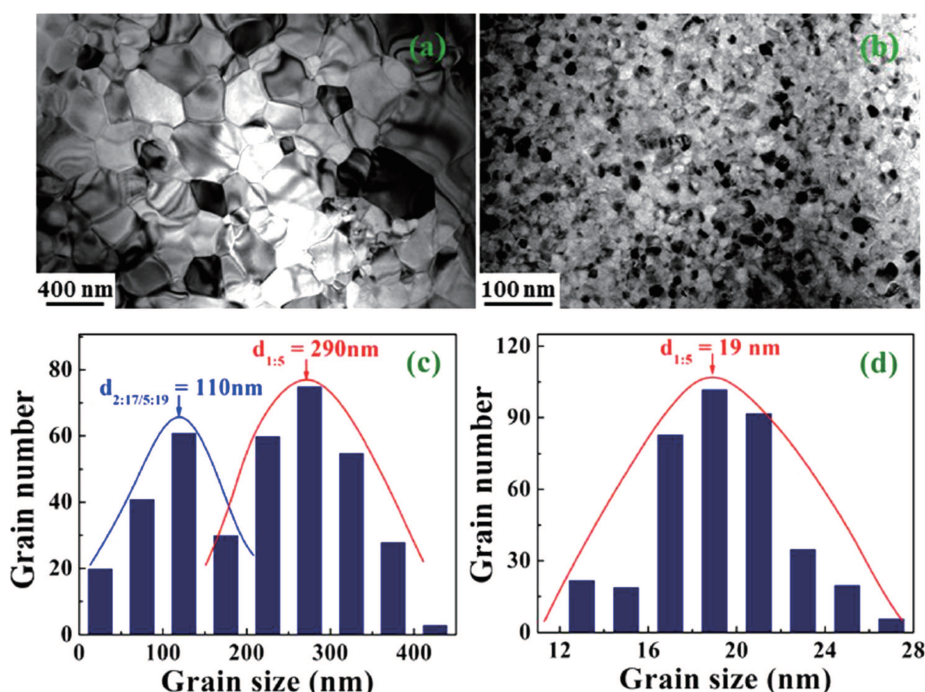


Fig. 15. (color online) TEM images of nanocrystalline  $\text{PrCo}_5$  prepared at (a) 30 m/s, (b) 70 m/s, and statistical grain size distribution of (c) 30 m/s, (d) 70 m/s.<sup>[116]</sup>

Carbon in combination with some transition metal element can produce fine 1:7 microstructures with further enhancement of coercivity. Du *et al.* found that carbon addition helps the formation of homogeneous microstructure with grain size around 60–70 nm in the  $\text{Sm}(\text{Co}_{0.9}\text{Fe}_{0.1})_{6.8}\text{Zr}_{0.2}\text{C}_x$  ribbons, which results in a coercivity of 1.43 T and an energy product of 11 MGOe.<sup>[127]</sup> With an optimized Fe content, the energy product is improved to 13.7 MGOe in the  $\text{Sm}(\text{Co}_{0.75}\text{Fe}_{0.25})_{6.7}\text{Zr}_{0.3}\text{C}_{0.06}$  ribbon, while coercivity is slightly dropped.<sup>[128]</sup> Similar grain refinement and coercivity enhancement are observed in the NbC-doped ribbons as reported by Hsiao *et al.*, confirming the role of carbon in the melt-spun 1:7-type alloys.<sup>[129]</sup> In fact, Li *et al.* found that the grain size of the melt-spun  $\text{SmCo}_{7-x}(\text{Cr}_3\text{C}_2)_x$  ribbons de-

creases with the increase of  $\text{Cr}_3\text{C}_2$  content.<sup>[130]</sup> The amorphous state is achieved in the ribbons with  $0.15 \leq x \leq 0.25$  when wheel speed is larger than 40 m/s. Magnetic properties can be further optimized by post-annealing of the amorphous ribbons.

Alternatively, boron can be doped into 1:7-type ribbons and significantly improves the coercivity. Makridis *et al.* reported that the as-spun  $\text{Sm}(\text{Co}_{0.74-x}\text{Fe}_{0.1}\text{Cu}_{0.12}\text{Zr}_{0.04}\text{B}_x)_{7.5}$  ribbons contains mainly  $\text{TbCu}_7$ -type phase with an average grain size of 60–100 nm.<sup>[131]</sup> A record high coercivity of 3.85 T at room temperature is achieved in these ribbons. It should be noted that excessive amount of B may lead to deterioration of the hard-magnetic properties. Kim *et al.* found that the magnetically soft  $\text{Sm}_2\text{Fe}_{14}\text{B}$  phase with a planar

anisotropy can be formed in the  $\text{Sm}_2(\text{CoFeMn})_{17}\text{B}_x$  ribbons if B is over-doped.<sup>[132]</sup>

$\text{TbCu}_7$  structure is observed in the Pr–Co alloys as well. Zhang *et al.* reported the stabilized 1:7 phase in both compound through arc melting<sup>[133]</sup> and nanocrystalline powders with an average grain size of 20 nm through mechanical alloying of  $\text{PrCo}_{7-x}\text{Ti}_x$  alloys with an energy product of 10.6 MGOe.<sup>[134]</sup> With the assistance of C addition, Kostogorova *et al.* successfully fabricated the  $(\text{Pr}_x\text{Co}_{1-x})_{94}\text{Ti}_3\text{C}_3$  ribbons consisting of 1:7 phase with a coercivity around 1.0 T through melt spinning and post-annealing.<sup>[135]</sup>

Besides microstructure refinement, the improvement of crystallographic texture in the melt-spun ribbons is also an effective way to promote the properties of 1:7-type magnets. Yan *et al.* observed a high degree of texture in the melt-spun  $\text{Sm}(\text{CoFeCuZr})_{7.4}$  ribbons prepared at low wheel speed such as 5 m/s.<sup>[136]</sup> The formation of the crystallographic texture, with *c*-axis parallel to the longitudinal direction of ribbon, is attributed to a directional solidification process resulting from a temperature gradient. Maximum energy product of 12.3 MGOe is obtained in such highly-textured ribbons. Yan *et al.* also found that the C addition to  $\text{Sm}(\text{CoZr})_7$  alloy not only significantly enhances the coercivity of the ribbons but also affects the crystallographic texture. The preferred orientation changes from parallel to the ribbon plane for carbon-free ribbon, to normal to the ribbon plane for the  $\text{SmCo}_{6.5}\text{Zr}_{0.5}\text{C}_{0.5}$  ribbon.<sup>[137]</sup> Figure 16 shows the scanning electron micrograph (SEM) images of ribbons with and without carbon. The analysis shows that a dendrite structure was presented in the  $\text{SmCoZr}$  ribbon surface, while C addition leads to the diminishing of the dendrite and the grains become equiaxial. A higher energy product of 8.6 MGOe is observed in the C-added ribbon prepared at 5 m/s.

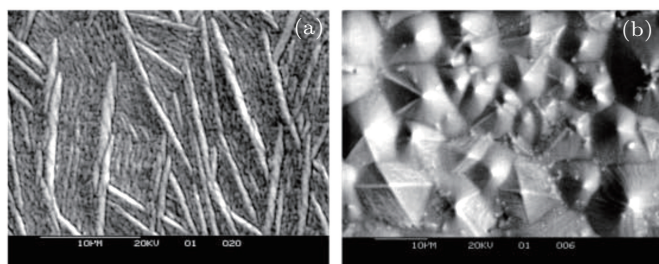


Fig. 16. SEM micrographs on the surface of (a)  $\text{SmCo}_{6.5}\text{Zr}_{0.5}$  and (b)  $\text{SmCo}_{6.5}\text{Zr}_{0.5}\text{C}_{0.5}$  ribbons.<sup>[137]</sup>

### 3.1.4. The 2:17 phase

Since the  $\text{Sm}_2\text{Co}_{17}$  and especially  $\text{Sm}_2(\text{CoFe})_{17}$  have saturated magnetization substantially higher than that of  $\text{SmCo}_5$ , it seems natural to increase  $(\text{BH})_{\text{max}}$  in the  $\text{Sm}_2\text{Co}_{17}$  magnets. Another advantage of  $\text{Sm}_2\text{Co}_{17}$  is the higher Curie temperature compared to  $\text{SmCo}_5$  phase, as seen in Table 7. Unfortunately, Chen *et al.* found that the coercivity of  $\text{Sm}_2(\text{Co}, \text{Fe})_{17}$

ribbons is less than 0.3 T, although they found that the coercivity increase with increasing wheel speed and a crystallographic texture formed during the melt-spinning process,<sup>[138]</sup> which is similar to the behaviors observed in  $\text{SmCo}_5$  ribbons. The low coercivity might be expected, since the anisotropy field of  $\text{Sm}_2\text{Co}_{17}$  is only about one-fourth of that of  $\text{SmCo}_5$ . However, the major reason for the low coercivity appears to be related to a coarse dendritic microstructure with their long axis parallel to the longitudinal direction of the ribbons.<sup>[139]</sup> The size and alignment of the dendritic grains can be significantly modified through Cu and Zr substitution for Co. With an appropriate annealing, a coercivity of over 2.5 T has been obtained in the Cu and Zr substituted  $\text{Sm}_2(\text{CoFe})_{17}$  ribbons. However, these high coercivities cannot be attributed to the 2:17 solely. Instead, it should be attributed to the two-phase cellular structure, similar to that of conventional precipitation-type  $\text{Sm}(\text{Co}, \text{Cu}, \text{Fe}, \text{Zr})_z$  magnets, which leads to the domain-wall pinning mechanism in the ribbons.<sup>[139]</sup> On the other hand, Crabbe *et al.* studied the melt-spun  $\text{Sm}(\text{Co}_{0.704}\text{Cu}_{0.061}\text{Fe}_{0.209}\text{Zr}_{0.025})_{7.61}$  ribbons with a single-phase 2:17 microstructure and a grain size of about 30 nm, through controlling wheel speed and nozzle diameter during melt-spinning process. Unfortunately, their magnetic properties are still at the low end with  $\mu_0M_r = 0.52\text{--}0.75$  T,  $\mu_0H_c = 0.3\text{--}0.5$  T,  $(\text{BH})_{\text{max}} = 4.4\text{--}10$  MGOe.<sup>[140]</sup> There are not many researches on the melt spinning of  $\text{Sm}_2(\text{CoFe})_{17}$  alloys with single-phase microstructure due to their poor hard magnetic properties and thus lack of potential applications. In fact, the melt-spun 2:17 ribbons with two-phase cellular microstructure have attracted interests, which will be discussed in Section 3.3.

### 3.1.5. The 2:17 interstitial phase

$\text{Sm}_2\text{Fe}_{17}$  compound has high saturation magnetization but shows low Curie temperature and planar anisotropy likely due to the strong Fe sublattice anisotropy. However, interstitial modification of the  $\text{Sm}_2\text{Fe}_{17}$  compounds can lead to uniaxial anisotropy and dramatically change their magnetic properties.<sup>[99,141]</sup> Owing to a volume expansion of the atomic lattice caused by the absorbed N, C, or H atoms, the Curie temperature increases by more than 300 °C. In addition, both magnetocrystalline anisotropy and saturation magnetization also increase significantly, as shown in Table 7. For  $\text{Sm}_2\text{Fe}_{17}\text{N}_{2.94}$ , a value for the anisotropy field of 21 T at room temperature has been reported by Katter *et al.*<sup>[99]</sup> These excellent magnetic properties were immediately realized in high-performance nanocrystalline magnets. However, these nitrides or carbides prepared by gas-phase interstitial modification are metastable, and decompose into Sm–N or Sm–C and  $\alpha$ -Fe upon heating to about 700 °C and cannot be used for the development of anisotropic sintered magnets.

### 3.1.5.1. $\text{Sm}_2\text{Fe}_{17}$ nitride

Pinkerton and Fuerst obtained magnetically hard Sm–Fe–N ribbons with a room-temperature coercivity of 2.3 T by nitriding melt-spun Sm–Fe precursor ribbons. To facilitate the absorption of nitrogen, the ribbons were ground to powder with particle size less than 25  $\mu\text{m}$ , then heat treated in vacuum for 1 h at 700  $^\circ\text{C}$  prior to nitriding in  $\text{N}_2$  gas at 450–480  $^\circ\text{C}$ .<sup>[142]</sup> Katter *et al.* studied the structure and magnetic properties of the Sm–Fe ribbons in the as-quenched state and after nitriding.<sup>[143]</sup> It was found that a hexagonal  $\text{TbCu}_7$ -type phase only shows up in melt spun ribbons with a stoichiometry of about  $\text{SmFe}_9$  and at wheel speed above 15 m/s. At higher Sm concentrations or lower quenching rates the structure changes to the  $\text{Th}_2\text{Zn}_{17}$ -type. Both phases give very low coercivity, while nitrogenation leads to an expansion of the lattice and to an overall improvement of the hard magnetic properties for both phases, i.e., their Curie temperatures increase to 470  $^\circ\text{C}$  and the saturated magnetizations raise to 1.40 and 1.51 T for the  $\text{TbCu}_7$ -type and the  $\text{Th}_2\text{Zn}_{17}$ -type phases, respectively. It was also found that Nb or Zr additions can stabilize the 1:7 structure in the melt-spun Sm–Fe ribbons, while the samples without substitutions crystallize in the  $\text{Th}_2\text{Zn}_{17}$ -type structure.<sup>[144]</sup>

Shield *et al.* found that melt spinning of the  $\text{Sm}_{11}\text{Fe}_{89}$  alloys usually results in grain sizes at or above the single domain limit which is around 360 nm.<sup>[145]</sup> The addition of Ti and C leads to an order of magnitude refinement at the microstructural scale, resulting in the coercivity enhancement in the  $\text{Sm}_2\text{Fe}_{17}\text{N}_x$  ribbons. Omatsuzawa *et al.* investigated the isotropic  $\text{TbCu}_7$ -type Sm–Zr–Fe–Co–N materials prepared by the melt spinning and following nitrogenation.<sup>[146]</sup> They found that the grain size decreased monotonically with the increase of the wheel speed, which leads to the increase of both remanence and coercivity. A compression-molded bonded magnet using the melt-spun powders at a wheel speed of 40 m/s showed excellent magnetically hard properties:  $\mu_0M_r = 0.83$  T,  $\mu_0H_c = 0.9$  T, and  $(\text{BH})_{\text{max}} = 14.2$  MGOe. Even better properties were reported in the  $(\text{Sm}_{0.7}\text{Zr}_{0.3})(\text{Fe}_{0.8}\text{Co}_{0.2})_9\text{B}_{0.1}\text{N}_x$  ribbons with a single-phase  $\text{TbCu}_7$ -type structure:  $\mu_0M_r = 1.07$  T,  $\mu_0H_c = 0.98$  T, and  $(\text{BH})_{\text{max}} = 22.6$  MGOe.

### 3.1.5.2. $\text{Sm}_2\text{Fe}_{17}$ carbide

The effect of interstitial carbon on  $\text{Sm}_2\text{Fe}_{17}$  is similar to that of nitrogen. However, the number of the C atoms per formula unit after a solid–gas carburization usually does not exceed 2. This means a lesser volume expansion of the 2:17 lattice and thus lesser gain in the magnetic properties. As one can see in Table 7, both Curie temperature and anisotropy field of Sm–Fe–C are lower than those of Sm–Fe–N. However, there are several advantages of Sm–Fe–C comparing to

Sm–Fe–N: i) the  $\text{Sm}_2\text{Fe}_{17}\text{C}_x$  system can be directly produced by the simple melt spinning without the two-step procedure in Sm–Fe–N system. ii) The melt-spun Sm–Fe–C ribbons have better phase thermal stability compared to the alloys prepared by solid–gas reaction. iii) The interstitial carbides  $\text{Sm}_2\text{Fe}_{17}\text{C}_x$  with higher carbon concentration can be formed by melt spinning, which leads to higher Curie temperature and larger magnetocrystalline anisotropy.

Shen and his group have systematically studied the structure and magnetic properties of the  $\text{RE}_2\text{Fe}_{17}\text{C}_x$  ( $\text{RE} = \text{Dy}, \text{Er}, \text{Ho}, \text{Er}, \text{Ge}, \text{Tm}, \text{Y}$ ) ribbons prepared by melt spinning and other approaches.<sup>[147–157]</sup> The Curie temperatures of  $\text{RE}_2\text{Fe}_{17}\text{C}_x$  are summarized in Fig. 17. A considerable enhancement of  $T_c$  is observed when  $x$  increases from 0 to 2.0. For small  $x$ -values, the Curie temperature increases with increasing carbon concentration more drastically than for larger  $x$ -values. In addition, there is a linear relation between  $T_c$  and the corresponding unit cell volumes, as shown in Fig. 17(b). It demonstrates the dependence of the exchange interaction on unit cell volume in the 2:17 structure. Figure 17(c) summarizes the dependence of room-temperature saturated magnetization on carbon concentration of  $\text{RE}_2\text{Fe}_{17}\text{C}_x$  ribbons. It was found that  $M_s$  increases with increasing  $x$  for low carbon concentration, while it becomes flat for high carbon concentration. The increase of  $M_s$  at lower carbon concentration is due to the enhancement of the Curie temperature which shifts the thermomagnetization curve to higher temperature. It should be noted that the substitution of Ga in  $\text{Sm}_2\text{Fe}_{17}$  also increases Curie temperatures and develops a room temperature uniaxial anisotropy without introducing interstitial carbon or nitrogen atom.<sup>[158]</sup> Unfortunately, no considerable coercivity is reported in the above mentioned Sm–Fe based ribbons.

Among all  $\text{RE}_2\text{Fe}_{17}\text{C}_x$  alloys,  $\text{Sm}_2\text{Fe}_{17}\text{C}_x$  is the best candidate for permanent magnets due to their high saturation magnetization and relatively high Curie temperature. It was found later by Shen *et al.* that substituting Fe partially with Ga, Al, Si, or Cr in  $\text{Sm}_2\text{Fe}_{17}\text{C}_x$  helps the formation of Sm–Fe compounds of even higher carbon content with the 2:17-type structure.<sup>[159–161]</sup> The excellent magnetic properties of these 2:17-type carbides results from not only the interstitial carbon atoms but also the substitutional Ga, Al, or Si atoms, which leads to a significant increase in the uniaxial anisotropy field.

Figure 18 summarizes the intrinsic magnetic properties of  $\text{Sm}_2\text{Fe}_{15}\text{M}_2\text{C}_x$  ( $M = \text{Ga}, \text{Al}, \text{Si}$ ) alloys, which were reported in Refs. [161]–[163] Similar to the contribution of carbon addition to  $\text{Sm}_2\text{Fe}_{17}\text{C}_x$  ribbons, carbon leads to the increases of Curie temperature in all  $\text{Sm}_2\text{Fe}_{15}\text{M}_2\text{C}_x$  alloys and reaches the maximum around  $x = 1.5 \sim 2.0$ . The Ga, Al, and Si substitutions themselves also enhance the Curie temperatures, as shown in Fig. 18(a). Figure 18(b) presents the dependence of anisotropy field  $H_A$  on carbon content. It shows that carbon

addition leads to dramatic increase of  $H_A$  as  $x < 1.0$ , and then increases slowly or even deteriorates with excess carbon addition. Unfortunately, carbon addition leads to the monotonic decrease of saturated magnetization for all Ga, Al and Si substitution, although it benefits the  $\text{Sm}_2\text{Fe}_{17}\text{C}_x$  alloys, as shown

in Fig. 18(c). For this reason, the carbon content was usually chosen between  $x = 1.0\text{--}2.0$  to gain the benefits of  $T_c$  and  $H_A$  but not scarify too much saturated magnetization. Comparing with  $\text{Nd}_2\text{Fe}_{14}\text{B}$ , the  $\text{Sm}_2\text{Fe}_{15}\text{Ga}_2\text{C}_x$  materials have higher  $T_c$  and  $H_A$ , but lower saturated magnetization.

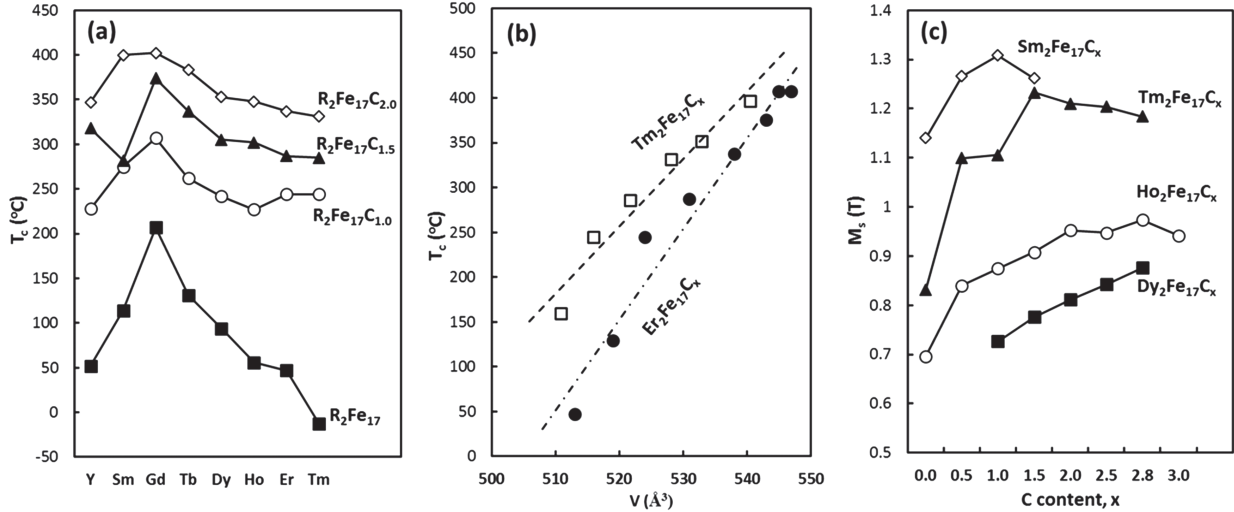


Fig. 17. (a) Curie temperatures of  $R_2\text{Fe}_{17}\text{C}_x$  ribbons ( $x = 0, 1.0, 1.5, \text{ and } 2.0$ ); (b) Curie temperatures versus unit cell volume of  $\text{Er}_2\text{Fe}_{17}\text{C}_x$  and  $\text{Tm}_2\text{Fe}_{17}\text{C}_x$ ; (c) dependence of  $M_s$  on carbon content of  $R_2\text{Fe}_{17}\text{C}_x$  ribbons.<sup>[147–157]</sup>

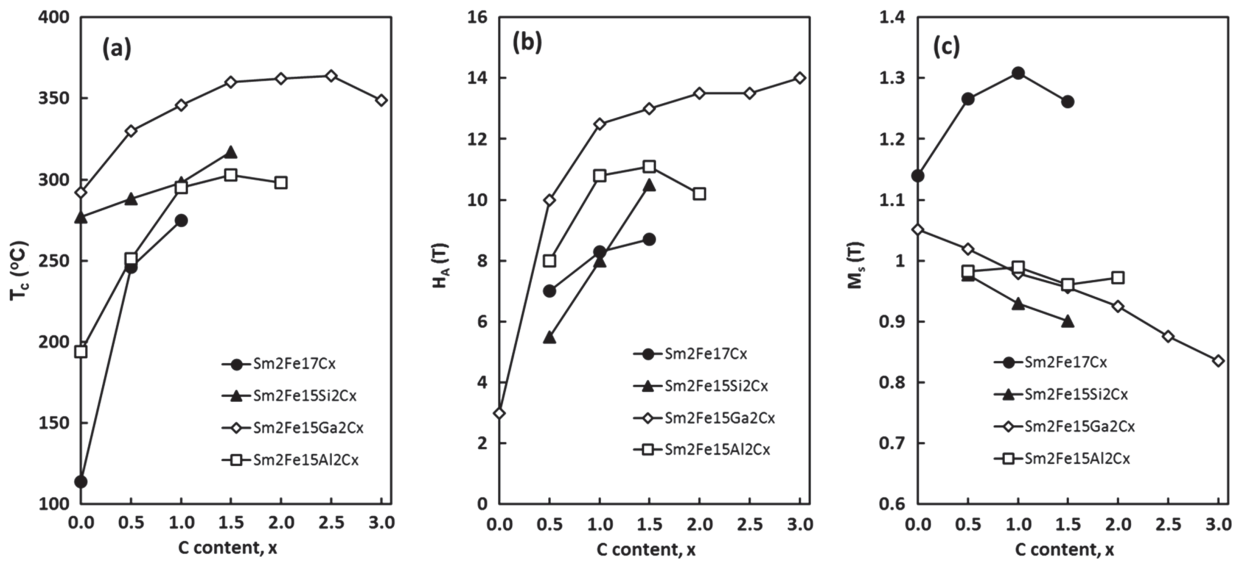
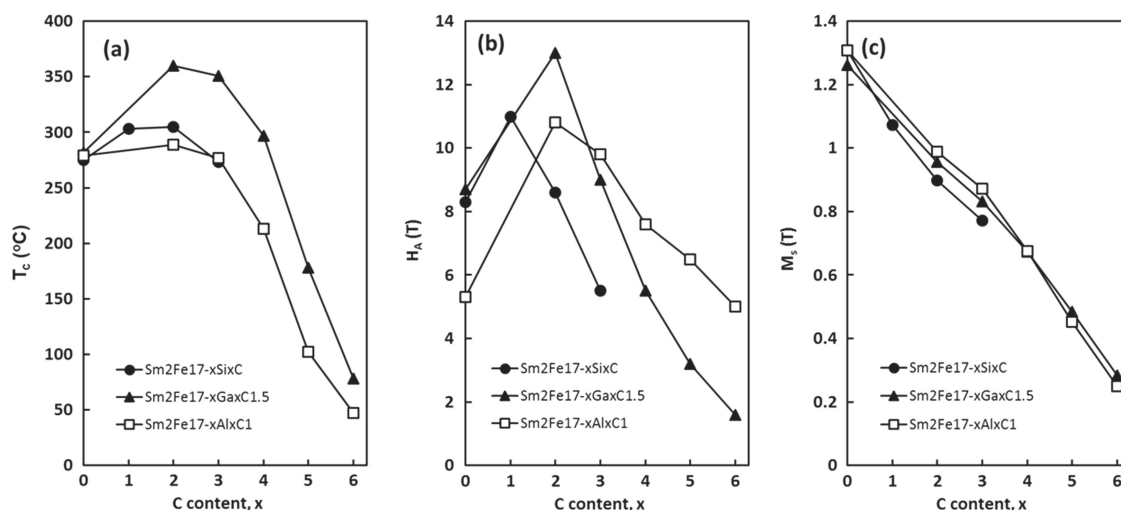


Fig. 18. Effect of carbon addition on (a)  $T_c$ , (b)  $H_A$ , and (c)  $M_s$  of  $\text{Sm}_2\text{Fe}_{17}\text{C}_x$  and  $\text{Sm}_2\text{Fe}_{15}\text{M}_2\text{C}_x$  alloys.<sup>[161–163]</sup>

With an optimized carbon content, Shen and his group further optimized the Ga, Al, and Si substitutions on intrinsic magnetic properties of  $\text{Sm}_2\text{Fe}_{15}\text{M}_x\text{C}_{1.0\text{--}1.5}$  alloys,<sup>[164,165]</sup> as shown in Fig. 19. It was found that maximum Curie temperature and anisotropy field are obtained in the alloys with  $x$  around 2, while they drop quickly with excess Ga/Al/Si substitutions. The saturated magnetization decrease almost linearly with the amount of substitution in a fast manner. Further substitution for Fe with transition metals such as Cu, Nb, V, Mo, Zr, Ti in  $\text{Sm}_2(\text{Fe}, \text{TM})_{15}\text{Ga}_2\text{C}$  ribbons shows

that they all deteriorates the Curie temperature, anisotropy field, and saturated magnetization.<sup>[166]</sup> It should be noted that the Co substitution for Fe leads to monotonic increases of both Curie temperature and saturated magnetization in  $\text{Sm}_2\text{Fe}_{15-x}\text{Co}_x\text{Si}_2\text{C}$  ribbons if  $x < 5$ , while anisotropy field does not change much.<sup>[167]</sup> Additional studies have also been conducted on the effect of Ga substitution on the intrinsic magnetic properties of  $R_2\text{Fe}_{15-x}\text{Ga}_x\text{C}_2$  ( $R = \text{Gd}, \text{Y}, \text{Ho}, \text{Er}$ ) alloys, while similar behaviors as those in  $\text{Sm}\text{--}\text{Fe}\text{--}\text{Ga}\text{--}\text{C}$  system are observed.<sup>[164,168–171]</sup>



**Fig. 19.** The effect of Ga, Si, and Al substitutions on (a) Curie temperature, (b) anisotropy field, and (c) saturated magnetization of  $\text{Sm}_2\text{Fe}_{15}\text{M}_x\text{C}_{1.0-1.5}$  alloys. [172,173]

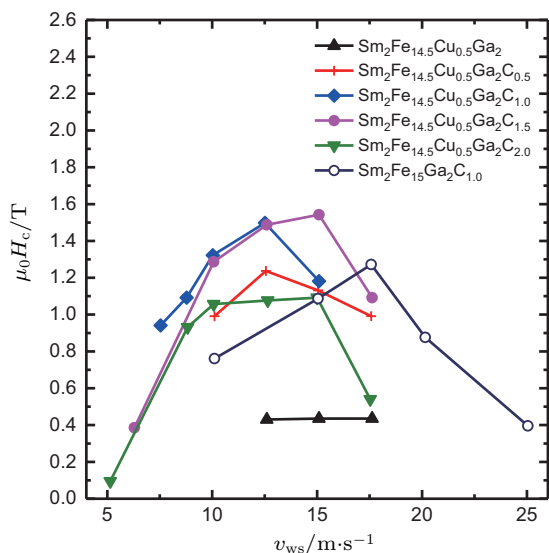


**Fig. 20.** (color online) Dependence of coercivity on wheel speed of  $\text{Sm}_2\text{Fe}_{15-x}\text{Cu}_x\text{Ga}_2\text{C}_x$  ( $x = 0-2.0$ ) and  $\text{Sm}_2\text{Fe}_{15}\text{Ga}_2\text{C}$  ribbons. [174]

Compared with  $\text{Sm}_2\text{Fe}_{17}\text{C}_x$ , the further advantage of  $\text{Sm}_2\text{Fe}_{15}\text{M}_2\text{C}$  materials is the developed coercivity and energy products. Zhang *et al.* studied the effects of wheel speed of melt spinning as well as the carbon content on the coercivity of the  $\text{Sm}_2\text{Fe}_{14.5}\text{Cu}_{0.5}\text{Ga}_2\text{C}_x$  ribbons, [174] as shown in Fig. 20. The coercivity increases significantly with increasing carbon content and reaches a maximum at  $x = 1.0-1.5$  for an optimized wheel speed of about 12.5–15 m/s. The maximum coercivity at room temperature is 2.2 T for  $\text{Sm}_2\text{Fe}_{14.5}\text{Cu}_{0.5}\text{Ga}_2\text{C}_{1.5}$  ribbon. It should be noted that the coercivity shown in Fig. 20 is measured by a vibrating sample magnetometer (VSM) with a maximum applied field of 1.9 T, without reaching the saturation magnetization of the samples. The coercivity could be further improved to 2.6 T if the ribbon was annealed in a Sm atmosphere. [175] With a small portion of Sm substituted by Pr, energy product of about 8.9 MGOe was obtained in the single-phase Sm–Fe–Ga–C ribbons. [176] For Sm–Fe–Si–C ribbons, a coercivity about 1.5 T and an energy product of

about 7.2 MGOe are achieved through Cu or Co substitution with optimized melt-spinning process. [167,177] Such melt-spun Sm–Fe–(Ga, Si)–C ribbons usually have a fine microstructure with grain size of about 45–60 nm while the magnetic domain size is about 100–500 nm, indicating the effective exchange coupling between grains.

### 3.1.6. The 1:12, 3:29, and 5:17 phases

$\text{Sm}(\text{Fe}, M)_{12}$  ( $M = \text{Ti}, \text{V}, \text{Mo}, \text{Si}$ ) compounds with the tetragonal  $\text{ThMn}_{12}$  structure possess a uniaxial anisotropy at room temperature, which is large enough for the development of permanent magnet materials. Both melt spinning and ball milling were utilized to produce nanocrystalline  $\text{Sm}(\text{Fe}, M)_{12}$  magnets. The  $\text{SmFe}_{12-x}\text{M}_x$  magnets with the desired 1:12 structure can be obtained if  $x \geq 1$  for Ti-substitution and if  $x \geq 1.5$  for V-substitution magnets.  $\text{SmFe}_{12-x}\text{M}_x$  is metastable phase which makes melt spinning suitable for development of such materials with nanostructures. Wang *et al.* studied the effects of V substitution on the magnetic properties of Sm–Fe–Ti–V melt ribbons. A coercivity of about 1.07 T is obtained in the melt-spun  $\text{Sm}_8\text{Fe}_{75.5}\text{Ga}_{0.5}\text{Ti}_8\text{V}_8$  with a  $\text{ThMn}_{12}$ -type structure after post annealing, which is far higher than that of bulk magnets prepared by the powder metallurgy technique. [178] A higher coercivity is reported in the  $\text{SmFe}_{10}\text{TiV}$  ribbons after annealing in Sm atmosphere, where such annealing technique is specially aimed to prevent the evaporation losses of Sm. [179] Pinkerton *et al.* also reported a bulk  $\text{Sm}_{0.89}\text{Fe}_{10}\text{V}_2$  magnet prepared by hot compaction of the overquenched ribbons with bulk magnetic properties:  $\mu_0 M_r = 0.54$  T,  $\mu_0 H_c = 0.78$  T,  $(\text{BH})_{\text{max}} = 4$  MGOe. With partial Co substitution for Fe, an energy product of about 8.4 MGOe is obtained in the  $\text{Sm}(\text{Fe}, \text{Co}, \text{Ti})_{12}$  ribbons. [180]

Interstitial modification of the  $\text{Nd}(\text{Fe}, M)_{12}$  compounds changes their intrinsic magnetic properties in a way very similar to that of  $\text{Sm}_2\text{Fe}_{17}$ . The room-temperature coercivity of

about 0.6–0.9 T are obtained by nitriding the melt-spun Nd(Fe, Mo)<sub>12</sub> ribbons which only have coercivity less than 0.05 T prior to nitriding.<sup>[181]</sup> The magnetic properties and interstitial atom effects in the  $R(\text{Fe}, M)_{12}$  compounds have been reviewed in Ref. [182].

$R_3(\text{Fe}, \text{Ti})_{29}$  is a novel intermetallic which crystallizes into a monoclinic structure with a space group of  $A2/m$ . The unit cell can be described as an alternate stacking of the tetragonal  $\text{ThMn}_{12}$ -type and the rhombohedral  $\text{Th}_2\text{Zn}_{17}$ -type structures. There is a strong enhancement in saturated magnetization and Curie temperature ( $T_c > 450$  °C in the nitride) upon nitrogenation while the easy magnetization direction changes from planar to uniaxial. The anisotropy field about 12 T at room temperature is reported in the  $\text{Sm}_3(\text{Fe}, \text{Ti})_{29}$  nitrides.<sup>[183]</sup> Chen *et al.* fabricated the  $\text{Sm}_3\text{Fe}_{27.5}\text{Ti}_{1.5}$  ribbons via melt spinning with controlled cooled rate.<sup>[184]</sup> It was found that 3:29 only forms at low wheel speed of 5–10 m/s, while 1:7 phase was developed at higher wheel speed of 20–25 m/s and amorphous phase became dominant with increased speed to 40 m/s. The best magnetic properties  $\text{Sm}_3\text{Fe}_{27.5}\text{Ti}_{1.5}$  ribbons are  $\mu_0 M_r = 0.72$  T,  $\mu_0 H_c = 0.15$  T,  $(\text{BH})_{\text{max}} = 2.9$  MGOe, which is not very promising, even after optimized post-annealing and nitrogenation.

$\text{Nd}_5\text{Fe}_{17}$  phase was found to be a stable intermetallic compound with a hexagonal structure in the binary Nd–Fe system. Although the  $\text{Nd}_5\text{Fe}_{17}$  phase has a high saturated magnetization of 1.52 T at 4 K and a Curie temperature of 230 °C, it does not possess  $c$ -axis anisotropic, which is essential for permanent magnet materials. On the other hand,  $\text{Sm}_5\text{Fe}_{17}$  phase is a metastable phase with a Curie temperature around 280 °C and an anisotropy field  $> 9$  T. The single-phase  $\text{Sm}_5\text{Fe}_{17}$  with two elements was first observed in the sputtered films with a coercivity of 1.47 T at room temperature.<sup>[185]</sup> Although it was found later that  $\text{Sm}_5\text{Fe}_{17}$  phase can be obtained through melt spinning,<sup>[186]</sup> partial replacement of Fe by Ti and/or V could greatly favor the formation of the 5:17 phase. The ternaries around  $\text{Sm}_{20}\text{Fe}_{70}\text{Ti}_{10}$  are the most studied alloys with the 5:17 structure. Saito *et al.* reported a coercivity of 4.0 T in the  $\text{Sm}_5\text{Fe}_{17}$  ribbons consisted of grains around 50–100 nm.<sup>[187]</sup> Unfortunately, the remanence of these ribbons is only about 0.48 T, which does not favor the permanent magnet applications.

### 3.1.7. RE-free phases

Recent constraints on availability and cost increase of RE elements have stimulated a strong interest in the discovery of RE-free materials with excellent permanent-magnet properties. Many RE-free candidates with high magnetic anisotropy and high Curie temperature have been proposed and studied in the past years. Here we only briefly reviewed some of them such as MnBi, Co-rich Hf–Co/Zr–Co, Fe–Pt–B, Mn–Al–C and Alnico, which are prepared by melt spinning.

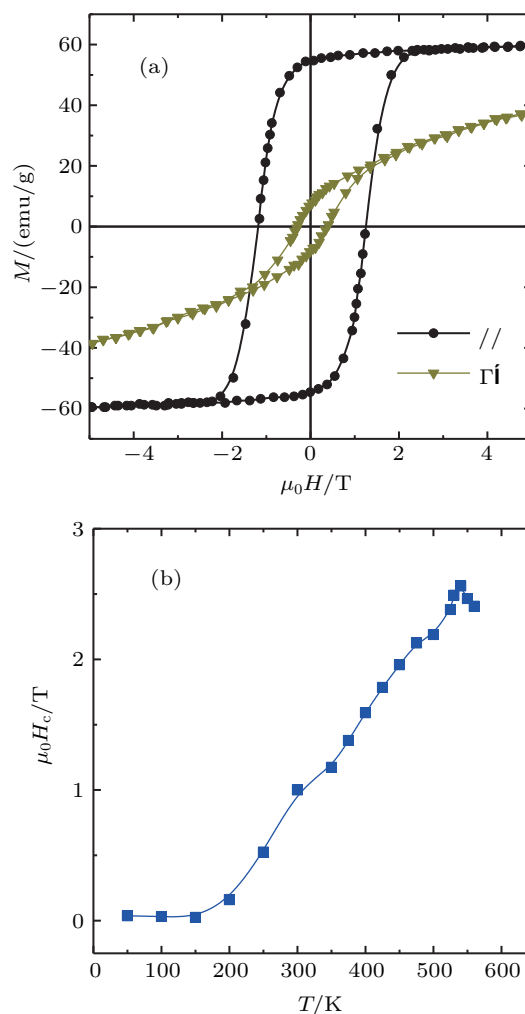


**Fig. 21.** (color online) The magnetic properties of nanocrystalline MnBi. (a) The hysteresis loops of MnBi at room temperature along the directions parallel and perpendicular to the  $c$ -axis; (a) the temperature dependence of coercivity.<sup>[190]</sup>

The low temperature phase (LTP) MnBi compound is of interest not only because of its RE-free feature, but also because of its magnetic properties. The magnetic anisotropy constant of MnBi is negative below  $-170$  °C but increases with increasing temperature and attains its maximum value of  $2.2 \times 10^6$  J/m<sup>3</sup> at 220 °C. Actually, the high temperature anisotropy constant of MnBi is much higher than that of  $\text{Nd}_2\text{Fe}_{14}\text{B}$  phase, although its room temperature value is lower. This made MnBi a good candidate for high temperature applications. However, the maximum energy product of MnBi at room temperature is much lower than most other permanent magnet materials, due to its low saturated magnetization. Guo *et al.* prepared the LTP MnBi by melt spinning and found a maximum anisotropy field of about 9 T at 257 °C and a Curie temperature of about 500 °C.<sup>[188]</sup> Following the above method, Saha *et al.* produced the MnBi powders with a coercivity of about 2.6 T at 280 °C by a ball milling process following the melt-spinning.<sup>[189]</sup> The saturated magnetization and remanence of these ribbons or powders are relative low. Yang *et al.* optimized melt spinning and annealing

processes of the MnBi ribbons.<sup>[190]</sup> They found that the grain size of 200 nm in the 20 m/s spun ribbons can be reduced to 20–30 nm with increasing wheel speed to 65 m/s. With a grinding process followed by alignment under magnetic field, an anisotropic nanocrystalline MnBi magnet is obtained with an energy product of 7.1 MGOe. The hysteresis loops of the anisotropic MnBi magnets are given in Fig. 21(a) along the directions parallel and perpendicular to the *c*-axis. The temperature dependence of the coercivity is shown in Fig. 21(b), which exhibits a positive temperature coefficient. The coercivity reaches a maximum of 2.5 T at 267 °C. The positive temperature coefficient of coercivity can be explained by the temperature dependence of the magnetocrystalline anisotropy field. It should be noted that MnBi compound is sensitive to oxygen and temperature. Cui *et al.* found that oxygen is the driving force for MnBi decomposition when subjected to a temperature higher than 200 °C. Once decomposed, the Mn reacts with oxygen forming MnO, causing irreversible loss of magnetic properties.<sup>[191]</sup> The authors also reported an energy product of 11.9 MGOe for the MnBi magnet, although it is prepared by ball milling, not melt spinning. To improve the room temperature coercivity, Kharel *et al.* studied the effect of Pr substitution and found that the coercivity increases by a factor of 9 from 0.26 for Pr-free to 2.3 T for 9 at.% Pr substitution.<sup>[192]</sup>

Recently, the Co-rich transition-metal alloys such as HfCo<sub>7</sub> and Zr<sub>2</sub>Co<sub>11</sub> have attracted interests to develop new RE-free magnetic materials with high-energy products. The metastable nature and/or the requirement of high formation temperature of about 1050–1230 °C for HfCo<sub>7</sub> phase indicate that melt spinning process is suitable to make such alloy with good phase purity. Although Zr<sub>2</sub>Co<sub>11</sub> phase has a wider temperature range of about 300–1254 °C, a high-temperature growth or annealing process followed by melt spinning was generally used to obtain high-anisotropy crystal structures in the alloys. Balasubramanian *et al.* fabricated the nanocrystalline Co<sub>100-x</sub>TM<sub>x</sub> alloys (TM = Zr, Hf, and 10 ≤ *x* ≤ 18) by melt spinning with varied wheel speed from 25 to 70 m/s.<sup>[193]</sup> For the Zr–Co alloys, the grain size of the melt-spun ribbons is reduced from 120 to 50 nm with increasing wheel speed from 45 to 70 m/s. The ribbons majorly consist of both rhombohedral and orthorhombic Zr<sub>2</sub>Co<sub>11</sub>, with the minor cubic Zr<sub>6</sub>Co<sub>23</sub> and Co phases. Although there are both magnetically hard and soft phases in the ribbons, the hysteresis loop of the 70 m/s melt-spun ribbon exhibits nearly a single-phase behavior and shows a coercivity of 0.24 T and an energy product of 4.3 MGOe. These properties have been slightly improved to 0.30 T and 4.6 MGOe by the same research group for coercivity and energy product, respectively.<sup>[194]</sup> For the Hf–Co alloys, an energy product of 5.2 MGOe was achieved in the HfCo<sub>7</sub> ribbons. Besides the HfCo<sub>7</sub> phase, McGuire *et al.* re-

ported a Hf<sub>2</sub>Co<sub>11</sub>B-type nanocrystalline by melt spinning with the best magnetic properties of  $\mu_0 M_r = 0.62$  T,  $\mu_0 H_c = 0.45$  T, and  $(BH)_{\max} = 6.7$  MGOe.<sup>[195]</sup>

Several RE-free magnets have L1<sub>0</sub>-type structure, such as Fe–Pt and Mn–Al. Zhang *et al.* studied the phase evolution, thermal stability and magnetic properties of the melt-spun Fe<sub>70-x</sub>Pt<sub>x</sub>B<sub>30</sub> ribbons.<sup>[196]</sup> It was found that the amorphous forming ability increases with small amount addition of Pt into the Fe<sub>70</sub>B<sub>30</sub> alloy and a complete amorphous phase is obtained in the alloys with *x* = 5 and 10 and wheel speed of 33 m/s. However, further increase of Pt content results in the formation of *fcc*-FePt, Fe<sub>2</sub>B with or without L1<sub>0</sub>-FePt phases. A homogenous microstructure, consisting of magnetically hard L1<sub>0</sub>-FePt and soft Fe<sub>2</sub>B phases with an average grain size of 30–50 nm, is formed in the ribbons with *x* = 10–20 after appropriate annealing. The coercivity of Fe<sub>70-x</sub>Pt<sub>x</sub>B<sub>30</sub> ribbons increases while remanence decreases with increasing Pt content. Good magnetic properties were obtained in the Fe<sub>70-x</sub>Pt<sub>x</sub>B<sub>30</sub> ribbons with  $\mu_0 M_r = 0.81$ –1.20 T,  $\mu_0 H_c = 0.22$ –0.65 T, and  $(BH)_{\max} = 8.0$ –11.0 MGOe.

Liu *et al.* studied the effects of C, B, and RE doping in phase transitions and magnetic properties of Mn–Al alloy.<sup>[197]</sup> The as-spun Mn–Al, Mn–Al–C, and Mn–Al–C–RE ribbons possessed a hexagonal  $\epsilon$  phase. The  $\epsilon$  to L1<sub>0</sub> phase transition occurs at ~ 500 °C, which is of interest as it could develop hard magnetic properties in the ribbons. Moderate carbon addition promotes the formation of the desired magnetically hard L1<sub>0</sub> phase and improves the hard magnetic properties. The best magnetic properties,  $\mu_0 M_r = 0.3$  T,  $\mu_0 H_c = 0.15$  T, and  $(BH)_{\max} = 1.5$  MGOe, were obtained in Mn–Al–C ribbon with C content of 1.7 at.% annealed at 650 °C, though they are quite low compared to other permanent magnets.

Löwe *et al.* studied the magnetic properties of melt-spun Alnico ribbons.<sup>[198]</sup> The grain size of the ribbons decreases from 5–10  $\mu\text{m}$  to about 1  $\mu\text{m}$  by increasing the wheel speed from 5 m/s to 60 m/s, and further decreases by addition of 1 at.% B to less than 1  $\mu\text{m}$ . The size of the spinodal features was about the same in the ribbons without B, which means that grain size above a certain threshold does not influence the spinodal decomposition anymore. The coercivities obtained in all samples are about 0.04 T, only half of those in anisotropic bulk samples, even though the aspect ratio of spinodals is the same as in bulk.

### 3.2. Nanocomposite magnets

Advanced permanent magnet applications always require materials with high remanence, high coercivity, and high Curie temperature. Although most single-phase permanent magnets have large coercivity, their saturation magnetization is relatively low compared to that of magnetically soft materials such as Fe or Fe–Co. In addition, the rare-earth magnets

are chemically reactive and expensive on account of a substantial content of rare-earth elements. It is natural to think that the combination of magnetically hard and soft materials should give higher magnetization and thus a potentially higher energy product with lower material cost. Coehoorn *et al.*<sup>[199–201]</sup> and Shen *et al.*<sup>[32,202–204]</sup> first reported the pioneering researches on the  $\text{Nd}_2\text{Fe}_{14}\text{B}/\text{Fe}_3\text{B}$  composites with  $\text{Fe}_3\text{B}$  as the magnetically soft phase and with the microstructure in nanoscale. The nanocomposites with the magnetically hard and soft phases have attracted tremendous attention in searching for novel permanent magnets, especially after the concept of exchange-spring magnets was first introduced by Kneller and Hawig in 1991.<sup>[13]</sup> In such exchange-spring magnets, the magnetically hard phase provides a high coercivity and the magnetically soft phase provides high magnetization. If the two phases are magnetically coupled together in an efficient way, the resultant composites can have both high coercivity and high magnetization, which eventually give a higher maximum energy product than the single-phase hard magnets. The concept was further developed by Skomski and Coey<sup>[14]</sup> who showed that the length scale of the soft phase should be smaller than twice of the domain wall width ( $\delta_B$ ) of the magnetically hard phase. For example,  $\delta_B$  of  $\text{Nd}_2\text{Fe}_{14}\text{B}$  is about 4.2 nm which leads to a critical size smaller than 10 nm for the magnetically soft phase. The magnetically soft phase becomes a slave to the magnetically hard phase and follows its magnetization direction, as illustrated in Fig. 22. The exchange coupling interaction between the magnetically soft and hard components, is the key in determining the overall magnetic properties of the composite magnets. Based on the micromagnetic analysis model, Skomski and Coey pointed out the giant energy product of about 137 MGOe can be achieved with alignment of magnetically hard grains and controlled microstructure in the  $\text{Sm}_2\text{Fe}_{17}\text{N}_3/\text{Fe}_{65}\text{Co}_{35}$  system, which is more than twice of theoretical limit of  $\text{Nd}_2\text{Fe}_{14}\text{B}$  magnet.<sup>[14]</sup>

The magnetic properties of the exchange-coupled nanocomposite magnets depend sensitively on both the material parameters, such as the magnetocrystalline anisotropy and saturated magnetization, and the microstructure, such as the grain size, soft-phase content and soft phase distribution. In principal, the nanocomposite could be made of any magnetically hard phase discussed in Section 3.1, and any magnetically soft phase with high magnetization such as Fe, Fe-Co, Fe-N, etc. It is a general trend that a larger amount of magnetically soft phase leads to a higher magnetization at the expense of coercivity reduction. The proper control of the microstructure then leads to the optimum  $(\text{BH})_{\text{max}}$ . In the last decades, many nanocomposite magnets have been studied intensively, including  $\text{Nd}_2\text{Fe}_{14}\text{B}/\text{Fe}_3\text{B}$ ,  $\text{Nd}_2\text{Fe}_{14}\text{B}/\alpha\text{-Fe}(\text{Co})$ ,  $\text{Pr}_2\text{Fe}_{14}\text{B}/\alpha\text{-Fe}(\text{Co})$ ,  $\text{Nd}_2\text{Fe}_{14}\text{C}/\alpha\text{-Fe}(\text{Co})$ ,  $\text{Sm}_2\text{Fe}_{17}\text{N}_x/\alpha\text{-Fe}$ ,  $\text{Sm}_2\text{Fe}_{15}\text{M}_2\text{C}_x/\alpha\text{-Fe}$  ( $M = \text{Ga}, \text{Si}, \text{Al}$ ),  $\text{SmCo}_5/\alpha\text{-Fe}$ , and  $L1_0$

$\text{FePt}/\text{Fe}_3\text{Pt}$ . Significant progresses have been made on improving the magnetic properties of the nanocomposite magnets in the past years. It should be noted that we only summarized some representative nanocomposites prepared by melt spinning in this review.

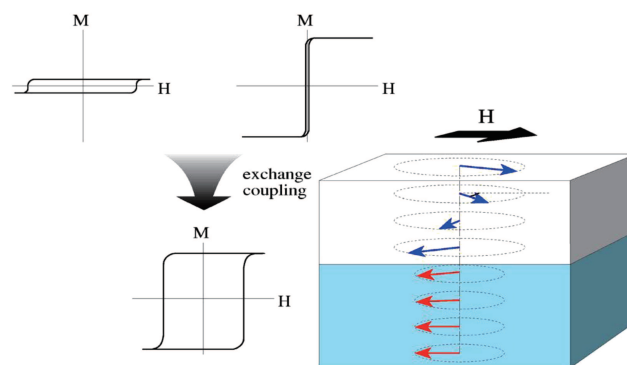


**Fig. 22.** (color online) Schematic of the exchange-spring principle from Ref. [205]. A magnetically hard phase possessing a wide hysteresis loop exchange couples to a magnetically soft phase possessing a tall hysteresis loop, forming a composite magnet that has both a wide and tall hysteresis loop. The image to the right illustrates a bilayer structure. If the soft layer thickness exceeds a critical size, the magnetization reversal happens first in the soft layer.

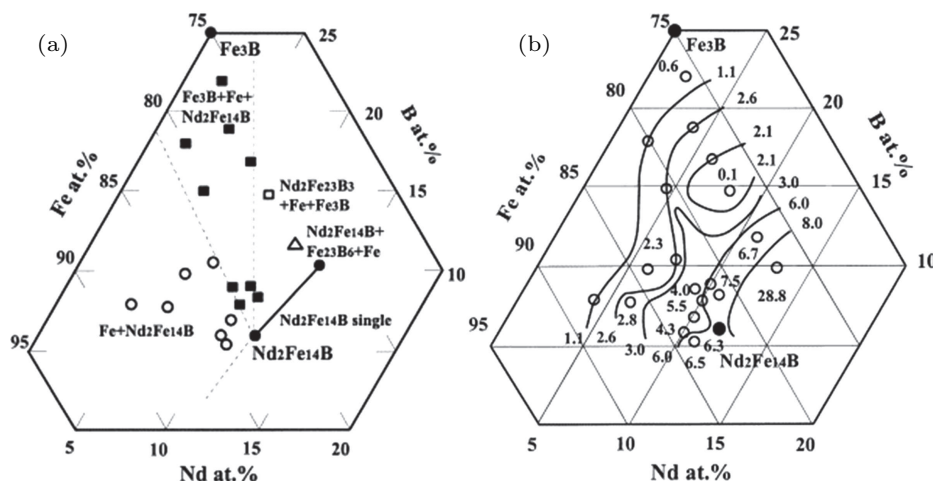
### 3.2.1. $\text{Nd}_2\text{Fe}_{14}\text{B}/\text{Fe}_3\text{B}$

Coehoorn *et al.* first obtained this novel nanocomposite magnet consisting mainly of  $\text{Fe}_3\text{B}$  with  $\text{Nd}_2\text{Fe}_{14}\text{B}$  as a secondary phase.<sup>[199]</sup> The amorphous alloy with composition of  $\text{Nd}_4\text{Fe}_{78}\text{B}_{18}$  was produced by melt spinning, followed by post annealing at 670 °C for 30 minutes. The annealing process consists of two steps: the metastable phase  $\text{Fe}_3\text{B}$  is crystallized with a small amount of  $\alpha\text{-Fe}$  phase at a lower temperature at first, while the hard-magnetic phase  $\text{Nd}_2\text{Fe}_{14}\text{B}$  is formed at a higher temperature. The annealed ribbons consist of 73%  $\text{Fe}_3\text{B}$ , 12%  $\alpha\text{-Fe}$ , and only 15% magnetically hard phase  $\text{Nd}_2\text{Fe}_{14}\text{B}$ . The saturated magnetization of  $\text{Fe}_3\text{B}$  and  $\text{Nd}_2\text{Fe}_{14}\text{B}$  are both 1.6 T at room temperature, while  $\text{Fe}_3\text{B}$  has a higher Curie temperature of about 513 °C, nearly 200 °C higher than that of  $\text{Nd}_2\text{Fe}_{14}\text{B}$ . The annealed ribbon gives a coercivity of 0.3 T, which may be due to the presence of  $\text{Nd}_2\text{Fe}_{14}\text{B}$  since  $\text{Fe}_3\text{B}$  has much lower magnetocrystalline anisotropy. The most remarkable property in this material is the normalized remanence, which is as high as 0.75 and much higher than 0.5 predicted by Stoner–Wohlfarth model. The large remanence enhancement is attributed to the fine microstructure with  $\text{Fe}_3\text{B}$  grains of 30 nm and  $\text{Nd}_2\text{Fe}_{14}\text{B}$  grains of 10 nm plus the exchange coupling between them. Owing to the large remanence, the energy product of 11.9 MGOe is obtained.<sup>[200]</sup> With partial substitution of Nd by Tb or Dy, the coercivity of the melt-spun ribbons can be improved to 0.45 T.<sup>[201]</sup> Simultaneously, Shen *et al.* studied the amorphization and crystallization of the rapidly quenched  $M_{1-x}(\text{Nd}_2\text{Fe}_{14}\text{B})_x$  ribbons ( $M = \text{Fe}_3\text{B}, \text{Fe}_2\text{B}$ ;  $0 \leq$

$x \leq 1.0$ ).<sup>[203]</sup> By the analyses of phase components and magnetic properties, it was found that the  $\text{Fe}_3\text{B}$ -based materials have superior properties than the  $\text{Fe}_2\text{B}$ -based materials. A coercivity of 0.3 T and an energy product of 13 MGOe in  $\text{Nd}_4\text{Fe}_{77.5}\text{B}_{18.5}$  alloys are achieved at room temperature by annealing at 670 °C for a short time.

Kim *et al.* studied the ferromagnetic phase diagram of the  $\text{Nd}_x\text{Fe}_y\text{B}_z$  ( $2 \leq x \leq 13$ ,  $76 \leq y \leq 88$ ,  $5.5 \leq z \leq 22$ ) melt-spun alloys.<sup>[206]</sup> Most of the as-spun ribbons prepared at 35 m/s are found to contain amorphous phase. Depending on the composition, the main phases of the optimally annealed ribbons are found to possess one or more the following phase:  $\alpha$ -Fe,  $\text{Fe}_3\text{B}$ ,  $\text{Nd}_2\text{Fe}_{23}\text{B}_3$ , and  $\text{Nd}_2\text{Fe}_{14}\text{B}$  phases. It was found that the  $\text{Fe}_3\text{B}$  phase precipitates only appears in the alloys with high boron content and low Nd content. Figure 23(a) summarizes the ferromagnetic phase diagram of the optimally an-

nealed  $\text{Nd}_x\text{Fe}_y\text{B}_z$  melt-spun alloys: (i) for Nd-rich alloys with  $x \geq 12$ ,  $\text{Nd}_2\text{Fe}_{14}\text{B}$  appears to be the main phase; (ii) for Fe-rich alloys with  $y \geq 83$  and  $x \leq 11$ , the major phase is  $\alpha$ -Fe with  $\text{Nd}_2\text{Fe}_{14}\text{B}$  as a secondary phase; (iii) for B-rich alloys with  $x \leq 11$ ,  $76 \leq y \leq 82$ , and  $7 \leq z \leq 22$ , the major phase is  $\text{Fe}_3\text{B}$  with  $\alpha$ -Fe and  $\text{Nd}_2\text{Fe}_{14}\text{B}$  as minor phases; (iv) for the  $\text{Nd}_8\text{Fe}_{77}\text{B}_{15}$  alloy, the major phase is  $\text{Nd}_2\text{Fe}_{23}\text{B}_3$  with minor phases of  $\text{Fe}_3\text{B}$  and  $\alpha$ -Fe, showing no evidence of the presence of  $\text{Nd}_2\text{Fe}_{14}\text{B}$ ; (v) for the  $\text{Nd}_{11}\text{Fe}_{77}\text{B}_{12}$  alloy, the major phase is  $\text{Nd}_2\text{Fe}_{14}\text{B}$  with precipitation of  $\text{Fe}_{23}\text{B}_6$  and  $\alpha$ -Fe. The coercivity of alloys with different phase components has a wide distribution, strongly depending on the Nd content, as shown in Fig. 23(b). A high coercivity of about 2.9 T was observed in the  $\text{Nd}_{13}\text{Fe}_{77}\text{B}_{10}$  alloy, while it dramatically dropped to 0.01 T due to the formation of magnetically soft phase  $\text{Nd}_2\text{Fe}_{23}\text{B}_3$  instead of  $\text{Nd}_2\text{Fe}_{14}\text{B}$  phase in the  $\text{Nd}_8\text{Fe}_{77}\text{B}_{15}$  alloy.



Shen *et al.* studied the Co substitution for Fe in the  $\text{Nd}_4(\text{Fe}_{1-x}\text{Co}_x)_{77.5}\text{B}_{18.5}$  alloys and found that the Curie temperatures of both the as-quenched amorphous and annealed ribbons increase with Co content.<sup>[204]</sup> Interestingly, it was observed that the magnetic moment of Fe atom increases with increasing Co content from  $x = 0$  to  $x = 0.4$ , while the magnetic moment of Co atom keeps a constant value over the whole concentration range. Unfortunately, the coercivity decreases monotonically with increase of Co concentration. A still good magnetic property was observed in the ribbons with  $x \leq 0.2$ , which have coercivity of 0.23–0.30 T and energy products of 11.6–13.5 MGOe. The benefits of Co addition on the magnetic properties of the  $\text{Fe}_3\text{B}$ -based nanocomposite were confirmed in  $\text{Nd}_4\text{Fe}_{77.5-x}\text{Co}_x(\text{HfGa})_y\text{B}_{18.5}$  ( $0 \leq x \leq 5$ ,  $y = 0, 0.5$ ) ribbons.<sup>[210]</sup> The Co addition retarded the crystallization of both  $\alpha$ -Fe and  $\text{Fe}_3\text{B}$  phases, but accelerated that of  $\text{Nd}_2\text{Fe}_{14}\text{B}$  phase. As a result, the coercivity increased slightly with the addition of Co and an energy product of about 14.4 MGOe was obtained.

Kanekiyo *et al.* have reported that Al, Si, Cu, Ga, Ag, Au additives considerably reduce grain size of  $(\text{Fe},\text{Co})_3\text{B}/\text{Nd}_2\text{Fe}_{14}\text{B}$  nanocomposite based on  $\text{Nd}_5\text{Fe}_{71.5}\text{Co}_5\text{B}_{18.5}M$  alloy, where  $M$  is the above-mentioned elements.<sup>[211]</sup> For example, the optimally heat-treated ribbons of  $\text{Nd}_5\text{Fe}_{76.5}\text{B}_{18.5}$  have grains around 40–50 nm, while the Ga or Al combined with Co addition could reduce the grain size down to 10–20 nm in the  $\text{Nd}_5\text{Fe}_{71.5}\text{Co}_5\text{B}_{18.5}M$  ribbon. The grain refinement increases the remanence from 1.0 T for  $\text{Nd}_5\text{Fe}_{76.5}\text{B}_{18.5}$  ribbon to 1.08–1.20 T for the  $\text{Nd}_5\text{Fe}_{71.5}\text{Co}_5\text{B}_{18.5}M$  ribbons, where Si additive gives the highest value. The Cu additive provides the lowest remanence among the  $M$ -added samples, but it generates the largest coercivity around 0.45 T. On the other hand, Ga-added ribbons have the largest energy product of about 16 MGOe. Ping *et al.* found that Cu and Nb can refine the microstructure of the  $\text{Fe}_3\text{B}/\text{Nd}_2\text{Fe}_{14}\text{B}$  using TEM and atom probe field ion microscopy (APFIM).<sup>[212]</sup> Figure 24 shows the TEM micrographs of alloys with and without Cu and Nb additions. This indicates that Cu addition to the ternary alloy causes significant reduction of the grain size of the

optimum nanocomposite microstructure. The combination of Cu and Nb can reduce the grain size down to 12 nm, where Cu is dissolved in the  $\text{Nd}_2\text{Fe}_{14}\text{B}$  phase. However, Nb mainly exists in the  $\text{Fe}_{23}\text{B}_6$  phase. The crystallization process in  $\text{Nd}_{4.5}\text{Fe}_{75.8}\text{B}_{18.5}\text{Cu}_{0.2}\text{Nb}_1$  ribbons are: amorphous  $\rightarrow \text{Fe}_3\text{B} + \text{amorphous} \rightarrow \text{Fe}_3\text{B} + \text{Nd}_2\text{Fe}_{14}\text{B} + \text{Fe}_{23}\text{B}_6$ . An even higher remanence about 1.25 T is obtained in these ribbons with an energy product of about 15.6 MGOe. Rajasekhar *et al.* studied the Mn substitution of Fe in the  $\text{Nd}_{4.5}\text{Fe}_{77-x}\text{Mn}_x\text{B}_{18.5}$  ( $x = 0-2$ ) nanocomposite magnets and found that 1 at.% Mn addition could improve both coercivity and the normalized remanence.<sup>[213]</sup>

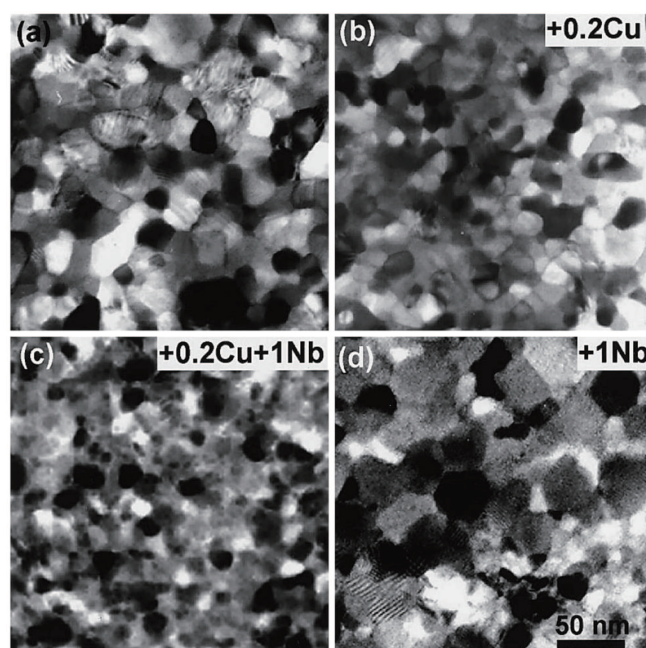


**Fig. 24.** TEM bright field micrographs of (a)  $\text{Nd}_{4.5}\text{Fe}_{77}\text{B}_{18.5}$ , (b)  $\text{Nd}_{4.5}\text{Fe}_{76.8}\text{B}_{18.5}\text{Cu}_{0.2}$ , (c)  $\text{Nd}_{4.5}\text{Fe}_{75.8}\text{B}_{18.5}\text{Cu}_{0.2}\text{Nb}_1$ , and (d)  $\text{Nd}_{4.5}\text{Fe}_{76}\text{B}_{18.5}\text{Nb}_1$  alloys annealed at 660 °C for 10 min. The average grain size is about 30, 17, 12, and 43 nm, respectively.<sup>[212]</sup>

Cheng *et al.* reported that the carbon substitution for B reduces the crystallization temperature of the as-spun  $\text{Nd}_4\text{Fe}_{77.5}\text{B}_{18.5}$  amorphous alloy.<sup>[214]</sup> Unfortunately, the coercivity of the crystallized ribbons decreases with increasing carbon content, with a simultaneous development of an orthorhombic  $\text{Fe}_3\text{B}$  (o- $\text{Fe}_3\text{B}$ ) phase, instead of the bct- $\text{Fe}_3\text{B}$  phase.

**Table 8.**  $\mu_0M_r$ ,  $\mu_0H_c$ , and  $(\text{BH})_{\text{max}}$  of  $\text{Fe}_3\text{B}/\text{Nd}_2\text{Fe}_{14}\text{B}$  nanocomposite magnets with different compositions.

Composition	$\mu_0M_r/\text{T}$	$\mu_0H_c/\text{T}$	$(\text{BH})_{\text{max}}/\text{MGOe}$	Reference
$\text{Nd}_4\text{Fe}_{78}\text{B}_{18}$	1.20	0.40	11.9	[200]
$\text{Nd}_4\text{Fe}_{77.5}\text{B}_{18.5}$	1.20	0.30	13.0	[203]
$\text{Nd}_4(\text{Fe}_{0.94}\text{Co}_{0.06})_{77.5}\text{B}_{18.5}$	1.20	0.3	13.5	[204]
$\text{Nd}_4\text{Fe}_{77.5-x}\text{Co}_x\text{Hf}_{0.5}\text{Ga}_{0.5}\text{B}_{18.5}$	1.15	0.35	14.4	[210]
$\text{Nd}_{4.5}\text{Fe}_{73}\text{Co}_3\text{Ga}_1\text{B}_{18.5}$	1.20	0.42	16.0	[211]
$\text{Nd}_{3.5}\text{Dy}_1\text{Fe}_{73}\text{Co}_3\text{Ga}_1\text{B}_{18.5}$	1.15	0.50	16.5	[208]
$\text{Nd}_{4.5}\text{Fe}_{75.8}\text{B}_{18.5}\text{Cu}_{0.2}\text{Nb}_1$	1.25	0.34	15.6	[212]
$\text{Nd}_{4.5}\text{Fe}_{75.8}\text{B}_{18.5}\text{Cu}_{0.2}\text{Nb}_1$	1.25	0.34	15.6	[212]

Although researches still occasionally occur recently, it is concluded that the energy product of  $\text{Fe}_3\text{B}/\text{Nd}_2\text{Fe}_{14}\text{B}$  nanocomposite magnets is relatively low due to the relatively low saturated magnetization of  $\text{Fe}_3\text{B}$  phase. Their coercivity is relative low comparing to other nanocomposites, so it is not critical to understand where is the coercivity from, either the bct- $\text{Fe}_3\text{B}$  phase or  $\text{Nd}_2\text{Fe}_{14}\text{B}$  phase. The magnetic properties of some typical  $\text{Fe}_3\text{B}/\text{Nd}_2\text{Fe}_{14}\text{B}$  nanocomposite magnets prepared by melt spinning are summarized in Table 8.

### 3.2.2. $\text{Nd}_2\text{Fe}_{14}\text{B}/\alpha\text{-Fe}$

The  $\alpha\text{-Fe}$  phase is actually often observed in the  $\text{Fe}_3\text{B}/\text{Nd}_2\text{Fe}_{14}\text{B}$  nanocomposite as mentioned in Section 3.2.1. Since  $\alpha\text{-Fe}$  has a higher saturated magnetization (about 2.2 T) than those of  $\text{Fe}_3\text{B}$  and  $\text{Nd}_2\text{Fe}_{14}\text{B}$  phases (both about 1.6 T), it is expected that  $\text{Nd}_2\text{Fe}_{14}\text{B}/\alpha\text{-Fe}$  magnets have higher remanence and thus higher energy product than those of  $\text{Nd}_2\text{Fe}_{14}\text{B}/\text{Fe}_3\text{B}$  magnets. Moreover,  $\text{Nd}_2\text{Fe}_{14}\text{B}/\alpha\text{-Fe}$  magnets also have higher coercivity than  $\text{Nd}_2\text{Fe}_{14}\text{B}/\text{Fe}_3\text{B}$ . Therefore,  $\text{Nd}_2\text{Fe}_{14}\text{B}/\alpha\text{-Fe}$  magnet is superior to  $\text{Nd}_2\text{Fe}_{14}\text{B}/\text{Fe}_3\text{B}$  for hard magnetic applications. It is true that most of investigations on exchange-coupled nanocomposites are based on  $\text{Nd}_2\text{Fe}_{14}\text{B}/\alpha\text{-Fe}$  magnets recently. To form the nanocomposite magnet with  $\alpha\text{-Fe}$  as the magnetically soft phase instead of  $\text{Fe}_3\text{B}$ , the B content is usually controlled to be about or less than 10 at.%, which is much lower than 18–20 at.% of the  $\text{Nd}_2\text{Fe}_{14}\text{B}/\text{Fe}_3\text{B}$  magnets. However, the low B content causes one shortcoming, i.e., the difficult in controlling the microstructure of the  $\text{Nd}_2\text{Fe}_{14}\text{B}/\alpha\text{-Fe}$  because of the low glass forming ability in such alloys. Because of this, the production of  $\text{Nd}_2\text{Fe}_{14}\text{B}/\alpha\text{-Fe}$  nanocomposite materials in an industrial scale with good reproducibility is challenging. The elemental additives are usually used in the production in order to control the microstructure, which is a major topic of this type of magnets.

The microstructure control, such as grain size, is one of the key factors to achieve high remanence and coercivity in the nanocrystalline and nanocomposite magnets. Davies *et al.* studied the effects of grain size on the remanence and coercivity of the single-phase nanocrystalline  $\text{Nd}_{13.2}\text{Fe}_{79.6}\text{B}_6\text{Si}_{1.2}$  magnets.<sup>[215]</sup> It is observed that remanence enhancement begins when grain size falls below  $\sim 30$  nm for both surfaces of the melt-spun ribbons, i.e., roller and free surfaces. The phenomenon is believed to result from exchange coupling between grains when they are free of non-magnetic intergranular phase. This condition correspondingly leads to reduction of coercivity since it lowers the resistance to reverse magnetization, as shown in Fig. 25(a). Based on the controlled grain growth, Davis *et al.* first reported the formation of  $\text{Nd}_2\text{Fe}_{14}\text{B}/\alpha\text{-Fe}$  nanocomposites from the  $\text{Nd}_{8+x}\text{Fe}_{86-x}\text{B}_6$  alloys by varying the alloy composition and processing conditions of the melt spinning.<sup>[215]</sup> It is found that the remanence

is consistently above 0.8 T even for the stoichiometric composition  $\text{Nd}_{12}\text{Fe}_{82}\text{B}_6$  and increases monotonously to  $> 1.1$  T for  $\text{Nd}_8\text{Fe}_{86}\text{B}_6$  with decreasing Nd content. The two-phase structure forms in the alloys of Nd content less than 11 at% and  $\text{Nd}_2\text{Fe}_{14}\text{B}$  grains smaller than 30 nm interspersed with smaller isolated  $\alpha\text{-Fe}$  grains typically  $\sim 10$  nm. Thus, the high remanence for these alloys is believed to arise from a combination of the remanence enhancement observed in single-phase  $\text{Nd}_2\text{Fe}_{14}\text{B}$  nanocrystalline and an increase in saturated magnetization due to the presence of  $\alpha\text{-Fe}$ , whose volume fraction increases with decreasing Nd content. As remanence increases, the coercivity decreases. However, it should be noted that this decrease is only gradual instead of collapse because of the exchange coupling between the magnetically hard and soft phases. Therefore, high energy products around 20 MGOe with coercivity of about 0.6 T are obtained for the isotropic nanocrystalline ribbons with Nd less than 9.5 at%. The dependences of remanence, coercivity and energy product on Nd content are given in Fig. 25(b). Similar results are also reported in the work from same research group.<sup>[216]</sup>

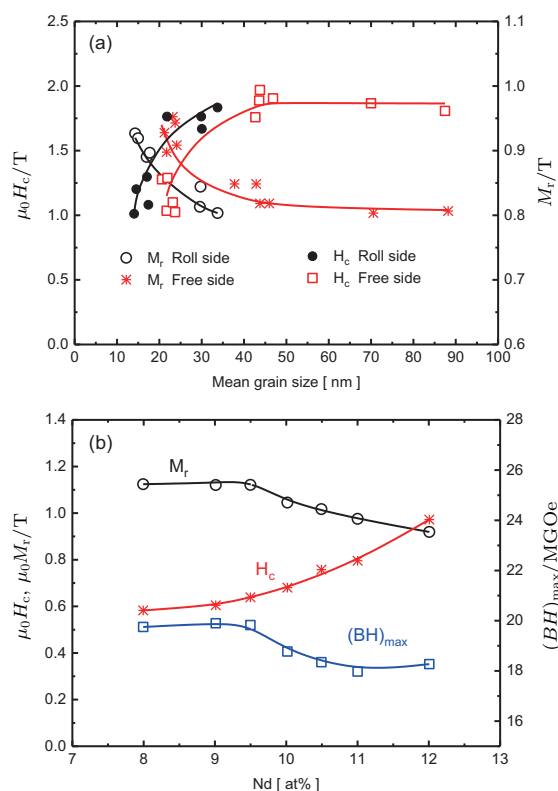


**Fig. 25.** (color online) (a) Dependence of remanence and coercivity on grain size of melt-spun  $\text{Nd}_{13.2}\text{Fe}_{79.6}\text{B}_6\text{Si}_{1.2}$  ribbons. (b) Dependence of magnetic properties on Nd content of melt-spun  $\text{Nd}_{8+x}\text{Fe}_{86-x}\text{B}_6$  ribbons. The figures are reproduced from Ref. [215].

Besides the grain size control, the soft-phase component is another key factor to achieve good magnetic properties in nanocomposite  $\text{Nd}_2\text{Fe}_{14}\text{B}/\alpha\text{-Fe}$  magnets. Bauer *et al.* studied the effect of  $\alpha\text{-Fe}$  phase content (up to 40 vol.%) on magnetic properties of the composite magnets, starting from

nearly single-phase  $\text{Nd}_2\text{Fe}_{14}\text{B}$  magnets.<sup>[73]</sup> The maximum remanence  $\mu_0 M_r = 1.25$  T with  $\mu_0 H_c = 0.53$  T and  $(\text{BH})_{\text{max}} = 23.2$  MGOe were achieved in nanocomposite magnets containing 30 vol.%  $\alpha$ -Fe (as shown in Fig. 26). It should be noted that demagnetization factor  $N$  of the ribbons, which is on the order of 0.01, was calculated based on the dimensions of the flakes. A representative TEM micrograph of a nanocomposite  $\text{Nd}_{10}\text{Fe}_{84}\text{B}_6$  magnet with 14.2 vol%  $\alpha$ -Fe is given in Fig. 27. The microstructure analysis reveals two characteristic maxima in the grain distribution at about 15 nm and 25 nm corresponding to the  $\alpha$ -Fe phase and to the  $\text{Nd}_2\text{Fe}_{14}\text{B}$  phase, respectively. Further high-resolution TEM analysis confirmed that smaller and larger grains represent the  $\alpha$ -Fe and  $\text{Nd}_2\text{Fe}_{14}\text{B}$  phases, respectively.

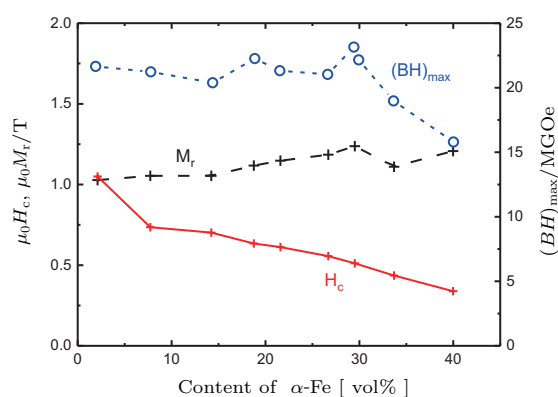


**Fig. 26.** (color online) Dependence of magnetic properties of NdFeB-based nanocomposite magnets on  $\alpha$ -Fe content at room temperature. The figure is reproduced from Ref. [73].

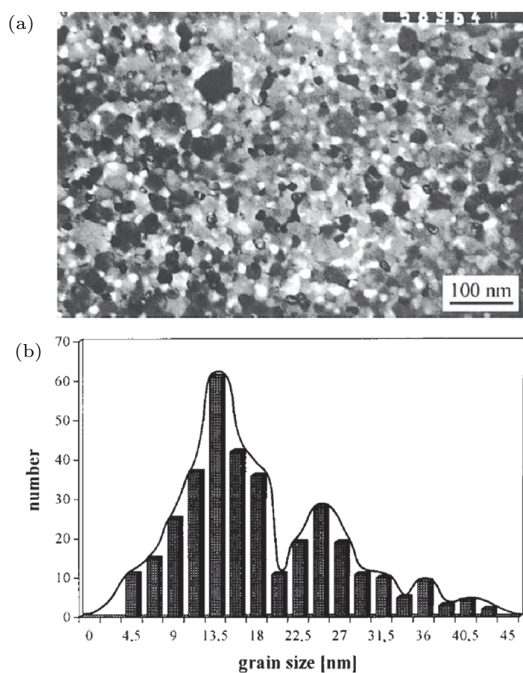


**Fig. 27.** (a) TEM micrograph and (b) grain size distribution of melt-spun  $\text{Nd}_{10}\text{Fe}_{84}\text{B}_6$  ribbon with 14.2 vol.%  $\alpha$ -Fe.<sup>[73]</sup>

The element substitutions in the  $\text{Nd}_2\text{Fe}_{14}\text{B}/\alpha$ -Fe affect the microstructure and thus magnetic properties, which are

categorized into *RE* substitution, refractory element substitution and other element substitution, as summarized below. The magnetic properties of the element substituted melt-spun ribbons are also summarized in Table 9.

**RE substitution.** Betancourt *et al.* studied the Nd:Pr ratio on the magnetic properties of  $(\text{NdPr})_x\text{Fe}_{94-x}\text{B}_6$  ribbons.<sup>[217]</sup> Remanence enhancement was observed for all compositions studied, arising from intergrain exchange coupling between the  $(\text{NdPr})_2\text{Fe}_{14}\text{B}$  crystallites with an average grain size of  $\sim 40$  nm and  $\alpha$ -Fe grains. An excellent combination of  $(\text{BH})_{\text{max}}$  about 23 MGOe and coercivity about 1.0 T was observed for the  $(\text{Pr}_{0.75}\text{Nd}_{0.25})_2\text{Fe}_{14}\text{B}$  alloy. Zhang *et al.* reported a similar enhancement of magnetic properties through Pr substitution for Nd in the  $(\text{Nd}_{1-x}\text{Pr}_x)_9\text{Fe}_{86}\text{B}_5$  ribbons.<sup>[218]</sup> The best magnetic properties with remanence of 1.14 T, coercivity of 0.62 T, and energy product of 19 MGOe are achieved in the sample with  $x = 0.6$ . Wang *et al.* reported that 1 at.% Dy substitution for Nd could improve coercivity of  $\text{Nd}_2\text{Fe}_{14}\text{B}/\alpha$ -Fe nanocomposite magnets, which is understandable because  $\text{Dy}_2\text{Fe}_{14}\text{B}$  has higher magnetocrystalline anisotropy than that of  $\text{Nd}_2\text{Fe}_{14}\text{B}$ .<sup>[219]</sup> With optimized composition and annealing conditions, the magnetic properties of remanence, coercivity, and energy product are 1.02 T, 0.88 T, and 16.8 MGOe in  $\text{Nd}_{8.16}\text{Dy}_1\text{Fe}_{85.26}\text{Nb}_1\text{B}_{4.58}$  alloy. Because it is believed that La is helpful to improve the glass forming ability due to its large atomic size and thus to reduce the optimum wheel speed required to prepare  $\text{Nd}_2\text{Fe}_{14}\text{B}/\alpha$ -Fe nanocomposites, Change *et al.* studied the effect of La substitution for Nd on the microstructure structure and magnetic properties of  $\text{Nd}_2\text{Fe}_{14}\text{B}/\alpha$ -Fe magnets.<sup>[220]</sup> Unfortunately, it was found that the grain size increases from 20–30 nm for both phases of the  $\text{Nd}_{9.5}\text{Fe}_{80.5}\text{B}_{10}$  ribbons to 70–80 and 30 nm of the  $(\text{Nd}_{0.95}\text{La}_{0.05})_{9.5}\text{Fe}_{78.5}\text{Cr}_2\text{B}_{10}$ , respectively. Interestingly, a further increase in total rare earth content to  $(\text{Nd}_{0.95}\text{La}_{0.05})_{11}\text{Fe}_{77}\text{Cr}_2\text{B}_{10}$  resulted in fine grains with average grain size around 20–30 nm again. A remanence of 0.92–0.97 T, coercivity of 1.11–1.32 T, and energy product of 16.5–18.0 were obtained in the La substitution ribbons.

**Refractory elements** The melting points of the refractory metals (Cr, Ti, Nb, V, Mo, Zr, Hf, Ta, Mn, and W) are the highest for all element except C, Os, and Ir. It was found that the refractory element substitution for Fe can effectively reduce the grain size of the  $\text{Nd}_2\text{Fe}_{14}\text{B}/\alpha$ -Fe nanocomposite as they are not easy to be dissolved in both  $\text{Nd}_2\text{Fe}_{14}\text{B}$  and  $\alpha$ -Fe phase. In other words, these elements usually stay at the grain boundaries and thus improve the coercivity of the magnets. The effect of Nb on the microstructure of  $\text{Nd}_2\text{Fe}_{14}\text{B}/\alpha$ -Fe nanocomposites has been widely studied and it has been approved as

one of the effective elements to improve the magnetic properties. Chang *et al.* have confirmed that Nb is the best element among Ti, Nb, V, Cr, and Mo to improve the coercivity of  $\text{Nd}_{10}\text{Fe}_{\text{bal}}\text{MCB}_{10.5}$  ribbons.<sup>[221]</sup> The Nb-substituted ribbons have a coercivity of 1.5 T, which is much larger than the second best of Ti-substituted ribbons with a coercivity of 1.2 T. The coercivity enhancement through Nb-substitution is again confirmed by Chen *et al.* in the  $\text{Nd}_{12}\text{Fe}_{82-x}\text{Nb}_x\text{B}_6$  ( $x = 0, 1.5, \text{ and } 3$ ) ribbons.<sup>[222]</sup> A coercivity of 1.24 T in ribbons with 1.5 at.% Nb is much larger than that of Nb-free ribbons with a coercivity of 0.86 T. In addition, the thermal stability is significantly improved with Nb substitution. As compared with the ternary  $\text{Nd}_{12}\text{Fe}_{82}\text{B}_6$ , the temperature coefficient of coercivity is reduced from  $-0.36\%/^{\circ}\text{C}$  to  $-0.32\%/^{\circ}\text{C}$ . TEM and energy dispersive spectroscopy (EDS) analyses show that Nb atoms are expelled during melt-spinning and annealing processes, resulting in the enrichment of Nb atoms in the grain boundary region and the generation of Nb-rich phase along grain boundary, which inhibits the grain growth and finally refines the microstructure. The enrichment of Nb atoms at the grain boundary may weaken the exchange coupling between the phases in the above magnets, which causes a higher coercivity but lower remanence. As a result, the Nb-substituted nanocomposite magnets do not have best energy products. Recently, Zhang *et al.* reported that enhanced remanence and energy product could be achieved in Nb-substituted magnets if the microstructure are fine controlled in the melt-spun ribbons.<sup>[223]</sup> Figure 28 compares the TEM images of the  $\text{Nd}_{12}\text{Fe}_{82}\text{B}_6$  and  $\text{Nd}_{10}\text{Nb}_2\text{Fe}_{82}\text{B}_6$  ribbons spun at 15 m/s. The grain size decreases from 120 nm for  $\text{Nd}_{12}\text{Fe}_{82}\text{B}_6$  to 20 nm for  $\text{Nd}_{10}\text{Nb}_2\text{Fe}_{82}\text{B}_6$ . The grain refinement promotes intergrain exchange coupling and leads to the remanence enhancement from 0.84 T to 0.99 T and energy products increase from 15 MGOe to 20 MGOe. It should be noted that Ti substitution has similar function as Nb. Chang *et al.* reported that Ti substitution in the  $\text{Nd}_2\text{Fe}_{14}\text{B}/\alpha\text{-Fe}$  nanocomposite ribbons could result in an even finer grain structure than that of Nb substitution, i.e., average grain size of about 10–20 nm is achievable.<sup>[221]</sup> Therefore, a higher energy product is achieved in the Ti-substitution nanocomposites, although it accompanies a slightly lower coercivity. Zhang *et al.* investigated the effect of Ti content on magnetic properties of  $\text{Nd}_9\text{Dy}_{0.4}\text{Fe}_{81.24-x}\text{Ti}_x\text{Nb}_{0.36}\text{Co}_3\text{B}_6$  ribbons and found that the coercivity and energy product increases from 0.74 T and 15.8 MGOe to 1.20 T and 21.9 MGOe, respectively.<sup>[224]</sup> Besides Nb and Ti, Ta is another element proved to be an effective element to improve microstructure and magnetic properties of the nanocomposite magnets. Zeng *et al.* found that the average

grain size of 30–40 nm of Ta-free  $\text{Nd}_{9.5}\text{Fe}_{84}\text{B}_{6.5}$  ribbons can be reduced to 20–25 nm with 1.5 at.% Ta substitution.<sup>[225]</sup> Although the remanence is reduced from 1.07 T to 0.94, the coercivity increases from 0.64 T to 0.94 T. The refined microstructure improves the intergrain exchange coupling and leads to an energy product about 19.8 MGOe. Hashino *et al.* have found that Zr addition improves the glass forming ability and retards the formation of  $\alpha\text{-Fe}$  phase in the  $\text{Nd}_{10}\text{Fe}_{83-x}\text{Zr}_x\text{B}_6\text{C}_1$  ribbons, which results in a finer microstructure in the melt-spun ribbons.<sup>[226]</sup> Wang *et al.* confirmed that a small amount of Zr addition can inhibit the prior precipitation of the magnetically soft  $\alpha\text{-Fe}$  phase and refine the microstructure.<sup>[36]</sup> A combination of Zr and Nb could further improve the maximum energy product.

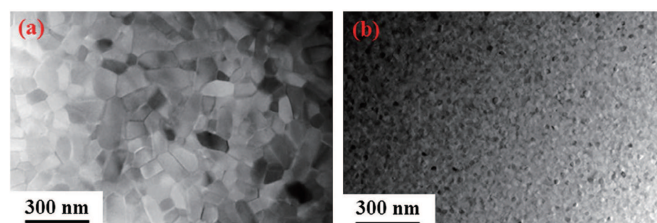
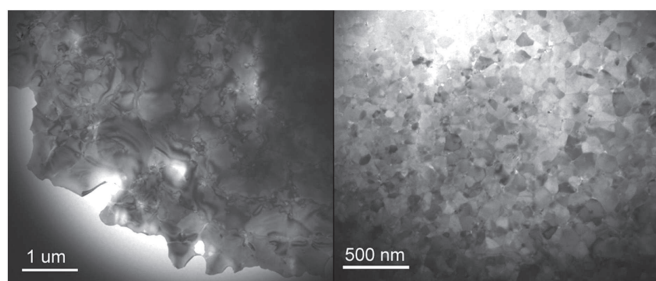


Fig. 28. TEM images for the (a)  $\text{Nd}_{12}\text{Fe}_{82}\text{B}_6$  and (b)  $\text{Nd}_{10}\text{Nb}_2\text{Fe}_{82}\text{B}_6$  ribbons spun at 15 m/s.<sup>[223]</sup>

**Other element substitutions** Liu and Davis studied the substitution of Fe by Co and found that Co improves remanence, coercivity, and Curie temperature in certain concentration range. The 10–20 at.% Co substitution could lead to the best magnetic properties with  $\mu_0M_r = 0.97$  T and  $\mu_0H_c = 0.55$  T in the nanocomposite  $\text{Nd}_2\text{Fe}_{14}\text{B}/\alpha\text{-Fe}$  alloys produced by melt spinning.<sup>[227]</sup> Ji *et al.* found that 1 at% indium (In) addition in the  $\text{Nd}_{10}\text{Fe}_{84-x}\text{B}_6\text{In}_x$  nanocomposites significantly enhances the hard magnetic properties.<sup>[228]</sup> The coercivity increases from 0.5 T to 0.6 T, while remanence ratio also increases from 0.71 to 0.83, accompanying improvement of squareness of hysteresis loop, indicating a strong inter-phase exchange coupling in the nanocomposite magnets. Therefore, the maximum magnetic energy product increases remarkably from 12 to 18 MGOe. The origin for these enhancements is mainly attributed to the magnetically softened grain boundaries and enhanced crystallographic coherency by indium addition. Ma *et al.* found Zn addition could help on developing texture in the hot-deformed  $(\text{NdDy})_{11.5}\text{Fe}_{82.5-x}\text{Nb}_x\text{B}_6$  magnets, because the combination of Nb and Zn promotes the volume fraction of the intergranular phase where Zn prefers to diffuse into.<sup>[229]</sup> The combination of Nb and Zn addition increases the coercivity of alloys up to 22% and a maximum energy product of 20.6 MGOe is obtained.

**Table 9.**  $\mu_0M_r$ ,  $\mu_0H_c$ , and  $(BH)_{\max}$  of  $\text{Nd}_2\text{Fe}_{14}\text{B}/\alpha\text{-Fe}$  nanocomposite magnets with different compositions and different element substitutions.

Composition	$\mu_0M_r/\text{T}$	$\mu_0H_c/\text{T}$	$(BH)_{\max}/\text{MGOe}$	Reference
$\text{Nd}_{9.5}\text{Fe}_{84.5}\text{B}_6$	1.10	0.6	20	[215]
$\text{Nd}_{12}\text{Fe}_{82}\text{B}_6$ (stoichiometric)	1.02	1.05	21.2	[73]
$\text{Nd}_8\text{Fe}_{87}\text{B}_5$	1.25	0.53	23.2	
$(\text{Pr}_{0.75}\text{Nd}_{0.25})_2\text{Fe}_{14}\text{B}$	1.05	1.01	23	[217]
$(\text{Nd}_{0.4}\text{Pr}_{0.6})_9\text{Fe}_{86}\text{B}_5$	1.14	0.62	19	[218]
$\text{Nd}_{8.16}\text{Dy}_1\text{Fe}_{85.26}\text{Nb}_1\text{B}_{4.58}$	1.02	0.88	16.8	[219]
$\text{Nd}_{10}\text{Fe}_{77.5}\text{TiCB}_{10.5}$	0.92	1.21	16.2	
$\text{Nd}_{10}\text{Fe}_{77.5}\text{NbCB}_{10.5}$	0.85	1.50	1.45	
$\text{Nd}_{10}\text{Fe}_{77.5}\text{VCB}_{10.5}$	0.87	1.04	14.3	[221]
$\text{Nd}_{10}\text{Fe}_{77.5}\text{CrCB}_{10.5}$	0.92	0.99	13.2	
$\text{Nd}_{10}\text{Fe}_{77.5}\text{MoCB}_{10.5}$	0.81	0.99	11.6	
$\text{Nd}_{10}\text{Nb}_2\text{Fe}_{82}\text{B}_6$	0.99	1.18	20	[223]
$\text{Nd}_9\text{Dy}_{0.4}\text{Fe}_{76.24}\text{Ti}_5\text{Nb}_{0.36}\text{Co}_3\text{B}_6$	0.91	1.20	21.9	[224]
$\text{Nd}_{9.5}\text{Fe}_{82.5}\text{B}_{6.5}\text{Ta}_{1.5}$	0.94	0.94	19.8	[225]
$\text{Nd}_{10}\text{Fe}_{80}\text{Zr}_3\text{B}_6\text{C}_1$	1.00	0.94	18.1	[226]
$\text{Nd}_{10}\text{Fe}_{83}\text{B}_6\text{In}_1$	0.83	0.58	18	[228]
$(\text{NdDy})_{11.5}\text{Fe}_{79.5}\text{Nb}_1\text{Zn}_2\text{B}_6$	1.14	0.83	20.6	[229]

**Fig. 29.** TEM images of  $\text{Nd}_{15}\text{Fe}_{77}\text{B}_8$  ribbons melt-spun at the wheel speed 25 m/s (a) without a field and (b) in the field of 0.15 T which is perpendicular to ribbon plane.<sup>[230]</sup>

It is interesting to note that the magnetic field during melt spinning process may also reduce the grain size in the ribbons. Nguyen *et al.* customized a melt spinner which could provide a magnetic field up to 0.32 T parallel or perpendicular to the ribbons plane during the melt-spinning process.<sup>[230,231]</sup> The grain refinement effect was proved by TEM observations in the single-phase  $\text{Nd}_{15}\text{Fe}_{77}\text{B}_8$  ribbons, as shown in Fig. 29. The average grain size of 22 nm for the ribbons prepared under zero field is reduced to 19 nm for the one prepared under a magnetic field of 0.15 T with the field direction perpendicular to the ribbons plane. In addition, the morphologies of the two ribbons are also different. It is observed that the separated small grains are embedded in a matrix with dislocations for the regular ribbons, while only homogenous grains exist in the field-assisted melt-spun ribbons. The reason for the grain size reduction may be explained by the magnetic field induced seed-size reduction effect. Since the iron-rich seeds are formed on the wheel surface where the temperature is far below the Curie temperature of Fe (770 °C), they can be magnetized and absorb energy from an external magnetic field, which could result in the changes in solidification process.<sup>[230]</sup> Similar procedures have been applied

to the field-assisted melt-spun  $\text{Nd}_2\text{Fe}_{14}\text{B}/\text{Fe-Co}$  ribbons with nominal composition  $\text{Nd}_{16}\text{Fe}_{76}\text{B}_8 + 40 \text{ wt.}\% \text{Fe}_{65}\text{Co}_{35}$ .<sup>[231]</sup> A higher magnetic field of about 0.32 T perpendicular to the wheel surface reduces the grain size, increases the texture, improves the exchange coupling, and in sequence, increases the energy product  $(BH)_{\max}$  from 16 to 17.5 MGOe.

### 3.2.3. $\text{Pr}_2\text{Fe}_{14}\text{B}/\alpha\text{-Fe}$

The intrinsic magnetic properties of  $\text{Pr}_2\text{Fe}_{14}\text{B}$  are similar to those of  $\text{Nd}_2\text{Fe}_{14}\text{B}$ , but  $\text{Pr}_2\text{Fe}_{14}\text{B}$  does not have spin reorientation behavior, so it can be used at low temperature. In addition,  $\text{Pr}_2\text{Fe}_{14}\text{B}$  has slightly higher anisotropy field than  $\text{Nd}_2\text{Fe}_{14}\text{B}$ , as shown in Table 5. Therefore,  $\text{Pr}_2\text{Fe}_{14}\text{B}$  is a good candidate for the magnetically hard phase in nanocomposite magnets. To gain best magnetic properties, the optimizations on microstructure such as grain size of both magnetically hard and soft phase, soft phase distribution, grain boundary control are all very important, which is very similar to those observed in  $\text{Nd}_2\text{Fe}_{14}\text{B}/\alpha\text{-Fe}$  nanocomposites. The magnetic properties of melt-spun  $\text{Pr}_2\text{Fe}_{14}\text{B}/\alpha\text{-Fe}$  nanocomposites with different element substitutions are summarized in Table 10.

Goll *et al.* studied the effects of composition on microstructure and magnetic properties of  $\text{Pr}_2\text{Fe}_{14}\text{B}/\alpha\text{-Fe}$  two-phase magnets from the stoichiometric  $\text{Pr}_2\text{Fe}_{14}\text{B}$  to a nominal composition with 54.2 vol%  $\alpha\text{-Fe}$ .<sup>[74]</sup> The room temperature magnetic properties of the  $\text{Pr}_2\text{Fe}_{14}\text{B}/\alpha\text{-Fe}$  ribbons are summarized as a function of the  $\alpha\text{-Fe}$  concentration, as shown in Fig. 30. With an increasing amount of  $\alpha\text{-Fe}$  phase, an enhancement of the remanence is achieved, but a decrease of the coercivity is observed. For the energy product, a maximum value of 22.6 MGOe is found at 30.4 vol%  $\alpha\text{-Fe}$  where the balanced remanence and coercivity are approached. At low  $\alpha\text{-Fe}$  concentrations (< 30 vol%) the coercivity is higher than

one half of the remanence,  $(BH)_{\max}$  sensitively depends on the remanence according to the theoretical upper limit of isotropic sample, i.e.,  $(BH)_{\max} \leq \mu_0 M_r^2/4$ . On the other hand, if at high  $\alpha$ -Fe concentrations ( $> 30$  vol%), the coercivity is too small so  $(BH)_{\max}$  is limited by irreversible demagnetization processes, leading to a drastic decrease energy product. The microstructure of  $\text{Pr}_8\text{Fe}_{87}\text{B}_5$  magnet containing 30.4 vol%  $\alpha$ -Fe is very fine grain, as shown in Fig. 31(a). Even with high-resolution TEM one cannot observe any boundary phase. This

microstructure is clearly different from the decoupled single-phase  $\text{Pr}_{15}\text{Fe}_{78}\text{B}_7$  magnet. Two characteristic maxima in the grain size distribution are observed in the grain size distribution of  $\text{Pr}_{10}\text{Fe}_{84}\text{B}_6$  ribbon containing 14.0%  $\alpha$ -Fe, as shown in Fig. 31(b), which correspond to  $\text{Pr}_2\text{Fe}_{14}\text{B}$  (20–30 nm) and  $\alpha$ -Fe ( $\sim 15$  nm) phases, respectively. This behavior is very similar to that of exchange coupled  $\text{Nd}_2\text{Fe}_{14}\text{B}/\alpha$ -Fe composite magnets.<sup>[73]</sup> This fine microstructure is the key factor to gain such a high energy product in the melt-spun ribbons.

**Table 10.**  $\mu_0 M_r$ ,  $\mu_0 H_c$ , and  $(BH)_{\max}$  of  $\text{Pr}_2\text{Fe}_{14}\text{B}/\alpha$ -Fe nanocomposite magnets with different compositions and different element substitutions.

Composition	$\mu_0 M_r/T$	$\mu_0 H_c/T$	$(BH)_{\max}/\text{MGOe}$	Reference
$\text{Pr}_{12}\text{Fe}_{82}\text{B}_6$ (stoichiometric)	0.95	1.2	19.5	[74]
$\text{Pr}_8\text{Fe}_{87}\text{B}_5$ (30.4 vol% $\alpha$ -Fe)	1.17	0.59	22.6	
$\text{Pr}_{10}\text{Fe}_{84}\text{B}_6$	1.16	0.81	21.3	[240]
$\text{Pr}_7\text{Dy}_1\text{Fe}_{86}\text{B}_6$	1.14	0.66	16.9	[234]
$(\text{Pr}_{0.75}\text{Nd}_{0.25})_2\text{Fe}_{14}\text{B}$	1.06	1.01	23.1	[217]
$\text{Pr}_9\text{Fe}_{76}\text{Co}_{10}\text{B}_5$	1.15	0.63	17.3	[235]
$\text{Pr}_{9.5}\text{Fe}_{78.5}\text{Cr}_2\text{B}_{10}$	0.89	1.16	14.7	
$\text{Pr}_{9.5}\text{Fe}_{78.5}\text{Nb}_2\text{B}_{10}$	0.90	1.32	16.9	
$\text{Pr}_{9.5}\text{Fe}_{78.5}\text{Ti}_2\text{B}_{10}$	0.88	1.28	16.3	[236]
$\text{Pr}_{9.5}\text{Fe}_{78.5}\text{V}_2\text{B}_{10}$	0.89	1.11	15.5	
$\text{Pr}_{9.5}\text{Fe}_{78.5}\text{Zr}_2\text{B}_{10}$	0.88	1.01	14.5	
$\text{Pr}_8\text{Fe}_{84}\text{Nb}_2\text{B}_6$	1.08	0.65	17.9	[97]
$\text{Pr}_9\text{Fe}_{74}\text{Co}_{12}\text{GaB}_5$	1.22	0.65	22.2	[239]
$\text{Pr}_8\text{Fe}_{86.4}\text{B}_5\text{Mn}_{0.6}$	1.33	0.58	23.1	[237]
$\text{Pr}_8\text{Fe}_{85}\text{VB}_6$	1.25	0.62	23.4	[238]
$\text{Pr}_8\text{Fe}_{85}\text{VB}_5\text{C}$	1.22	0.69	21.7	
$\text{Pr}_8\text{Dy}_1\text{Fe}_{74.5}\text{Co}_{10}\text{Nb}_{0.5}\text{B}_6$ (125 MPa)	1.03	0.87	17.1	[233]
$\text{Pr}_8\text{Dy}_1\text{Fe}_{74.5}\text{Co}_{10}\text{Nb}_{0.5}\text{B}_6$ (5 GPa)	1.11	1.02	23.6	

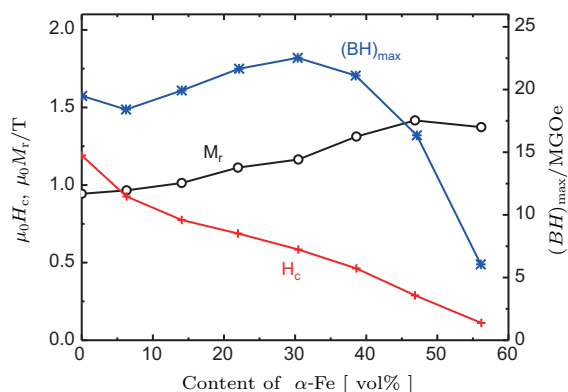


**Fig. 30.** (color online) Magnetic properties as a function of the  $\alpha$ -Fe phase content of nanocomposite  $\text{Pr}_2\text{Fe}_{14}\text{B}/\alpha$ -Fe magnets.<sup>[74]</sup>

The effects of the grain size on magnetic properties of a series of nanocrystalline melt-spun  $\text{Pr}_x\text{Fe}_{94-x}\text{B}_6$  alloys ( $6 \leq x \leq 20$ ) have been investigated by Mendoza–Suárez and Davies.<sup>[232]</sup> It is found that the remanence increases with decreasing grain size up to a maximum at which vitrification is initiated for all cases with different compositions. The intrinsic coercivity also rises with decreasing grain size except for the single-phase near-stoichiometric alloys. The significantly better combinations of coercivity and maximum energy product are obtained for the Pr–Fe–B than for the Nd–Fe–B result-

ing from the higher anisotropy field of the  $\text{Pr}_2\text{Fe}_{14}\text{B}$  phase.  $(BH)_{\max}$  increases with remanence up to 30 vol%  $\alpha$ -Fe content, beyond this point it falls, which agrees with the conclusion reported by Goll *et al.*<sup>[74]</sup>

It is interesting to note that high pressure leads to grain refinement and thus more efficient exchange coupling in the  $\text{Pr}_2\text{Fe}_{14}\text{B}/\alpha$ -Fe nanocomposites. Wang *et al.* reported this high pressure effects in the  $\text{Pr}_8\text{Dy}_1\text{Fe}_{74.5}\text{Co}_{10}\text{Nb}_{0.5}\text{B}_6$  ribbons.<sup>[233]</sup> The grain size of  $\text{Pr}_2\text{Fe}_{14}\text{B}$  phase decreases from 22.5 to 8.7 nm, while the grain size of  $\alpha$ -(FeCo) phase also drops from 30.3 to 10.1 nm, when increasing pressure from 125 MPa to 5 GPa. As a result, the magnetic properties are improved from 1.03 T, 0.87 T, and 17.1 MGOe to 1.11, 1.02 T, and 23.6 MGOe for remanence, coercivity, and energy product, respectively. However, when hot pressing under even higher pressure, the crystallization is constrained and the hot-pressed magnets retains a certain amount of amorphous phase besides the  $\text{Pr}_2\text{Fe}_{14}\text{B}$  and  $\alpha$ -(FeCo) phases, which results in the deterioration of the magnetic properties.

Similar to  $\text{Nd}_2\text{Fe}_{14}\text{B}/\alpha$ -Fe, element substitutions, such as RE, refractory elements, and other elements, can help on grain refinement and grain boundary modifications of the  $\text{Pr}_2\text{Fe}_{14}\text{B}/\alpha$ -Fe magnets, leading to improved magnetic prop-

erties. Chen *et al.* found that Dy substitution for Pr not only increases the coercivity because of the much higher magnetocrystalline anisotropy of  $\text{Dy}_2\text{Fe}_{14}\text{B}$  alloys, but also leads to the microstructure refinement in the  $\text{Pr}_2\text{Fe}_{14}\text{B}/\alpha\text{-Fe}$  nanocomposite magnets.<sup>[234]</sup> An optimum coercivity of 0.66 T is obtained in the  $\text{Pr}_7\text{Dy}_1\text{Fe}_{86}\text{B}_6$  magnet as compared to 0.43 T in the  $\text{Pr}_8\text{Fe}_{86}\text{B}_6$  magnet. As a result, the energy product increases from 9.1 MGOe in the Dy-free magnet to 16.9 MGOe in the 1 at.% Dy magnets, due to the enhanced exchange coupling between the magnetically hard and soft phases. As mentioned in Section 3.2.2, a Pr:Nd ratio of 3:1 in the  $\text{RE}_2\text{Fe}_{14}\text{B}$  magnets generated the best magnetic properties with an energy product of 23.1 MGOe.<sup>[217]</sup>

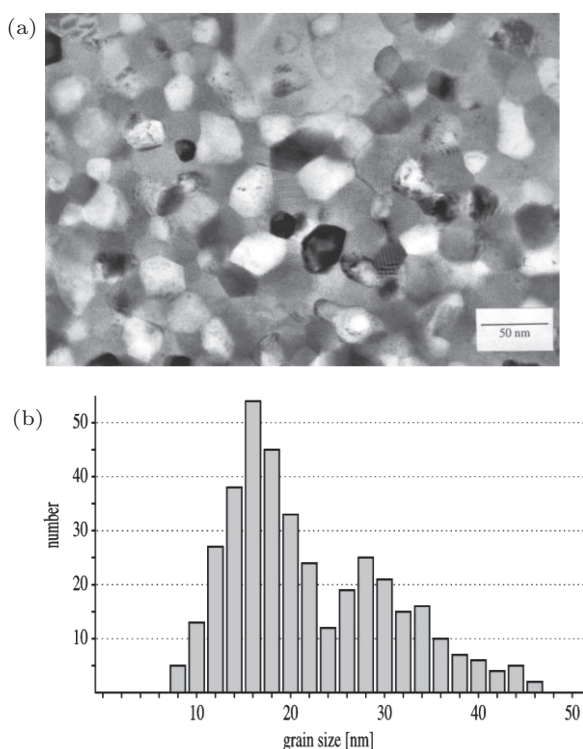


**Fig. 31.** (a) TEM image of a melt-spun  $\text{Pr}_8\text{Fe}_{87}\text{B}_5$  ribbon containing 30.4 vol%  $\alpha\text{-Fe}$ ; (b) grain size distribution of a melt-spun  $\text{Pr}_{10}\text{Fe}_{84}\text{B}_6$  ribbon containing 14.0 vol%  $\alpha\text{-Fe}$ .<sup>[74]</sup>

Zhang *et al.* investigated the Co substitution for Fe in the melt-spun  $\text{Pr}_9\text{Fe}_{86-x}\text{Co}_x\text{B}_5$  ( $x = 0-16$ ) nanocomposites.<sup>[235]</sup> It was found that Co obviously raises the saturated magnetization from 1.50 T for  $\text{Pr}_9\text{Fe}_{86}\text{B}_5$  to 1.80 T for  $\text{Pr}_9\text{Fe}_{76}\text{Co}_{10}\text{B}_5$  (measured under an applied field of 6.5 T), which may be attributed to the formation of  $\alpha\text{-(Fe, Co)}$  phase. At the same time, the remanence, coercivity, and maximum energy product changes from 0.96 T, 0.57 T, and 11.8 MGOe to 1.15 T, 0.63 T, and 17.3 MGOe, respectively. Further substitution of Co for Fe results in a decrease of magnetic properties because of the presence of minor amounts of 1:5 and 2:17 phases. It was also observed that the Curie temperature of the magnetically hard phase increases linearly by increasing Co-substitution at the rate of  $\Delta T_c = 9^\circ\text{C/at}\%$ .

Chang *et al.* found that both  $\text{Pr}_2\text{Fe}_{23}\text{B}_3$  and  $\text{Fe}_3\text{B}$  phases have been completely suppressed and the volume fraction of magnetically hard phase  $\text{Pr}_2\text{Fe}_{14}\text{B}$  increases in the  $\text{Pr}_{9.5}\text{Fe}_{78.5}\text{M}_2\text{B}_{10}$  ( $M = \text{Cr, Nb, Ti, V, and Zr}$ ) ribbons with all the selected refractory element substitutions.<sup>[236]</sup> Accordingly, the coercivity of the ribbons is improved remarkably from 0.83 T for ternary  $\text{Pr}_{9.5}\text{Fe}_{80.5}\text{B}_{10}$  ribbons to 1.01–1.32 T for all chosen refractory element-substituted nanocomposites. The optimal magnetic properties with an energy product of 16.9 MGOe is obtained in Nb-substitution  $\text{Pr}_{9.5}\text{Fe}_{78.5}\text{Nb}_2\text{B}_{10}$  ribbons. Chen *et al.* confirmed that the largest property enhancement is obtained in Nb-substituted  $\text{Pr}_8\text{Fe}_{84}\text{Nb}_2\text{B}_6$  magnets with a coercivity of 0.65 T and a maximum energy product of 17.9 MGOe, as compared to the coercivity of 0.43 T and the energy product of 9.1 MGOe in the  $\text{Pr}_8\text{Fe}_{86}\text{B}_6$  magnets.<sup>[97]</sup> The gain of the magnetic properties is attributed to the most uniform microstructure with the smallest average grain size of 10–20 nm in the Nb-substituted magnets. Ti substitution has a very similar role as Nb substitution in the  $\text{Pr}_2\text{Fe}_{14}\text{B}/\alpha\text{-Fe}$  but with a slightly poorer performance, which is also similar to their function in the  $\text{Nd}_2\text{Fe}_{14}\text{B}/\alpha\text{-Fe}$  nanocomposite magnets.

Yang *et al.* reported significant improvements of microstructure and magnetic properties of  $\text{Pr}_2\text{Fe}_{14}\text{B}/\alpha\text{-Fe}$  nanocomposite magnets by Cu and Mn substitutions for Fe.<sup>[237]</sup> It was found that Mn is more effective on the enhancement of coercivity than Cu. The remanence has maximum values when the content of Cu and Mn reaches 0.2 and 0.6, respectively. The remanence of the ribbons with Mn substitution again has higher value than that with Cu substitution, which may be attributed to magnetic dilute effect of non-magnetic element Cu. The saturated magnetization decreases from 1.68 T for  $\text{Pr}_8\text{Fe}_{87}\text{B}_5$  to 1.61 T for  $\text{Pr}_8\text{Fe}_{86.4}\text{B}_5\text{Cu}_{0.6}$  ribbons, while that of  $\text{Pr}_8\text{Fe}_{86.4}\text{B}_5\text{Mn}_{0.6}$  only decreases to 1.65 T. In comparison with Cu substitution, the Mn substitution significantly improves the  $(\text{BH})_{\text{max}}$ , which mainly results from the stronger exchange-coupling effect due to fineness of grain in the melt-spun  $\text{Pr}_8\text{Fe}_{87-x}\text{B}_5\text{Mn}_x$  ribbons. Excellent magnetic properties with remanence of 1.33 T, coercivity of 0.58 T, and energy product of 23.1 MGOe are obtained in the  $\text{Pr}_8\text{Fe}_{86.4}\text{B}_5\text{Mn}_{0.6}$  ribbons. The authors also studied the effects of addition of V or C or the combined addition on the structure and magnetic properties of melt-spun  $\text{Pr}_8\text{Fe}_{86-x}\text{V}_x\text{B}_{6-y}\text{C}_y$  ribbons.<sup>[238]</sup> Compared with addition-free ribbons, 1 at.% V addition is found to reduce the grain sizes and improve their magnetic properties due to a strong exchange coupling between the magnetically hard and soft phases. A normalized remanence of 0.82, a coercivity of 0.62 T, and a maximum energy product of 23.4 MGOe in melt-spun  $\text{Pr}_8\text{Fe}_{85}\text{VB}_6$  ribbons are obtained at room temperature. The combined addition of V and C leads to the formation of an intermediate phase of VC at grain boundaries, which appears as a pinning

barrier during magnetization and results in a slight increase of the coercivity value to 0.69 T for melt-spun  $\text{Pr}_8\text{Fe}_{85}\text{VB}_5\text{C}$  ribbons. However, energy product drops to 21.7 MGOe for the ribbons with C substitution. Zhang *et al.* studied the effect of Ga additive on the microstructure and magnetic properties of nanocomposite  $\text{Pr}_2(\text{Fe}, \text{Co})_{14}\text{B}/\alpha\text{-(Fe, Co)}$  ribbons.<sup>[239]</sup> The microstructure refinement by introducing 1 at.% Ga leads to a stronger exchange coupling between the magnetically hard and soft phases in comparison with that in Ga-free sample. Therefore, the remanence and energy product increase from 1.14 T, 17 MGOe for Ga-free ribbons to 1.22 T, 22.2 MGOe for the Ga-added ribbons.

### 3.2.4. $\text{Sm}_2\text{Fe}_{15}\text{M}_2\text{C}/\alpha\text{-Fe}$

The compound  $\text{Sm}_2\text{Fe}_{15}\text{Ga}_2\text{C}$  has an anisotropy field exceeding 12 T at room temperature, which is much larger than those of  $\text{Nd}_2\text{Fe}_{14}\text{B}$  and  $\text{Pr}_2\text{Fe}_{14}\text{B}$  (7.6 and 9.0 T, respectively). However, the introduction of nonmagnetic Ga atoms decreases the saturated magnetization monotonically. As a result, the saturated magnetization is only about 1.0 T, which is much lower than those of  $\text{Nd}_2\text{Fe}_{14}\text{B}$  and  $\text{Pr}_2\text{Fe}_{14}\text{B}$ . In order to obtain high-energy product, it is necessary to improve the saturated magnetization and remanence, while keeping the coercivity sufficiently high. Exchange coupled nanocomposite magnets meet this requirement as magnetically hard phase  $\text{Sm}_2\text{Fe}_{15}\text{Ga}_2\text{C}$  can provide large coercivity while magnetically soft phase  $\alpha\text{-Fe}$  can provide high magnetization.

Since Sm is easy to evaporate during alloying, it may be difficult to control the grain size and its distribution precisely by directly melt spinning, especially for the  $\text{Sm}_2\text{Fe}_{15}\text{Ga}_2\text{C}$ -based nanocomposite with low Sm concentration. Cheng *et al.* first fabricated the  $\text{Sm}_2\text{Fe}_{15}\text{Ga}_2\text{C}/\alpha\text{-Fe}$  nanocomposites with low Sm contents directly by melt spinning without a subsequent heat treatment in 1998.<sup>[241]</sup> The alloy with nominal composition  $\text{Sm}_8\text{Fe}_{72}\text{Ga}_8\text{C}_{12}$  was melt-spun at a wheel speed of 15–35 m/s. It was found that the wheel speed affects the microstructure sensitively. The ribbons quenched at 15 and 17.5 m/s are composed of a phase with the  $\text{Th}_2\text{Zn}_{17}$ -type structure and  $\alpha\text{-Fe}$ , while those quenched at 25 m/s and above show nearly complete amorphous state. The average grain size of  $\text{Sm}_2\text{Fe}_{15}\text{Ga}_2\text{C}$  and  $\alpha\text{-Fe}$  are found to decrease with increasing the wheel speed from 140 and 50–60 nm for 15 m/s to 60–70 and 20–30 nm for 18.5 m/s, respectively. A maximum energy product of 5.9 MGOe was obtained for ribbons spun at 17.5 m/s with remanence of 0.71 T and coercivity of 0.55 T. The authors further found that Zr additive in the above nanocomposites could lead to the microstructure refinement and significantly improve the magnetic properties.<sup>[242]</sup> Figure 32 presents the TEM micrographs and the grain size distributions of the Zr-free and Zr-containing samples. It shows that the ribbons contain two different phases, i.e., the major

phase  $\text{Sm}_2\text{Fe}_{15}\text{Ga}_2\text{C}$  with larger grains and the minor phase  $\alpha\text{-Fe}$  with smaller grains. The  $\alpha\text{-Fe}$  grains are located as isolated particles at the grain boundaries of the major phase. The grain size of the Zr-free sample has very broad distributions from 50 to 140 nm for 2:17 phase and from 20 to 50 nm for  $\alpha\text{-Fe}$ . The Zr additive appears to be very successful in retarding the grain growths during crystallization. The grain size of the Zr-containing sample becomes more homogeneous and distributes in the range of 40–70 nm for the 2:17 phase and 13–30 nm for  $\alpha\text{-Fe}$ . The improved microstructure therefore leads to a smoother hysteresis loop and higher remanence in the Zr-containing ribbon, as shown in Fig. 33. As a result, magnetic properties with remanence of 0.72 T, coercivity of 0.77 T, and energy product of 9.0 MGOe were achieved through Zr substitution in the  $\text{Sm}_2\text{Fe}_{15}\text{Ga}_2\text{C}/\alpha\text{-Fe}$  nanocomposites.

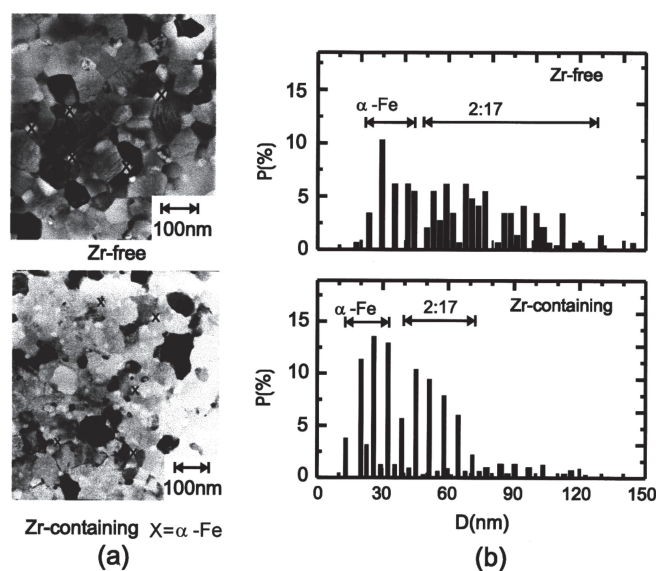


Fig. 32. (a) TEM images and (b) grain size distributions for the Zr-free ( $\text{Sm}_8\text{Fe}_{72}\text{Ga}_8\text{C}_{12}$ ) and Zr-containing ( $\text{Sm}_{7.9}\text{Fe}_{71.3}\text{Ga}_{7.9}\text{Zr}_1\text{C}_{11.9}$ ) ribbons.<sup>[242]</sup>

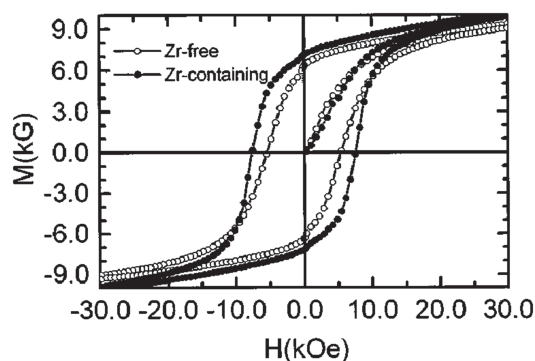


Fig. 33. Room-temperature hysteresis loops of the Zr-free ( $\text{Sm}_8\text{Fe}_{72}\text{Ga}_8\text{C}_{12}$ ) and Zr-containing ( $\text{Sm}_{7.9}\text{Fe}_{71.3}\text{Ga}_{7.9}\text{Zr}_1\text{C}_{11.9}$ ) ribbons.<sup>[242]</sup>

Zhang *et al.* studied the magnetic properties of  $\text{Sm}_2\text{Fe}_{15}\text{Si}_2\text{C}/\alpha\text{-Fe}$  nanocomposites with Cu additive, which are prepared by melt spinning at wheel speed of 20 m/s.<sup>[243]</sup> The average grain size of 2:17 carbides and  $\alpha\text{-Fe}$  in the rib-

bons is about 50 and 30 nm, respectively. The ribbons exhibit a single hard magnetic phase behavior and remanence enhancement due to inter-grain exchange coupling between magnetically hard and soft phases. The remanence increases with the increase of  $\alpha$ -Fe phase content in ribbons, while the coercivity decreases rapidly, which agrees with the correlation between remanence and coercivity in other nanocomposite magnets. The highest maximum energy product around 10.7 MGOe was obtained for  $\text{Sm}_8\text{Fe}_{76}\text{Cu}_4\text{Si}_8\text{C}_4$  ribbons with a coercivity of 0.5 T.

The effect of pressure on the microstructure of  $\text{Sm}_2(\text{Fe},\text{Si})_{17}\text{C}_x/\alpha$ -Fe nanocomposite magnets has been studied by Zhang *et al.* through pressing the amorphous  $\text{Sm}_8\text{Fe}_{85}\text{Si}_2\text{C}_5$  alloy under pressures up to 6 GPa at 650 °C.<sup>[244]</sup> The grain size of  $\alpha$ -Fe and  $\text{Sm}_2(\text{Fe},\text{Si})_{17}\text{C}_x$  decreases from 30.6 to 6.4 and from 28.5 to 5.8 nm, respectively. The volume fraction of the 2:17-type carbide increases with increasing pressure. A significant increase in both remanence and coercivity, comparing to those prepared under normal pressure, is observed in the nanocomposites prepared under high pressure. As a result, an energy product is significantly improved in the  $\text{Sm}_2(\text{Fe},\text{Si})_{17}\text{C}_x/\alpha$ -Fe nanocomposites.

**Table 11.**  $\mu_0M_r$ ,  $\mu_0H_c$ , and  $(\text{BH})_{\text{max}}$  of  $\text{Sm}_2\text{Fe}_{15}\text{M}_2\text{C}/\alpha$ -Fe ( $M = \text{Ga}, \text{Si}$ ) nanocomposite magnets with different compositions and different element substitutions

Composition	$\mu_0M_r/\text{T}$	$\mu_0H_c/\text{T}$	$(\text{BH})_{\text{max}}/\text{MGOe}$	Reference
$\text{Sm}_8\text{Fe}_{72}\text{Ga}_8\text{C}_{12}$	0.71	0.55	5.9	[241]
$\text{Sm}_{7.9}\text{Fe}_{71.3}\text{Ga}_{7.9}\text{Zr}_{1.1}\text{C}_{11.9}$	0.72	0.77	9.0	[242]
$\text{Sm}_8\text{Fe}_{76}\text{Cu}_4\text{Si}_8\text{C}_4$	0.78	0.50	10.7	[243]
$\text{Sm}_8\text{Fe}_{85}\text{Si}_2\text{C}_5$ (4 GPa)	0.88	0.62	N/A	[244]

### 3.3. Precipitation-hardening ribbons

The 2:17-type  $\text{Sm}(\text{CoFeCuZr})_z$  magnets, having the highest Curie temperature among the commercial rare-earth permanent magnets, have attracted considerable interest for high-temperature applications since 1970 s, because of their large energy products and high temperature performance.<sup>[245]</sup> Their high coercivity is widely believed to be domain-wall-pinning control, which is attributed to the cellular microstructure having a 2:17 matrix and 1:5 precipitates around the grain boundaries of the 2:17 phase. Therefore, these 2:17-type magnets are also called as precipitation-hardened magnets. In addition to the cellular microstructure, a platelet phase of few nanometers in width which is orientated perpendicular to the c axis is superimposed on the cellular microstructure. This so-called lamellar Z phase extends through quite a lot of cells and cell boundaries and is believed to be of the hexagonal 2:17 structure or of the rhombohedral 1:3 structure. The special microstructure in the conventional sintered magnets is usually obtained through a complex heat treatment, as schematized in Fig. 34, following the sequences: homogenizing at

$T_h = 1100\text{--}1200$  °C for hours and quenching to room temperature, the magnets are isothermally aged at  $T_a = 800\text{--}900$  °C for  $t_a = 10\text{--}25$  h, succeeded by a slow cooling rate of  $v_c = 0.5\text{--}1$  °C/min down to 400 °C or lower, then finished by quenching to room temperature. Each step is very important in order to achieve the desired microstructure and magnetic properties. Besides the heat treatment, the chemical composition is also very important for the microstructure and thus magnetic properties. Each element plays its own unique roles in the  $\text{Sm}(\text{CoFeCuZr})_z$  magnets. Besides the high temperature performance, it is interesting to note that an abnormal temperature dependence of coercivity, i.e., the coercivity increasing with temperature and reaching a maximum at around 500 °C, is observed in the  $\text{Sm}(\text{CoFeCuZr})_z$  magnets with low Cu content, which could be attributed to the change of coercivity mechanism at different temperature.<sup>[246,247]</sup> The research progresses and the details of the sintered  $\text{Sm}(\text{CoFeCuZr})_z$  precipitation hardened magnets are summarized in the article reviewed by Liu.<sup>[248]</sup> This review only focuses on the recent developments on the melt-spun precipitation-hardened magnets, which attracts the interests of researchers due to the simplified routes, comparing to conventional sintered magnets.

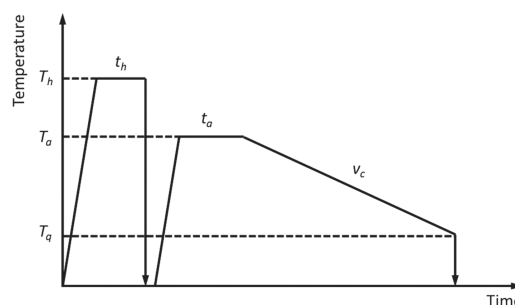


**Fig. 34.** Typical temperature profile of the heat treatment for sintered precipitation-type magnets.

#### 3.3.1. Simplified process

Doll *et al.* fabricated the precipitation-hardened ribbons through the melt spinning process and appropriate post heat treatment for the first time.<sup>[249]</sup> Although the alloys are prepared by melt spinning, however, the annealing procedure is very similar to that of conventional sintered magnets, i.e.,  $T_h = 1160$  °C,  $t_h = 30$  min,  $T_a = 840$  °C,  $t_a = 19$  h, and cooling rate of 0.75 °C/min. TEM analysis shows that a rhombic structure parallel to the c axis and a hexagonal network in the basal plane are formed in the ribbons after annealing, which is very similar to the microstructure of the sintered magnets. The characteristic cell size is about 50–70 nm, which depends on the composition. Figure 35 shows the temperature dependence of the coercivity for both magnets in comparison with three other common permanent magnetic materials, namely  $\text{Nd}_2\text{Fe}_{14}\text{B}$ , Sr ferrite and  $\text{AlNiCo}$ , respectively. For the Cu/Fe-rich sample, the coercivity decreases with increasing temper-

ature, i.e., a normal behavior of coercivity with negative temperature coefficient. In contrast, the coercivity of the Cu/Fe-poor magnet changes only slightly from room temperature to 500 °C and even shows a positive temperature coefficient in the temperature range between 227 °C and 427 °C. The coercivity reached a maximum of 0.4 T at 427 °C. To understand the different coercivity behavior, EDX was scanned from one 2:17 cell over a 1:5 cell boundary into another 2:17 cell for the Cu/Fe-poor magnet. It is clear that Cu have much higher concentration in the grain boundary 1:5 phase than the cell 2:17 phase. Although the mechanism is still a matter of debate, it is agreed that the abnormal coercivity behavior is related to the Cu-profile along the grain boundary phase.

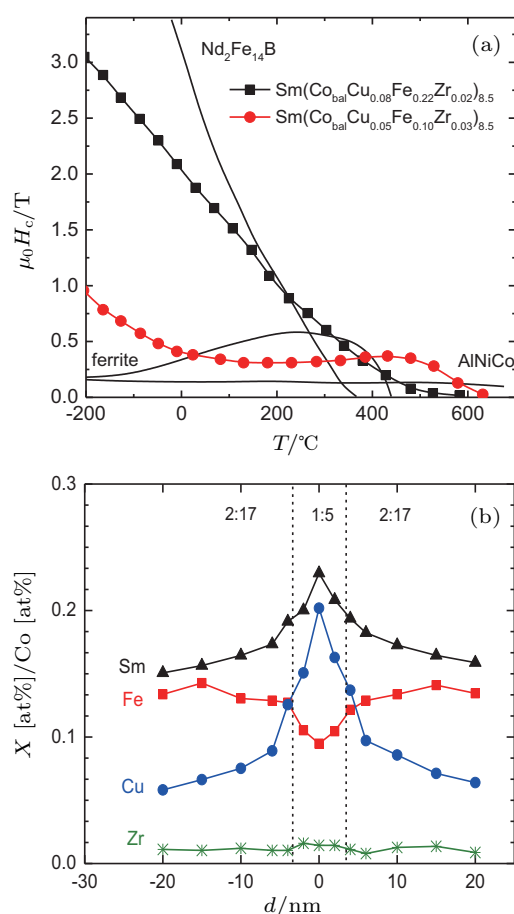


**Fig. 35.** (color online) (a) Temperature dependence of the coercivity of Cu/Fe-rich and Cu/Fe-poor in comparison with other common permanent magnetic materials; (b) EDX profiles of Sm, Cu, Fe, and Zr (contents standardized to the Co content) in the vicinity of a 2:17/1:5 phase boundary in Cu/Fe-poor magnet.<sup>[249]</sup>

Yan *et al.* further simplified the process for the melt-spun  $Sm(CoFeCuZr)_z$  ribbons and found that the homogenizing process (solid solution treatment) actually is not necessary.<sup>[250]</sup> They compared the magnetic hardening processes of the  $Sm(Co_{0.74}Fe_{0.1}Cu_{0.12}Zr_{0.04})_{7.5}$  ribbons with and without solid solution treatment (homogenizing at 1160 °C for 4 hours). The coercivity of the ribbons with solid solution treatment continues to increase with longer isothermal

aging time and a value of 2.4 T is obtained after aging for 12 h at 850 °C, as shown in Fig. 36(a). This behavior is very similar to that found in conventional precipitation-hardened  $Sm(CoFeCuZr)_z$  magnets. However, quite different behavior is observed in the ribbons without solid solution treatment. A very high coercivity of 2.8 T is developed by simply slow cooling from 850 to 400 °C, without isothermal aging, which is much higher than that of homogenized ribbons subjected to the same aging process (1.64 T). A short aging time about 3 h could bring the coercivity to its maximum of about 3.0 T. This behavior could be attributed to the already formed 1:7 phase in the melt-spun ribbon which is the final product with supersaturated Cu and Zr in the phase of the homogenizing process for the conventional  $Sm(CoFeCuZr)_z$  alloys. The 1:7 phase is believed to play important roles in developing the cellular/lamellar microstructure and high coercivity. TEM images shown in Fig. 36(b) confirmed that the microstructure, consisting of cellular and lamellar phases, was formed in the ribbon without solid solution treatment. Therefore, the time consuming and intricate aging regimen, which is normally required to develop high coercivity for bulk  $Sm(CoFeCuZr)_z$  permanent magnets, is significantly simplified in melt-spun materials, i.e., the precipitation hardening is realized in melt-spun ribbons by simply slow cooling from 850 to 400 °C.

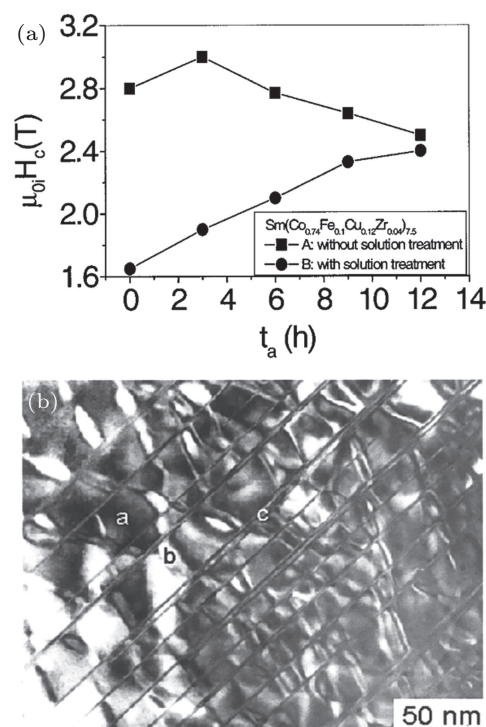


**Fig. 36.** (a) Evolution of the coercivity dependent on the isothermal aging time at 850 °C for the  $Sm(Co_{0.74}Fe_{0.1}Cu_{0.12}Zr_{0.04})_{7.5}$  ribbons with and without solid solution treatment; (b) typical TEM micrographs of samples without solution treatment.<sup>[250]</sup>

It is very interesting that Yan *et al.* observed the disappearance of the large coercivity in the above melt-spun  $Sm(CoFeCuZr)_z$  magnet by an additional short time

aging.<sup>[251]</sup> Figure 37(a) shows the coercivity dependence of the ribbons on the aging temperature of the additional aging process while the aging time is fixed at 5 min. One can see that higher aging temperatures lead to a more significant loss in the coercivity and the ribbons subjected to aging at 850 °C for only 5 minutes showed a very low coercivity of 0.16 T, which is far lower than the coercivity of 3.0 T of the original ribbon without aging. It should be noted that no change in the coercivity was observed after further increasing the aging time. The dramatic change of coercivity should be attributed to the Cu distribution across the 1:5 grain boundary phase. Figure 37(b) shows the nanoprobe EDX microanalysis profiles of Cu obtained by a line scan across the interface between

the 2:17 matrix and the 1:5 in the ribbons with and without additional aging process. A very sharp peak of Cu content (24 at.%) was detected in the middle of the 1:5 phase indicating that the Cu distribution in the cell boundary is highly inhomogeneous, which is similar to that observed in Ref. [249]. After the additional short-time aging at 850 °C, the Cu distribution in the 1:5 boundary phase becomes more homogenous and the large gradient of Cu content is no longer detectable. Therefore, the high coercivity in the melt-spun precipitation hardened magnet is proposed to be originated from the large gradient of domain wall energy within the 1:5 grain boundary phase and not from the Cu diffusion from 2:17 phase to 1:5 phase.

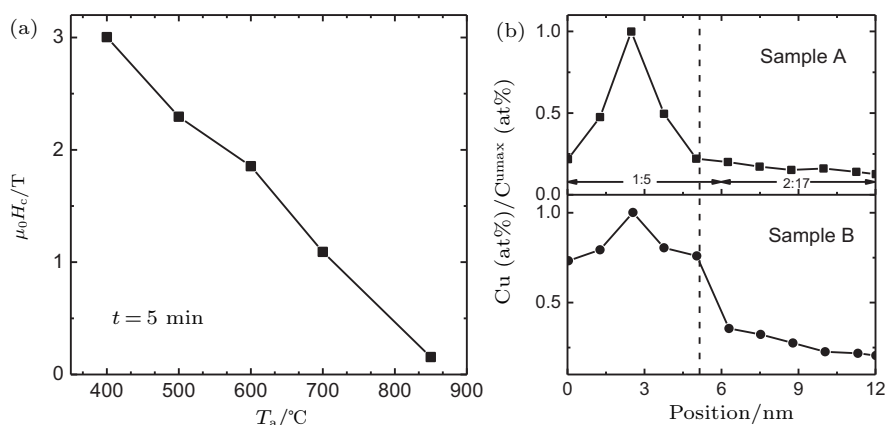


**Fig. 37.** (a) Dependence of the coercivity of  $\text{Sm}(\text{Co}_{0.74}\text{Fe}_{0.1}\text{Cu}_{0.12}\text{Zr}_{0.04})_{7.5}$  ribbons on aging temperature (additional isothermal aging for 5 min); (b) nanoprobe EDX profiles of Cu across the interface between the 2:17 matrix and the 1:5 grain boundary of the ribbons before (sample A) and after (sample B) additional aging at 850 °C for 5 min.<sup>[251]</sup>

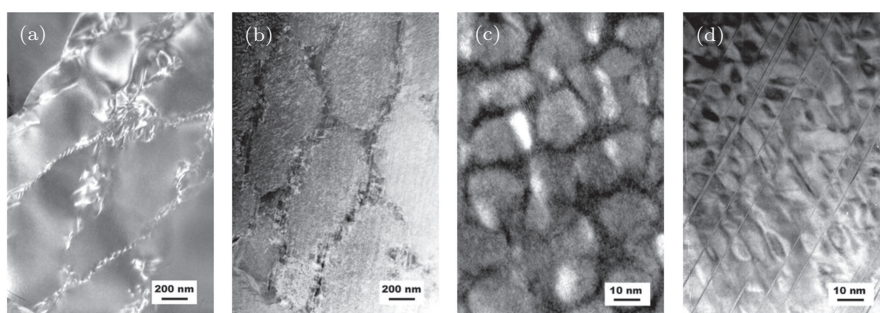


**Fig. 38.** TEM micrographs of the  $\text{Gd}(\text{Co}_{0.88-x}\text{Cu}_x\text{Fe}_{0.09}\text{Zr}_{0.03})_7$  ribbons. (a) As-spun; (b) precipitation-hardened without isothermal aging; (c) and (d) one 1:7 region of (b) which is observed perpendicular and parallel to the c axis, respectively.<sup>[252]</sup>

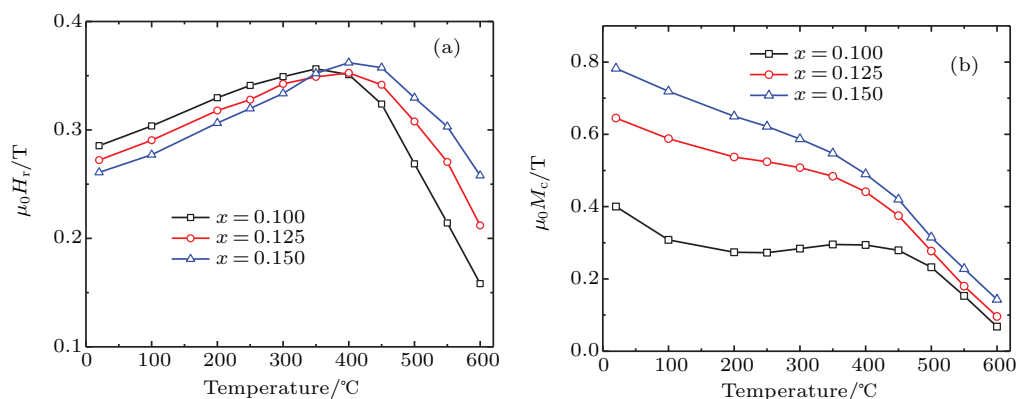


**Fig. 39.** (color online) Temperature dependences of remanence and coercivity of the precipitation-hardened  $\text{Gd}(\text{Co}_{0.88-x}\text{Cu}_x\text{Fe}_{0.09}\text{Zr}_{0.03})_7$  ribbons without isothermal aging.<sup>[252]</sup>

Rong *et al.* found that the TbCu<sub>7</sub>-type 1:7 phase is formed by direct melt spinning in the Gd(Co<sub>0.88-x</sub>Cu<sub>x</sub>Fe<sub>0.09</sub>Zr<sub>0.03</sub>)<sub>7</sub> alloy as well.<sup>[252]</sup> It is confirmed that solid solution treatment and the isothermal aging are not necessary for precipitation hardening in the melt-spun materials, i.e., high coercivity can be obtained by simply slow cooling the ribbons from 850 to 400 °C. Figure 38 shows the microstructure of the as-spun and precipitation-hardened Gd(Co<sub>0.88-x</sub>Cu<sub>x</sub>Fe<sub>0.09</sub>Zr<sub>0.03</sub>)<sub>7</sub> ribbons. TEM studies reveal that the as-spun ribbons are quite heterogeneous consisting of large crystalline areas, which mainly have a TbCu<sub>7</sub>-type structure, as shown in Fig. 38(a). The grain boundaries remain in the precipitation-hardened ribbons, as shown in Fig. 38(b). EDX analysis shows that the 1:7 phase boundary is composed of a Gd-rich phase and its composition is almost unchanged before and after the heat treatment. The mean size of the 1:7 regions is about 1 μm. The microstructure of one 1:7 region, as presented in Figs. 38(c) and 38(d), shows clearly that the cellular structure, which consists of a Fe-rich 2:17 cell phase, a Cu-rich 1:5 cell boundary phase, and a Zr-rich platelet phase, is obtained by the simple annealing treatment. Interestingly, the cell size is only about 10–20 nm which is much smaller than that of typical sintered magnets. The cell boundaries are about 2–5 nm in width and are coherent to the cellular grains. However, no cellular microstructure is formed in the 1:7 phase boundaries. The temperature dependences of remanence and coercivity of precipitation-hardened Gd(Co<sub>0.88-x</sub>Cu<sub>x</sub>Fe<sub>0.09</sub>Zr<sub>0.03</sub>)<sub>7</sub> ribbons without isothermal ag-

ing are given in Fig. 39. All ribbons exhibit a positive temperature coefficient of remanence from RT to about 400 °C. This is a consequence of the antiparallel coupling between Gd and Co magnetic moments. Since the rare-earth sublattice disorders rapidly increase with temperature, the ferromagnetic coupling of Gd–Co magnets results in an increasing magnetization with increasing temperature. Abnormal coercivity (positive temperature coefficient) is only observed in ribbons with  $x = 0.10$ . Further addition of Cu causes the monotonic temperature dependence of coercivity.

### 3.3.2. Texture development in melt-spun ribbons

Besides the simplified precipitation hardening process, texture can be developed in melt-spun Sm(CoFeCuZr)<sub>z</sub> ribbons, without the conventional sintering process. Therefore, a relatively high energy product can be obtained in such ribbons. Rong *et al.*<sup>[253,254]</sup> and Yan *et al.*<sup>[139]</sup> have studied the effects of composition on the crystallographic texture of the precipitation-hardened Sm(Co<sub>1.0-x-y-w</sub>Cu<sub>x</sub>Fe<sub>y</sub>Zr<sub>w</sub>)<sub>z</sub> ( $x = 0-0.25$ ,  $y = 0-0.30$ ,  $w = 0-0.10$ , and  $z = 6.5-7.5$ ) ribbons, which were melt-spun at low wheel speed of 5 m/s. The results are summarized below.

**Effect of  $z$  value (or Sm content).** The studies show that the  $z$  value or Sm content has little influence on the crystallographic texture of the melt-spun ribbon, as reported by both Rong *et al.*<sup>[253]</sup> and Yan *et al.*<sup>[139]</sup>

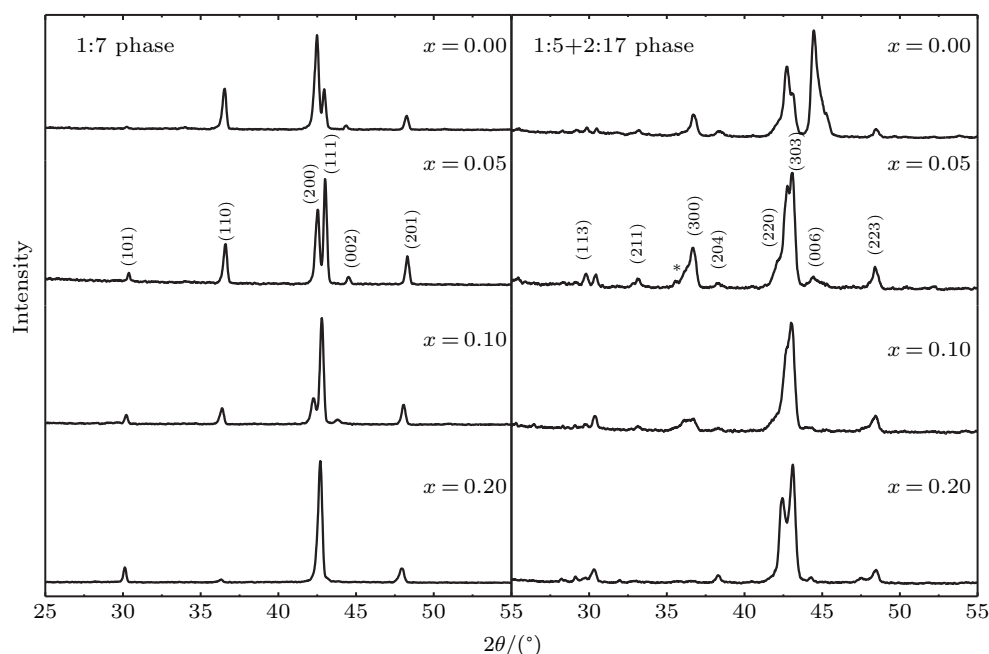
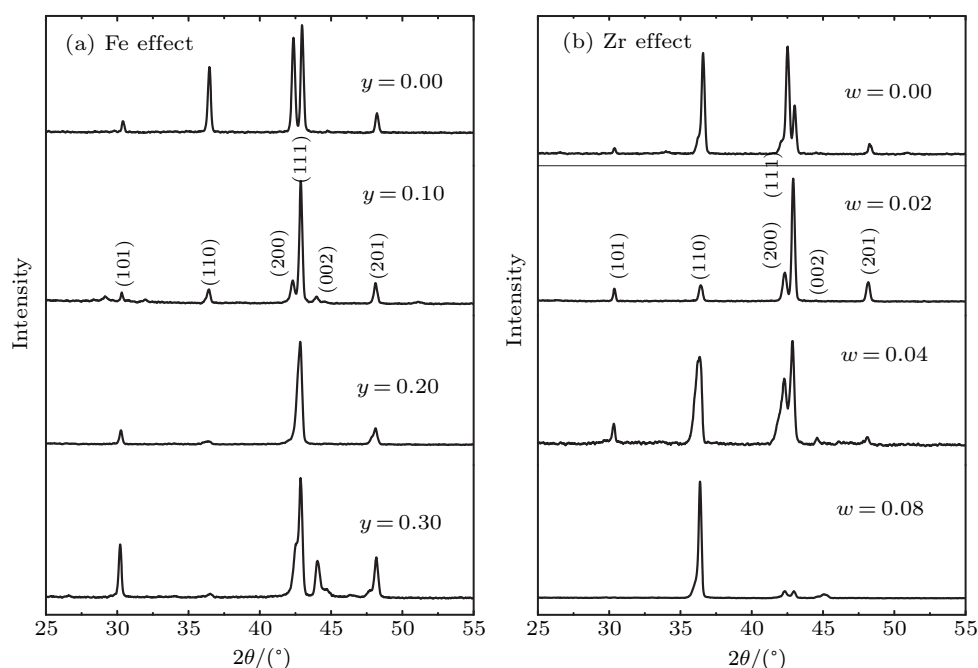


Fig. 40. XRD patterns of melt-spun and precipitation-hardened Sm(Co<sub>0.87-x</sub>Cu<sub>x</sub>Fe<sub>0.1</sub>Zr<sub>0.03</sub>)<sub>7</sub> ribbons with different Cu contents.<sup>[253]</sup>

**Effects of Cu.** Figure 40 shows the typical XRD patterns of the melt-spun and precipitation-hardened Sm(Co<sub>0.87-x</sub>Cu<sub>x</sub>Fe<sub>0.1</sub>Zr<sub>0.03</sub>)<sub>7</sub> ribbons with different Cu contents. The significantly enhanced intensity of the (200) and

(110) peaks for the Cu-free ribbon suggests that they are crystallographically anisotropic with easy magnetization direction parallel to the longitudinal direction of the ribbons. However, a small quantity of Cu substitution ( $x = 0.05$ ) leads to a sig-

nificant increase in the intensity of (111) reflection, which is close to that expected for isotropic materials, indicating that no crystallographic texture is present in the ribbons. Further addition of Cu leads to stronger intensity of (111) peak and disappearance of (200) and (110) peaks, indicating that the degree of crystallographic texture increases with increasing Cu content. After precipitation hardening through isothermal aging at 850 °C for 3 hours, the 1:7 phase is segregated into 1:5 and 2:17 phases. The broadened peaks of the precipitation-hardened samples indicate that phase transformation leads to the formation of a fine microstructure. The crystallographic texture is preserved in ribbons after precipitation hardening.



**Fig. 41.** XRD patterns of the melt-spun ribbons (a)  $\text{Sm}(\text{Co}_{0.87-y}\text{Fe}_y\text{Cu}_{0.1}\text{Zr}_{0.03})_7$  with different Fe contents; (b)  $\text{Sm}(\text{Co}_{0.8-w}\text{Fe}_{0.1}\text{Cu}_{0.1}\text{Zr}_w)_7$  with different Zr contents.<sup>[253,254]</sup>

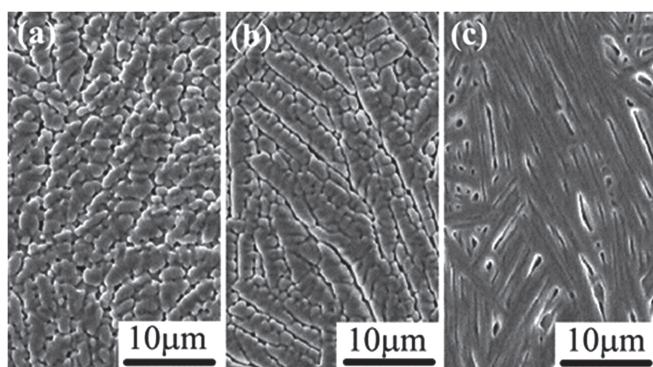


**Fig. 42.** (color online) SEM images of the free surface of melt-spun  $\text{Sm}(\text{Co}_{0.8-w}\text{Fe}_{0.1}\text{Cu}_{0.1}\text{Zr}_w)_7$  ribbons: (a)  $w = 0.01$ , (b)  $w = 0.04$ , and (c)  $w = 0.08$ .<sup>[254]</sup>

**Effects of Zr.** Figure 41(b) shows the XRD patterns of the melt-spun  $\text{Sm}(\text{Co}_{0.8-w}\text{Fe}_{0.1}\text{Cu}_{0.1}\text{Zr}_w)_7$  ribbons with different Zr contents. Again, all as-spun ribbons consist of a single TbCu<sub>7</sub>-type phase. The significantly enhanced intensity of

**Effects of Fe.** Figure 41(a) shows the XRD patterns of the melt-spun  $\text{Sm}(\text{Co}_{0.87-y}\text{Fe}_y\text{Cu}_{0.1}\text{Zr}_{0.03})_7$  ribbons with different Fe contents. The as-spun ribbons consist mainly of a single TbCu<sub>7</sub>-type phase. The intensity of the diffraction peaks of the Fe-free ribbons is close to those of isotropic materials, indicating no obvious texture in the ribbons. The addition of Fe leads to significantly enhanced intensity of (111) peak in the ribbons with  $y = 0.2$ , which indicates the increase of texture degree with increasing Fe content. However, further addition of Fe leads to the disappearance of crystallographic texture in the ribbons.

the (200) and (110) peaks for the Zr-free ribbons suggests that they are crystallographic anisotropic with easy magnetization direction parallel to the longitudinal direction of the ribbons. However, no obviously preferential orientation is observed in the samples with  $w \leq 0.03$ , which agrees with the results reported in Ref. [139]. It is interesting to note that partially preferential orientation starts to form with Zr content  $w = 0.04$ . Further Zr substitution leads to a more pronounced increase in the intensity of (110) peak and the perfect crystallographic texture is obtained in the ribbons with  $w = 0.08$ . Due to the appearance of 2:7 phase, the crystallographic texture disappears in the ribbons with  $w \geq 0.09$ . It is also found that Zr substitution results in a significant modification to the microstructure of the ribbons surface. Figure 42 shows the SEM micrographs of the free surface of the as-spun ribbons with different Zr content. The small grains of approximately 1 μm in diameter are obtained in the isotropic ribbon with  $w = 0.01$ . Whereas,

the columnar dendrite grains, with their long axes mainly parallel to the longitudinal axes of the ribbons, start to form in the ribbon with  $w = 0.04$ . The average grain size is about 2–15  $\mu\text{m}$ . With further Zr substitution, it can be found clearly that the columnar dendrite grains arrange more formally and compactly than those of low Zr content ribbons. It is suggested that the Zr addition favors the formation of preferential orientation, which agrees closely with the XRD analyses given in Fig. 41(b).

### 3.3.3. Optimization of magnetic properties

The desired magnetic properties of  $\text{Sm}(\text{CoFeCuZr})_z$  ribbons are controlled not only by the composition and texture, but also by the heat-treatment process, i.e., the isothermal temperature and time, the cooling rate, and the final quench temperature. The systematically work to optimize the magnetic properties of  $\text{Sm}(\text{CoFeCuZr})_z$  melt-spun ribbons was reported in Refs. [253] and [255].

Figure 43 summarizes the compositional dependence of  $\mu_0 M_r$ ,  $\mu_0 H_c$ , and  $(\text{BH})_{\text{max}}$  of precipitation-hardened

$\text{Sm}(\text{Co}_{1.0-x-y-w}\text{Cu}_x\text{Fe}_y\text{Zr}_w)_z$  ribbons. It should be noted that the remanence is determined by both the composition and texture. As a general rule, remanence increases with increasing the content of Fe/Co content and the preferred crystallographic texture, while decreases with increase of Zr/Cu content, as shown in Fig. 43(a). Coercivity, on the other hand, mainly relies on the composition and its related effects on the microstructure, but not the texture. As one can see in Fig. 43(b), all elements play an important role in the development of coercivity, which has been reported in both melt-spun ribbons and conventional sintered  $\text{Sm}(\text{CoFeCuZr})_z$  magnets. The coercivity is less than  $< 0.5$  T if any of the elements is missed. Among the elements, Cu has the biggest impact on coercivity of the precipitation-hardened magnets. The ribbons without Cu show coercivity about zero, while a high Cu content about  $x = 0.15$ – $0.20$  can lead to a coercivity about 3.0 T at room temperature. With a controlled composition and related texture, the maximum energy product around 11 MGOe at room temperature is achieved in the  $\text{Sm}(\text{Co}_{1.0-x-y-w}\text{Cu}_x\text{Fe}_y\text{Zr}_w)_z$  ribbons by the above-mentioned simple process.

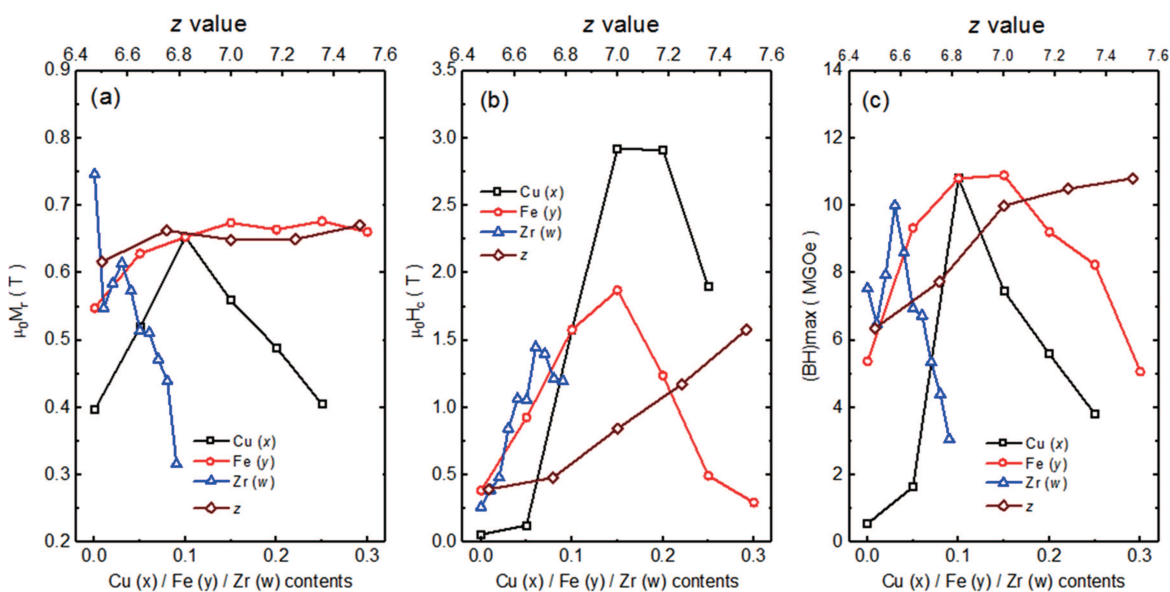


Fig. 43. (color online) The compositional dependence of (a)  $\mu_0 M_r$ , (b)  $\mu_0 H_c$ , and (c)  $(\text{BH})_{\text{max}}$  of precipitation-hardened  $\text{Sm}(\text{Co}_{1.0-x-y-w}\text{Cu}_x\text{Fe}_y\text{Zr}_w)_z$  ribbons.<sup>[253]</sup>

Besides the composition, the control of precipitation hardening process is another critical factor for the coercivity development in  $\text{Sm}(\text{CoFeCuZr})_z$  ribbons. Figure 44 shows the room-temperature coercivity of  $\text{Sm}(\text{Co}_{0.87-x}\text{Fe}_{0.1}\text{Cu}_x\text{Zr}_{0.03})_7$  ribbons as a function of isothermal aging temperature ( $T_a$ ), aging time ( $t_a$ ), cooling rate ( $v_c$ ), and quenching temperature ( $T_q$ ). It should be noted that the results in Fig. 44 give one fact at a time, i.e., all other parameters are fixed when one factor is studied. The coercivity dependences on these parameters are summarized below.

(i) Coercivity is low when  $T_a$  is lower than 750  $^\circ\text{C}$ , while it increases quickly with varying  $T_a$  up to 900  $^\circ\text{C}$ . Further in-

crease of  $T_a$  to 950  $^\circ\text{C}$  and above leads to a drop of coercivity.

(ii) The optimized  $t_a$  depends on the composition. For example, the coercivity of the ribbons with Cu content  $x = 0.15$  increases monotonically until  $t_a = 3$ – $5$  h and then rarely changes with longer aging time. However, the coercivity of the ribbons with  $x = 0.25$  reaches a maximum at  $t_a = 1$  h (not shown in the figure), i.e., a short-time aging is enough to develop the coercivity and a long-time aging deteriorates the ribbons.

(iii) The coercivity increases monotonically with reducing the cooling rate  $v_c$ , although degree of influence may rely on the composition, such as Cu content. This is understand-

able as Cu diffusion happens at this stage. For the ribbons with larger Cu content, the Cu concentration in the 1:5 boundary phase may be saturated faster, so an extremely low  $v_c$  may not help to increase the coercivity. However, for the ribbons with lower Cu content, a very low  $v_c$  could lead more Cu diffused into the 1:5 boundary phase and thus significant increase of coercivity.

The coercivity increases fast with a decrease in the quenching temperature  $T_q$ . Similar to the effects of  $v_c$  during the slow cooling, the decrease in  $T_q$  leads to an increase of Cu concentration in the 1:5 boundary phase and thus an increase in coercivity.

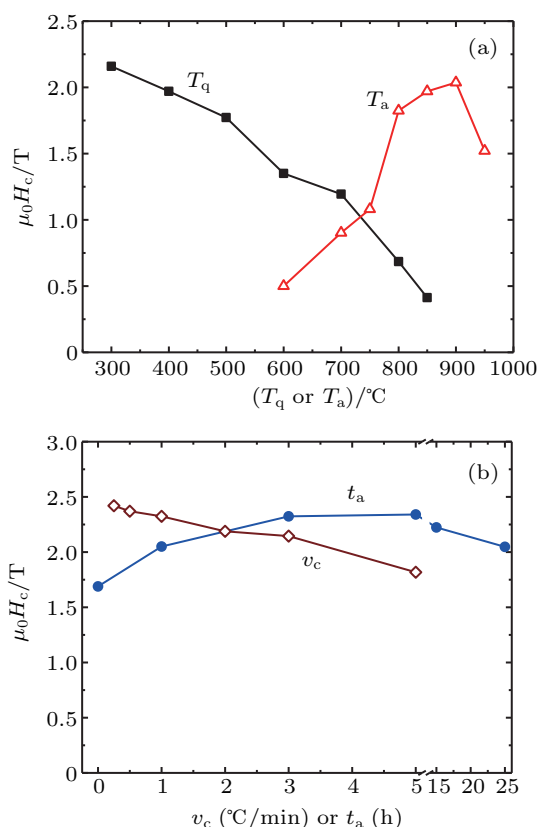


**Fig. 44.** (color online) The effects of isothermal aging temperature ( $T_a$ ), aging time ( $t_a$ ), cooling rate ( $v_c$ ), and quench temperature ( $T_q$ ) on the room-temperature coercivity of  $\text{Sm}(\text{Co}_{0.72}\text{Fe}_{0.1}\text{Cu}_{0.15}\text{Zr}_{0.03})_7$  ribbon. [255]

As mentioned above, the composition affects temperature dependence of coercivity  $H_c(T)$ . In fact, all parameters of the precipitation hardening process affect the temperature dependence of coercivity as well. Figure 45 shows the  $H_c(T)$  curves of the  $\text{Sm}(\text{Co}_{0.77}\text{Fe}_{0.1}\text{Cu}_{0.1}\text{Zr}_{0.03})_7$  ribbons quenched at different temperature  $T_q$ , as an example. The anomalous temperature dependence of coercivity can be obtained in the ribbons with  $T_q \geq 500$  °C. In addition, the tendency of the abnormal temperature dependence of coercivity gradually disappears with decreasing  $T_q$ . Besides the quenching temperature, other annealing parameters such as  $T_a$ ,  $t_a$ , and  $v_c$  significantly affect the  $H_c(T)$  curves as well. The details can be

found in Ref. [255]. All relations between  $H_c(T)$  curves and the annealing parameters may be explained by the change of microstructure and microchemistry, which leads to a variation of the distribution and amount of Cu in the 1:5 cell boundaries.

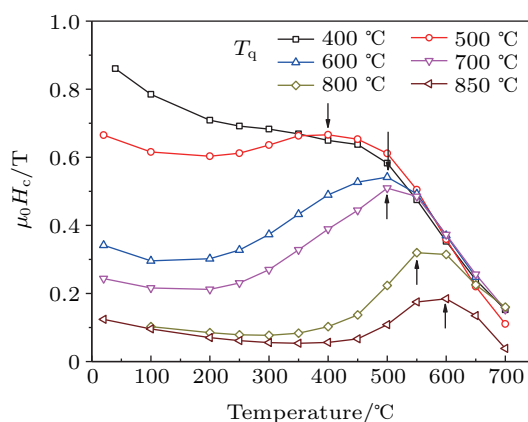


**Fig. 45.** (color online)  $H_c(T)$  curves of the  $\text{Sm}(\text{Co}_{0.77}\text{Fe}_{0.1}\text{Cu}_{0.1}\text{Zr}_{0.03})_7$  ribbons with different quenching temperatures. [255]

#### 4. Magnetic phenomena in melt-spun magnets

Exchange coupling is the way in which two magnetic atoms in a material interact with each other. When two magnetic atoms are situated very close together, their electrons can interact directly, in the same way as when forming a chemical bond. This type of exchange coupling is the way happened in the magnetic materials. The generalized intergrain exchange coupling (IGEC) actually includes inter-phase exchange coupling which happens between two phases in the nanocomposite magnets, and the inter-grain exchange coupling between the grains with the same phase which could happen in either single-phase nanocrystalline magnets or nanocomposite magnets. The IGEC plays the key role in determining the magnetic properties for nanostructured magnetic materials, especially for nanocomposite magnets. It should be noted that the discussions in this section are not limited to the melt-spun materials but they may be extended to any nanocrystalline magnets fabricated by other techniques, such as ball milling, thin-film technologies, self-assembly.

##### 4.1. Single-phase magnetic behavior

If a two-phase nanocomposite magnet has microstructure with fine grains and homogenous distributed magnetically soft-phase together with strong IGEC, it should demonstrate a one-step reversal behavior in the demagnetization curve, i.e., there is no “kink” in the curve, which is the so-called single-phase magnetic behavior. However, if the IGEC is not efficient or the microstructure is not well controlled, the demagnetization curve often shows a two-step reversal behavior, i.e., there is a “kink” in the curve. This method is widely used to inspect the effects of IGEC in the nanocomposite magnets in a simple way. Figure 46(a) shows the demagnetization curves

of the  $\text{SmCo}_5/\alpha\text{-Fe}$  nanocomposites which are ball milled for different time. [256,257] It can be clearly seen that the curves for samples milled less than 2 h have a noticeable kink indicative of a decoupled two-phase magnet. Samples milled longer than 2 h exhibit smooth demagnetization curves, which indicates that a good microstructure is obtained and therefore effective IGEC exists in the nanocomposites. This is understandable if one studies the evolution of the microstructure of the samples. The microscopic studies show that the initially equiaxial  $\alpha\text{-Fe}$  grains in microns became narrow and elongated with increasing milling time, as shown in Figs. 46(b) and 46(c). With further milling, the nanoscale  $\alpha\text{-Fe}$  strips become thinner and break up into isolated equiaxial nanoscale grains, as shown in Fig. 46(d). [256,257] After  $\sim 4$  h of milling, the result was a ho-

mogenously distributed magnetically soft phase particles embedded in the hard-phase matrix with size smaller than 15 nm, which could be effectively exchange-coupled by the magnetically hard  $\text{SmCo}_5$  phase. This is reflected by the demagnetization curve of the sample milled for 4 hours. In addition, if one compares the demagnetization curves of the samples milled for 30 min and 1 hour in Fig. 46(a), it should be noted that the 1 hour milling sample has better magnetic properties than the 30 minutes milling sample, which is reflected by the microstructure modification. The good correlation between the demagnetization behaviors and microstructures indicates this “kink” method is useful in studying the IGEC in nanocomposite materials.

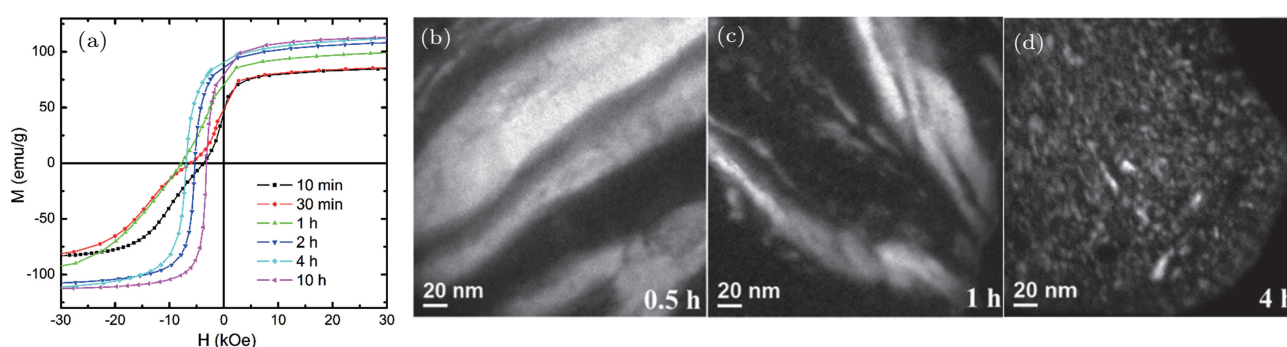


**Fig. 46.** (color online) (a) Demagnetization curves of the composite samples milled for different time; energy-filtered transmission electron microscopy (EFTEM) images of Fe maps for the samples milled for (b) 30 min, (c) 1 h, and (d) 4 h. High Fe-content regions have bright contrast. [256,257]

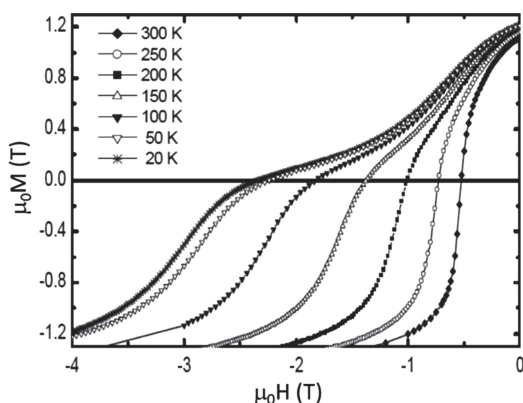


**Fig. 47.** Demagnetization curves at different temperatures of  $\text{Pr}_8\text{Fe}_{87}\text{B}_5$  nanocomposite magnets prepared by melt spinning. [258]

It should be noted that exchange-coupled magnets exhibit a strong temperature dependence of their hysteresis loops. Some nanocomposite magnets may have a smooth hysteresis loops at room temperature, but their low-temperature loops show a two-phase demagnetizing behavior. This could be explained by the reduction of exchange length  $l_{\text{ex}} = \sqrt{A/K}$  as the anisotropy constant increase quickly at low temperatures. Although the grain size of magnetically soft phase does not change, the reduction of exchange length leads to an inefficient exchange coupling at low temperature. Therefore, the low-temperature measurement is also used to identify the IGEC in the magnets. Figure 47 shows the demagnetization

curves at various temperatures of the  $\text{Pr}_8\text{Fe}_{87}\text{B}_5$  nanocomposite magnets prepared by melt spinning. [258] The demagnetization curves behavior like a single-phase magnet at room temperature but a two-phase behavior is observed at low temperatures.

While the method of single-phase magnetic behavior can provide an intuitive information, it only provides qualitative information of the strength of exchange coupling in the magnets. In addition, this method cannot provide good information for single-phase nanocrystalline magnets as there is no kink even there is no exchange coupling.

## 4.2. Remanence enhancement

According to the Stoner–Wohlfarth (SW) model, for an assembly of non-interacting and randomly oriented grains, the ratio of the remanence to the saturation magnetization (normalized remanence) is

$$m_r = \frac{M_r}{M_s} = \frac{\int_0^{2\pi} \int_0^{\pi/2} \sin \theta \cos \theta d\theta d\varphi}{\int_0^{2\pi} \int_0^{\pi/2} d\theta d\varphi} = \frac{1}{2}, \quad (1)$$

where  $\theta$  and  $\varphi$  are the polar and azimuth angles of the magnetic moment to the easy axis of uniaxial particles. However, nanocrystalline isotropic permanent magnets show an enhanced remanence in which the ratio is larger than 0.5, which was observed in experiments 30 years ago, [199] since IGEC

makes the magnetic moments of a grain parallel to the neighboring ones. This behavior is called remanence enhancement.

To quantitatively analyze the effect of IGEC on the normalized remanence, Zhang *et al.* estimated the maximum  $m_r$ , assuming that the mean magnetization direction of each hard grain boundary region is in the middle orientation between easy magnetization axis of the grain and that of its neighboring hard grain, while the magnetization direction of soft grain (such as  $\alpha$ -Fe) is assumed to be in the same mid-way.<sup>[258]</sup> The sum of all such regions for the remanence is

$$m_r = \frac{1}{2\pi} \int_0^{2\pi} d\varphi_2 \left\{ \int_0^{\pi/2} \sin \theta_2 \times \left[ \frac{1}{2\pi} \int_0^{2\pi} d\varphi_1 \left( \int_0^{\pi/2} \sin \theta_1 \cos \theta_0 d\theta_1 \right) \right] \right\}. \quad (2)$$

Here,  $\theta_{1,2}$  and  $\varphi_{1,2}$  are the angles of the easy axes of hard grain 1 and 2, respectively.  $\theta_0$  is the middle direction of easy axes of grain 1 and 2 and expressed as

$$\cos \theta_0 = \frac{\sqrt{2}(\cos \theta_1 + \cos \theta_2)}{2\sqrt{1 + \cos \theta_1 \cos \theta_2 + \sin \theta_1 \sin \theta_2 \cos(\varphi_1 - \varphi_2)}}. \quad (3)$$

The value of  $m_r$  is about 2/3, which is obviously higher than the normalized remanence 1/2 for noninteraction isotropic Stoner–Wohlfarth particle assembly.

Zhao *et al.* studied the remanence enhancement in a grain chain through a more complicated analytical model.<sup>[259]</sup> In this model, the magnetic moments near the grain boundaries point to the directions which gradually change from the easy direction of one grain to that of a neighboring grain, instead of the simple average of two directions of the easy axes, while those in the grain center point to the direction of the easy axis. The two-dimensional analytical model generates a normalized remanence given by

$$m_r = \frac{2}{\pi} \left( 1 + \frac{l_{\text{ex}}}{L} \right), \quad (4)$$

where  $L$  is the length of the studied cubic grain, i.e., equivalent grain size.  $l_{\text{ex}} = \sqrt{A/K}$  is the exchange length. It should be noted that  $\delta_w = \pi l_{\text{ex}}$  is the Bloch wall width for 180° domain wall. For  $\text{Nd}_2\text{Fe}_{14}\text{B}$ , the exchange length and Bloch wall width is 1.34 and  $\sim 4.2$  nm, respectively. With consideration of each cubic grain having six neighboring grains for three-dimensional model, the calculated relation between  $m_r$  and  $l_{\text{ex}}/L$  follows

$$m_r = 0.5 + 1.8 \frac{l_{\text{ex}}}{L}. \quad (5)$$

The constant term on the right-hand side corresponds to the bulk contribution as given by the SW model and the second term reflects the contribution from the grain boundaries due to IGEC.

Rong *et al.* studied the contribution of IGEC on the remanence of the isotropic nanocrystalline magnets using micromagnetic finite element analysis (FEA).<sup>[15]</sup> Figure 48 shows the dependence of  $m_r$  on the grain size of the single-phase nanocrystalline magnets, comparing the FEA, analytical model using Eq. (5), and experimental results. As one can see  $m_r$  increases quickly when the grain size approaches to 10 nm and below. This agrees with the theoretical prediction that the IGEC affects the magnetic moments majorly near the grain boundary within a region of twice of the domain wall, which is about 8.4 nm for  $\text{Nd}_2\text{Fe}_{14}\text{B}$  magnets. It should be noted that the FEA results fit the free-surface experimental results of the melt-spun ribbons quite well. Although it is slightly higher than that of roll-surface results, the trend is similar to that of micromagnetic FEA simulation. The analytical results based on Eq. (5) are similar to the FEA simulation when the grain size is larger than 30 nm. However, the deviation between them increases fast with reducing grain size.

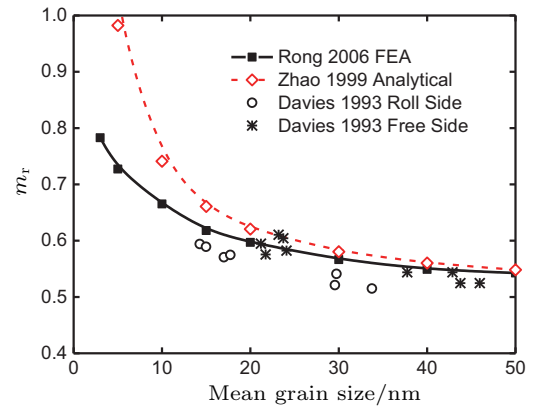


**Fig. 48.** (color online) Dependence of  $m_r$  as a function of grain size in the single-phase nanocrystalline magnet. FEA results are from Ref. [15]; analytical results are based on Eq. (5) from Ref. [259]; experimental results of the roller and free surfaces of the melt-spun  $\text{Nd}_{13.2}\text{Fe}_{79.6}\text{B}_6\text{Si}_{1.2}$  magnets are from Ref. [215].

The analysis of remanence enhancement in the nanocomposites is much more challenge than that in the single-phase nanocrystalline magnets, as the magnetically soft grains are more easily affected by the dipolar interactions comparing to the magnetically hard grains. This complex makes the accurate analysis of remanence enhancement by analytical model almost impossible. On the other hand, micromagnetic FEA simulation could provide a much better estimation on the remanence enhancement.<sup>[15–17,260]</sup> Figure 49 shows the effects of both grain size and soft phase content ( $v_s$ ) on the normalized remanence under two cases, i.e., with and without considering the dipolar interactions in the nanocomposite permanent magnets. Since the anisotropy field of magnetically soft phase is small, the magnetizations in soft grains rotate out of the easy axis easily and are parallel to the easy directions of the neighboring magnetically hard grains owing to the contribution of IGEC. As a result,  $m_r$  should increase with increasing

$v_s$ , which is confirmed in Fig. 49 for all grain sizes if dipolar interaction is not considered. Thus, the addition of soft phase is an important way to obtain the remanence enhancement in nanocomposite magnets. When the dipolar interaction is considered in the micromagnetic FEA simulation, the monotonic relation between  $m_r$  and  $v_s$  for the magnets with grain size smaller than 20 nm is similar to the results neglecting dipolar interactions. This means that IGEC plays a decisive role in the magnets with small grains. However, the above laws are no longer suitable for the magnet with both large grain size and soft-phase content. The  $m_r$  begins to decrease when the soft-phase content is higher than a special value, which decreases with increasing grain size. For example,  $m_r$  is only 0.39 for the magnets with 50 vol%  $\alpha$ -Fe and grain size of 40 nm. This value is lower than the Stoner–Wohlfarth limitation of 1/2. In this situation, the exchange interaction between the soft and hard phases cannot suppress dipolar interaction when both grain size and soft-phase content are too large. That is to say, redundant soft phase is not helpful to improve magnetic properties. In addition, it also proves that both IGEC and dipolar interaction are important in the nanocomposite permanent magnets.

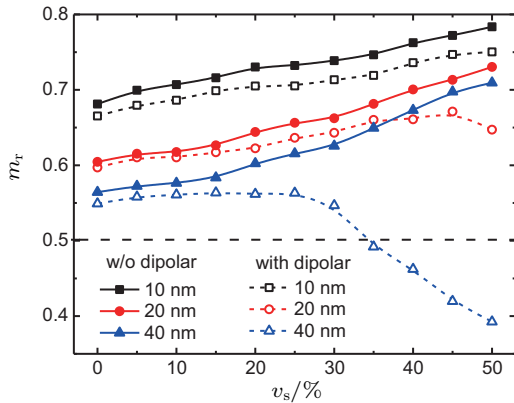


**Fig. 49.** (color online) Calculated  $m_r$  of the isotropic nanocomposite as a function of soft phase content,  $v_s$ , with and without considering the dipolar interactions.<sup>[15]</sup>

### 4.3. Henkel plot

Measurements of remanence are a well-known tool to characterize IGEC in the nanocrystalline magnets by comparison with an ideal Stoner–Wohlfarth (S–W) assembly. The remanence enhancement mentioned in Section 4.2 is only one of the methods which only considers the saturated remanence, i.e., remanence measured after saturating the magnet first. Henkel plot is another useful and popular way to investigate the IGEC inside magnetic materials. In this method, two types of remanence must be measured. One is the magnetizing remanence  $M_r(H)$  which is acquired after the application and subsequent removal of a direct applied field  $H$ . It should be noted that  $M_r(H)$  must be measured from the specially prepared initial zero-magnetization state, such as thermally de-

magnetized. The other is demagnetizing remanence  $M_d(H)$  which is obtained after saturation in one direction and the subsequent application and removal of a demagnetizing field  $H$  in the reverse direction. The relation between  $M_r(H)$  and  $M_d(H)$  is then used to determine IGEC in magnetic materials. For an assembly of small non-interacting particles, Stoner–Wohlfarth theory shows

$$M_d(H) = M_r(\infty) - 2M_r(H), \quad (6)$$

where  $M_r(\infty)$  is the saturated remanence and is denoted as  $M_r$  for convenience in the following. Henkel first proposed that the deviation from this behavior in real systems is caused by the interactions between particles. The expression of a Henkel plot is as follows:

$$\delta m(H) = [M_d(H) - M_r + 2M_r(H)] / M_r. \quad (7)$$

For an S–W system of an assembly of small non-interacting particles,  $\delta m(H)$  is zero in entire range. The positive values of  $\delta m(H)$  are due to the interactions promoting the magnetized state, such as IGEC, while negative values of  $\delta m(H)$  are caused by interaction tending to assist magnetization reversal, such as dipolar interaction.

To describe the reason of the positive value and peak of the  $\delta m(H)$  curve, a system with two grains are considered, assuming that the magnetic reversal field is  $H_0$  for the two identical grains with easy axes are parallel to each other.<sup>[261]</sup> At the initial state, the magnetic moments are on the opposite directions in order to simulate the thermal demagnetized status. As the IGEC favors the parallel magnetic moments in order to reduce the exchange energy, an applied field ( $H_1$ ) smaller than  $H_0$  is then required to align the thermal demagnetized system. When a demagnetizing field is applied, the magnetic moments in both grains will not reverse until the field reaches  $H_0$ , as IGEC does not play a role in the system already having minimum exchange energy. Therefore a  $\delta m(H)$  curve, as shown in Fig. 50, is expected with positive values when the magnetic field is in the range of  $H_1 \leq H \leq H_0$ .

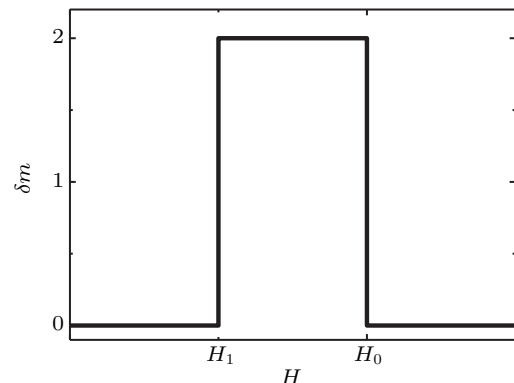


**Fig. 50.**  $\delta m(H)$  curve of a two-grain system.<sup>[261]</sup>

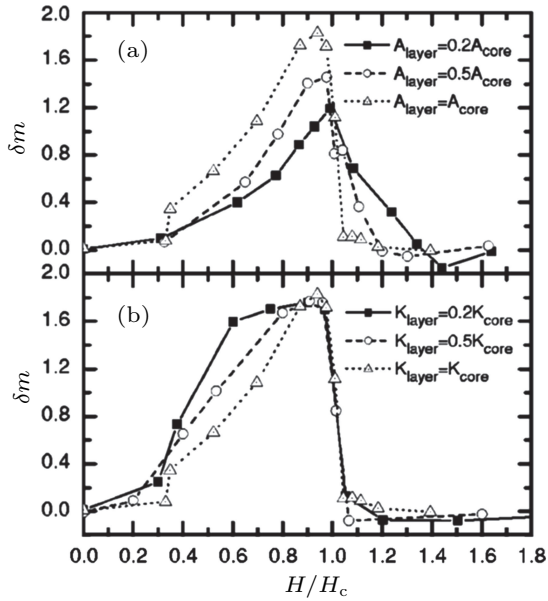


**Fig. 51.** The plots of  $\delta m$  vs.  $H/H_c$  for the variation of (a) exchange constant and (b) anisotropy constant of the grain boundary layer.<sup>[262]</sup>

Zhang *et al.*<sup>[262]</sup> and Rong *et al.*<sup>[261]</sup> studied the dependence of  $\delta m(H)$  on microstructure characteristic of the nanocrystalline and nanocomposite magnet. Figure 51 shows the dependence of  $\delta m$  on the normalized magnetic field ( $H/H_c$ ) for the samples with different layer, i.e.  $A_{\text{layer}}$  and  $K_{\text{layer}}$ , respectively. The plot of  $\delta m$  vs  $H/H_c$  shows a peak and the maximum value of  $\delta m$  is obtained at the field around coercivity, which is consistent with many experimental observations. As shown in Fig. 51, the maximum  $\delta m$  decreases with reducing  $A_{\text{layer}}$ , which means that the  $\delta m$  value could reflect the strength exchange coupling in the magnets between grains. On the other hand, the maximum  $\delta m$  seems to remain unchanged, while the width of the peak is extended to low applied field with the drop of  $K_{\text{layer}}$ , which is caused by the larger  $M_r(H)$  obtained at small applied field for reduced  $K_{\text{layer}}$ . This is understandable as a smaller  $K_{\text{layer}}$  means that the IGEC can affect the magnetic moment easier even the exchange constant is kept same. If we use the two-grain system to explain this behavior, it means the applied field  $H_1$  in Fig. 50 is smaller, and therefore, the  $\delta m$  peak is broadened. The FEA analysis also pointed out that  $m_r$  is 0.65, 0.69, and 0.72 for  $K_{\text{layer}} = 1.0, 0.5,$  and 0.2, respectively. This means that remanence enhancement can result from the decrease of  $K_{\text{layer}}$  only; that is, without the change of  $A_{\text{layer}}$ . Therefore, remanence enhancement is not the best to determine IGEC, while it can be easily examined by Henkel plot. For the nanocomposite magnets, if the magnetically soft phase is completely coupled by the magnetically hard phase, the Henkel plot only show one sharp peak. However, a broadened peak or even two separated peaks appears if the two phases are not well coupled.<sup>[261]</sup>

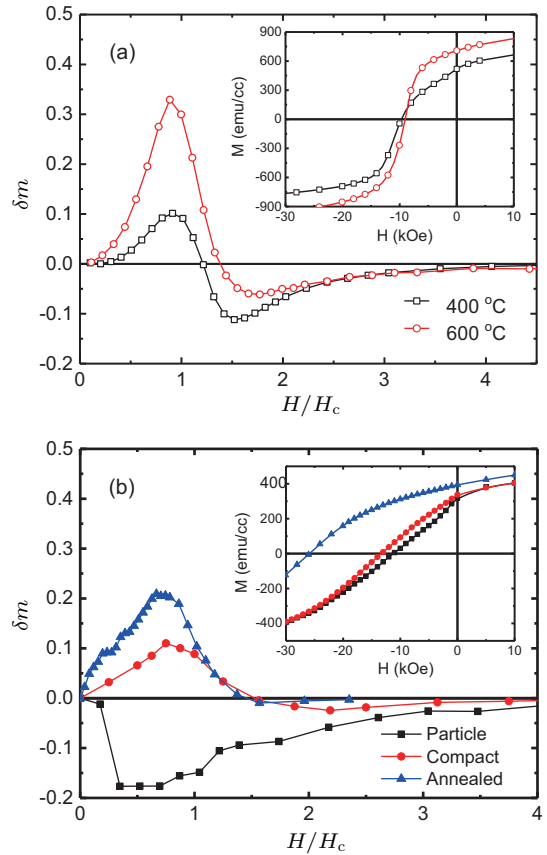


**Fig. 52.** (color online) (a)  $\delta m$  plots of the samples compacted at 400 and 600 °C from the fcc FePt nanoparticles. (b)  $\delta m$  plots of the isolated  $L1_0$  particles and samples compacted under 2.5 GPa at 200 °C as well as the post-annealed samples. The insets are the corresponding demagnetization curves.<sup>[263]</sup>

The effective of Henkel plot could be verified by experiments. Here two examples are given to compare the Henkel plots, normalized remanence, hysteresis loops and therefore to correlate the Henkel plot and IGEC in the nanocomposite magnets.<sup>[263]</sup> Figure 52(a) compares the  $\delta m$  plots of the 400 and 600 °C compacted FePt/Fe<sub>3</sub>Pt samples prepared from the face-centered-cubic (fcc) nanoparticles. The  $\delta m$  value for the 600 °C compacted sample with higher density is positive and much higher than that for the 400 °C compacted sample with lower density. This indicates the stronger exchange coupling in the denser compact compared to the looser compact. The stronger IGEC is reflected by the shape of the demagnetization curves, as shown in the inset of Fig. 52(a). The denser compact has a smoother demagnetization curve and better squareness. In addition, the normalized remanence (0.63) of the 600 °C compacted sample is higher than that of 400 °C compacted (0.58), which is also consistent with the  $\delta m$  measurement. This  $\delta m$  effect is even more pronounced for the  $L1_0$  particle samples. Figure 52(b) compares the Henkel plots for 15 nm  $L1_0$  FePt nanoparticles and their compacts. Here the FePt nanoparticles are prepared by the salt-assisted annealing method which ensures that the nanoparticles are isolated

after annealing but the fcc structure is transferred to face-centered-tetragonal (fct) structure.<sup>[264]</sup> It was found that the  $\delta m$  of the nanoparticles before compaction is a large negative value. This is because of the fact that only dipolar interaction but no IGEC exists between the particles. After the compaction at 2.5 GPa and 200 °C,  $\delta m$  changed its sign to positive, indicating the exchange interaction between the particles. Annealing of the compact at 1000 °C for 1 h led to further increase in  $\delta m$  value and thus an enhancement of the exchange coupling. As the annealing causes almost no obvious grain growth, the strong increase in  $\delta m$  can be attributed to improvement in interface conditions upon the high-temperature annealing. The inset in Fig. 52(b) shows the hysteresis loops of the  $L1_0$  nanoparticles and its compacts. It shows that the enhanced exchange coupling significantly improves the squareness of the hysteresis loops. The remanence of the separated nanoparticles, 200 °C compacted sample and 1000 °C annealed sample are 0.50, 0.54, and 0.63, respectively. This agrees with the conclusion from the Henkel plots.

#### 4.4. Recoil loop

The recoil loops represent the variations of working points in the application of permanent magnets, such as in a permanent magnet motor or generator. The enclosed area of the recoil loop means energy loss after one cycle. This energy is typically very small in sintered magnets. From the point view of material research, the recoil loops are measured by removing and re-applying a demagnetizing field to a magnetic material, as the demagnetizing field is increased successively. Recently researchers found that the recoil loops are quite open for nanocrystalline magnets, especially for nanocomposite magnets. Therefore, the recoil loop measurements are also often used to characterize the IGEC in nanocrystalline magnetic materials.

Physically, the open recoil loops can be composed of a time-dependent component and a time-independent one. The time-dependent component is contributed by magnetic viscosity, i.e., thermal relaxation/fluctuation. The time-independent component is majorly contributed from the IGEC, especially for the single-phase nanocrystalline magnets as the energy barrier for the magnetic reversal in the magnetically hard phase is quite large. Both components are discussed below.

Rong *et al.* studied the effect of thermal fluctuation on the recoil openness of an exchange-coupled FePt/Fe<sub>3</sub>Pt nanocomposite system with well-defined magnetically hard/soft two-phase morphology, which was prepared by reducing reaction of chemically synthesized FePt/Fe<sub>3</sub>O<sub>4</sub> bimagnetic nanoparticles.<sup>[265]</sup> TEM analysis shows that the grain size of

650 °C annealed sample is only 8–13 nm, while serious grain growth was observed in the 800 °C annealed sample. In addition, both magnetically hard  $L1_0$ -FePt phase and magnetically soft phase Fe<sub>3</sub>Pt exist in the 650 °C annealed sample, while only single phase  $L1_0$ -FePt is found in the 800 °C annealed sample. XRD analysis confirms that the volume fraction of the Fe<sub>3</sub>Pt phase decreases from  $28 \pm 3\%$  to  $8 \pm 2\%$  with increasing annealing temperature from 500 to 650 °C. The recoil loops were then measured with different sweep rate ( $\eta$ ) of applied magnetic field from  $\eta = \eta_0$  to  $\eta = 10^{-4}\eta_0$ , where  $\eta_0$  is the limit of sweep rate of the instrument. Figure 53 compares the major and recoil loops of the 550 and 800 °C annealed samples with  $\eta = \eta_0$  and  $\eta = 10^{-4}\eta_0$ . Open recoil loops were observed for both samples. However, the open areas of the 550 °C annealed sample are larger than that of the 800 °C annealed sample. More interestingly, the open areas of the fast measurements are larger than those of the slow ones for the 550 °C annealed sample, indicating that the openness of the recoil loops is related to the field sweep rate.

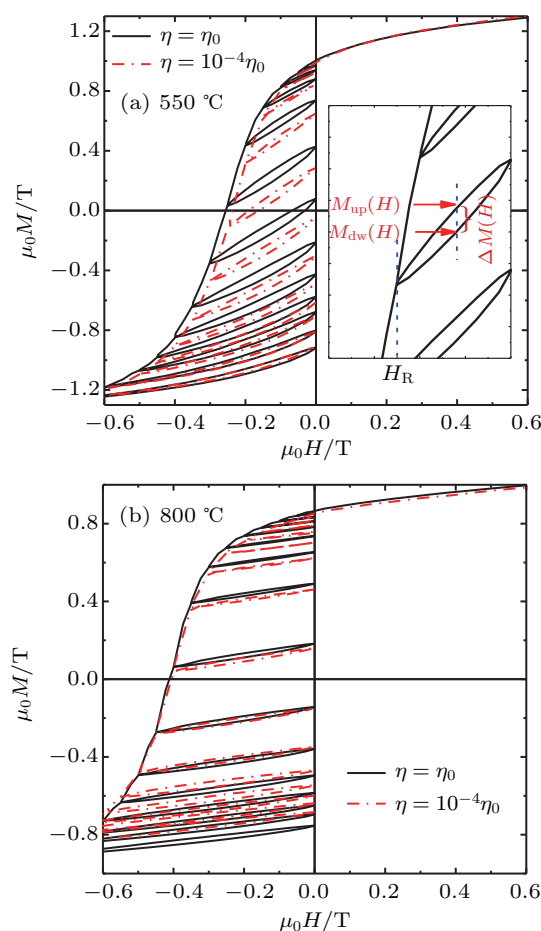


**Fig. 53.** (color online) Recoil loops of the (a) 550 and (b) 800 °C annealed samples with different sweep rates: (black)  $\eta = \eta_0$  and (red)  $\eta = 10^{-4}\eta_0$ . The inset defines  $M_{\text{up}}(H)$ ,  $M_{\text{dw}}(H)$ , and  $\Delta M_{\text{rc}}(H)$ , which are the magnetizations of the upper and lower branches, and their difference, respectively. The maximum normalized recoil loop openness in each recoil loop was then defined as  $\Delta m_{\text{rc}}^{\text{m}}(H_{\text{R}})$ , where  $H_{\text{R}}$  is the applied reversal field.<sup>[265]</sup>

To analyze the relation between the recoil loop openness and the thermal fluctuation quantitatively, two different methods were used to measure the activation volume, i.e., the sweep-rate dependence of the coercivity, and magnetic viscosity measurements. The activation volumes obtained by these two methods are quite similar. Figure 54(a) shows the dependence of normalized coercivity  $H_c(\eta)/H_c(\eta_0)$  on the sweep rate of the applied field as an example. It was found that the coercivity decreases fast with decreasing  $\eta$  for the low-temperature annealed samples while slowly for the high temperature annealed samples. The inset of Fig. 54(a) gives the dependence of the slope, i.e.,  $k_B T/V_{ac} H_c$ , on the annealing temperature, where  $k_B$  and  $V_{ac}$  are the Boltzmann constant and activation volume, respectively. One can see that  $k_B T/V_{ac} H_c$  decreases fast when annealing temperature is lower than 650 °C and slowly when annealing temperature is higher than 650 °C. Figure 54(b) shows the dependence of the maximum openness of the recoil loops on  $k_B T/V_{ac} H_c$  for different sweep rates of the applied field. The square and circle symbols represent the data of the samples annealed at 500–800 °C for  $\eta = \eta_0$  and  $\eta = 10^{-4} \eta_0$ , respectively. It was found that maximum openness of the recoil loops increases with the increase of  $k_B T/V_{ac} H_c$ . In addition, a rough linear relation between the recoil loop openness and  $k_B T/V_{ac} H_c$  was also observed. To confirm this correlation, the 550, 650, and 800 °C annealed samples were measured by a superconducting quantum interference device (SQUID) magnetometer at temperatures ranging from 5 to 390 K. It was found that the fitting line is consistent with the SQUID measured data as well. It should be noted that similar conclusion is also made in the  $\text{SmCo}_5/\alpha\text{-Fe}$  nanocomposite magnets.<sup>[266]</sup>

The correlation between the recoil loop openness and thermal fluctuation can be understood as follows: in a hard/soft nanocomposite, the magnetic moments in the soft phase are exchange coupled by the magnetically hard grains, while they tend to be unstable under a moderate reverse field and are easy to thermally reverse, especially for those in the center of soft grains due to the lower energy barrier compared to those near the hard phase.<sup>[15]</sup> The unstable moments are then affected sensitively by thermal fluctuation and contribute to the large openness in the recoil loops of the nanocomposite magnets. Larger openness is normally observed in the recoil loops of nanocomposite magnets compared with single-phase magnets since the magnetic moments in the soft phase of nanocomposites are more unstable than those in grain boundary regions in single-phase hard magnets.

While thermal fluctuation does contribute to the recoil loop openness as discussed above, it is not the only major factor, as one still see the open recoil loop in single-phase nanocrystalline magnets. Here the micromagnetic FEA simulation is used to investigate the origin of recoil loop open-

ness in exchange-coupled nanocrystalline magnets where the thermal fluctuation is not considered.<sup>[267]</sup> An isotropic single-phase magnet was constructed by assembling of 64 cubic  $\text{Nd}_2\text{Fe}_{14}\text{B}$  grains with random orientation, as shown in the inset of Fig. 55(a). A hard-soft phase nanocomposite magnet was constructed by filling the magnetically soft  $\alpha\text{-Fe}$  phase into the space between the  $\text{Nd}_2\text{Fe}_{14}\text{B}$  hard-phase grains, as shown in the inset of Fig. 55(b). The size ( $L$ ) of the  $\text{Nd}_2\text{Fe}_{14}\text{B}$  grains varies from 10 to 50 nm, while the thickness of the  $\alpha\text{-Fe}$  layers ( $t$ ) varies from 0 to 6 nm.

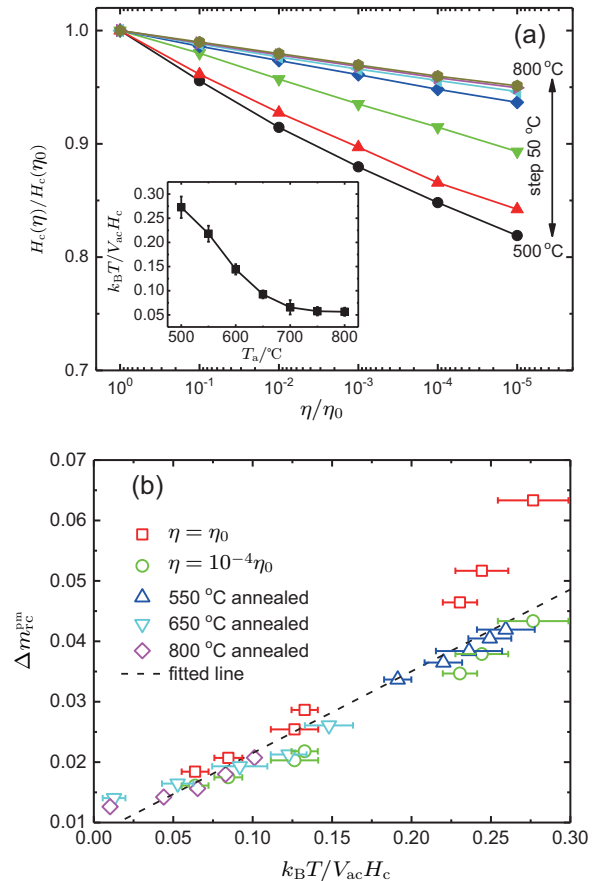


**Fig. 54.** (color online) (a) The dependence of coercivity on sweep rate for different samples. The inset gives the dependence of  $k_B T/V_{ac} H_c$  on the annealing temperature. (b) The dependence of recoil loop openness on  $k_B T/V_{ac} H_c$  for different samples and different sweep rates.<sup>[265]</sup>

Figure 55 compares the simulated recoil loops of the single-phase ( $L = 20$  nm) and the nanocomposite ( $L = 20$  nm and  $t = 3$  nm) samples. It is observed that the recoil loops of a single-phase magnet are also open, though the openness of the simulated nanocomposite magnet is larger than that of a single-phase sample. Figures 56(a) and 56(b) show the dependence of the recoil loop openness of the single-phase with different grain size and nanocomposite samples with different soft-phase layer thickness, respectively. Interestingly, it has been observed that the recoil loop openness increases with decreasing grain size, confirming that the intergranular exchange-coupling interactions in single-phase magnets also play an important role in the occurrence of open recoil loops.

For the nanocomposite magnets, the recoil loop openness increases with increasing soft-phase thickness (soft-phase content), which confirms that the soft phase contributes to the open recoil loops. In addition, the absolute openness of the

nanocomposite is much larger than the single-phase magnet, further confirming that the magnetically soft phase has more significant contribution to the openness comparing to magnetically hard phase.

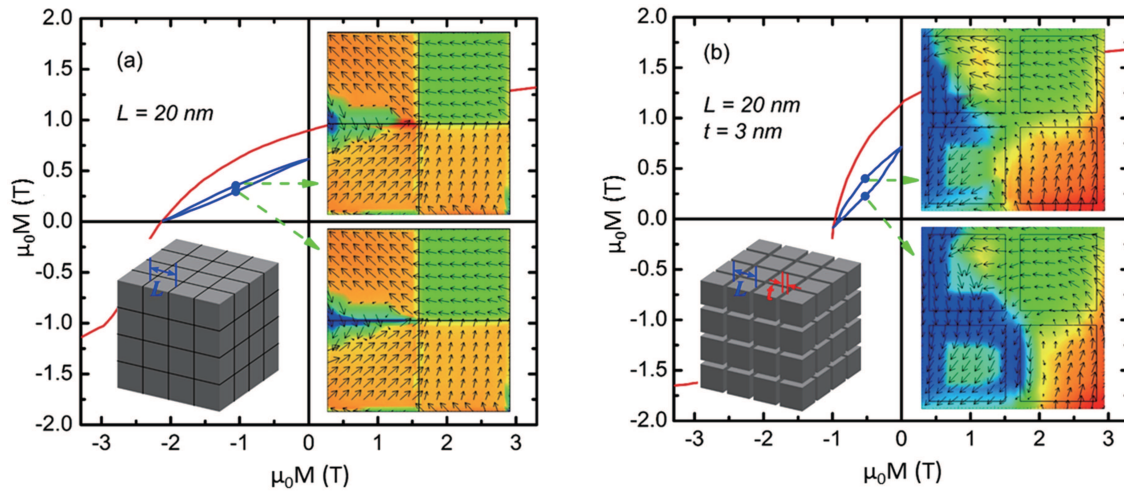


**Fig. 55.** (color online) The recoil loops with maximum openness of (a) the single-phase magnet with  $L = 20$  nm and (b) the nanocomposite magnet with  $L = 20$  nm and  $t = 3$  nm. The insets shown in the third quadrant are the 3D model of single-phase and hard-soft phase nanocomposite magnets. The insets in the right side give the magnetization distributions at different magnetic history, i.e., upper and lower branches of recoil loop under field  $H = H_R/2$ . The color red and blue in the distributions represent the magnetic moments with deviation to up and down, respectively. To illustrate the magnetization distributions clearly, the slice plane of only four grains was selected instead of the whole sample.<sup>[267]</sup>

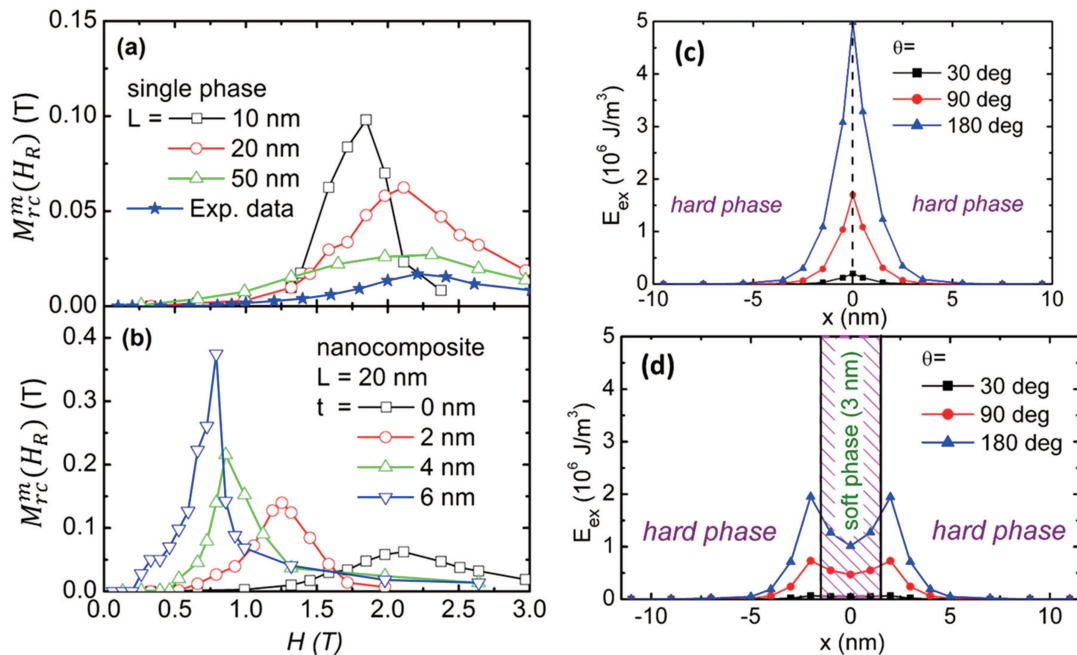


**Fig. 56.** (color online) The dependence of  $M_{TC}^m(H_R)$  on the maximum reversal field  $H_R$  for (a) the single-phase magnets with different grain size and (b) the nanocomposite magnets with different soft-phase layer thickness while keeping  $L = 20$  nm. The exchange energy distribution along (c) two adjacent hard grains for the single-phase magnet and (d) two adjacent hard grains through the soft-phase layer for the nanocomposite magnet.  $\theta$  is the angle between two easy-axis directions of the adjacent magnetically hard grains.<sup>[267]</sup>

Since the intergrain exchange coupling either between the grains in the same phase or different phases always leads to the deviation of magnetic moments in grain boundary regions from easy-axis directions of the grains in order to reduce the exchange energy and thus system Gibbs free energy, it is natural to assume that the exchange energy distribution over a

nanocrystalline is related to the origin of open recoil loops. Figures 56(c) and 56(d) show the exchange energy distribution along two adjacent hard-phase grains in a single-phase magnet and along the soft-phase layer in a nanocomposite magnet. It is found that the exchange energy increases very fast when approaching a grain boundary for both single-phase and

nanocomposite magnets, especially when two adjacent grains have large angle between two easy-axis directions. Surprisingly, the increase is much dramatic in case of single-phase magnets. It is not difficult to imagine that the high local exchange energy in grain boundary regions makes the magnetization configuration unstable.

The origin of an open recoil loop can be better understood by comparing the magnetization distributions in the single-phase and nanocomposite magnets, as shown in the insets of Fig. 55. First, the unstable magnetic moments in the grain boundary and soft-phase regions reverse under an applied relatively large external field. These magnetic moments keep reversed with removing external field unless the external field is small enough or is totally removed (lower branch of recoil loops). The unstable magnetic moments are now exchange-coupled with those in the adjacent hard grains if the external is removed. They will not reverse easily by reapplying a small external field (upper branch of recoil loops). Thus, an open recoil loop is formed owing to the irreversible magnetic moments in the grain boundary and in the soft-phase regions. The irreversible magnetization behavior is in turn due to the competition of exchange coupling between the adjacent hard grains which have large deviation angle between the stable magnetic moments in each grain core. Therefore, the more adjacent hard grains with large deviation angle are, the larger the recoil loop openness will be. This explains why the largest openness is always taking place when the applied reverse field is around the coercive field. It is also important to mention that the magnetic moments in the soft phase may be more unstable by nature since the magnetocrystalline anisotropy of soft phase is much lower than that of hard phase even the exchange energy in the soft-phase region is lower than that in grain boundary region in single-phase hard magnets.

In summary, the open recoil loops in the nanocrystalline and nanocomposite magnets are majorly caused by the IGEC and thermal fluctuation. Zheng *et al.* reported similar micro-magnetic simulation and also attributed the open recoil loop to the strong intergrain exchange coupling, which results in the magnetization reversal in some hard grains during the recoil processes.<sup>[268]</sup> The chance of the magnetization reversal in magnetically soft grains is larger, leading to a larger of recoil loops of the nanocomposite magnets. On the other hand, Li *et al.* confirmed the dependence of recoil loop openness on the sweep rate of magnetic field, the correlation between the recoil loop openness, activation volume and reversible susceptibility.<sup>[269]</sup>

#### 4.5. First-order reversal curve

Although the magnetic characterization of materials is usually made by measuring a hysteresis loop, it is not pos-

sible to obtain information of interactions or coercivity distributions from the hysteresis loop solely. First-order-reversal-curves (FORC) provide insight into the relative proportions of reversible and irreversible components of the magnetization of a material. In addition, the magnetostatic and exchange interactions between the magnetically hard and soft phases can be mapped using FORC diagrams for the exchange-coupled magnets. An FORC measurement begins by saturating the samples with a large positive applied field. The field is decreased to a reversal field, and then the FORC is defined as the magnetization curve measured with increasing applied field back to saturation. The measurement procedure is repeated for different values of reversal fields to obtain a suite of FORCs and a two-dimensional distribution function. The FORC diagram is defined as the mixed second derivative of the applied field and the reversal field. A detailed description of FORC distribution can be found in Refs. [270] and [271].

Rong *et al.* studied the correlation between FORC diagrams and the microstructure of the  $\text{SmCo}_5/\alpha\text{-Fe}$  nanocomposites,<sup>[272]</sup> which are the same samples shown in Fig. 46. The microstructures given in Fig. 46(b) show how the magnetically soft phase gradually distributed into the magnetically hard phase matrix through the ball milling process. The grain size of  $\text{SmCo}_5$  and  $\alpha\text{-Fe}$  phases are only about 12 nm for the annealed powders after milling for 240 minutes and after annealing, which is very close to the critical dimension of effective exchange coupling. Without grain size reduction through sufficient ball milling, the soft magnetic phase would be too large to effective exchange coupling, such as in samples milled for 30 and 60 minutes. Figure 57 shows the 2D and 3D FORC diagrams of the powders milled for 30, 60, and 240 minutes after annealing.<sup>[272]</sup> The FORC diagrams of the mixture without milling are also given for comparison. The FORC distribution of the samples and its correlation with the microstructure are summarized below.

(i) There is only one major peak around the origin for the un-milled sample since both the raw  $\alpha\text{-Fe}$  and  $\text{SmCo}_5$  powders have near zero coercivity. No useful information could be detected for this case.

(ii) Ball milling reduces the grain size while post-annealing restores the crystallinity for the  $\text{SmCo}_5$  phase, which in turn raises the coercivity. As a result, there are two completely separated peaks along the bias axis for the sample milled for 30 minutes, one near origin and one near 15 kOe, which represent the magnetization reversals of the magnetically soft and hard phases, respectively. The separated magnetization reversal indicates weak exchange interaction between the two magnetic phases. A distinct ridge is observed at an angle of  $\sim 135^\circ$  across the lower half of the FORC diagram, which could be attributed to the magnetostatic interaction be-

tween the magnetically soft and hard phases.

(iii) The two peaks along the bias axis merge when milling time is increased to 60 minutes, which is attributed to the grain refinement of  $\alpha$ -Fe phase. The magnetic moments in the  $\alpha$ -Fe grains are partially exchange-coupled and thus the switching field of the magnetically soft phase increases.

However, a large amount of  $\alpha$ -Fe phase is still in a form of strips and not exchanged coupled, therefore there is still a strong peak around the origin in the FORC diagram. The ridge around  $\sim 135^\circ$  becomes weak with increasing milling time since the exchange interaction starts to dominate the magnetization behavior with grain refinement.

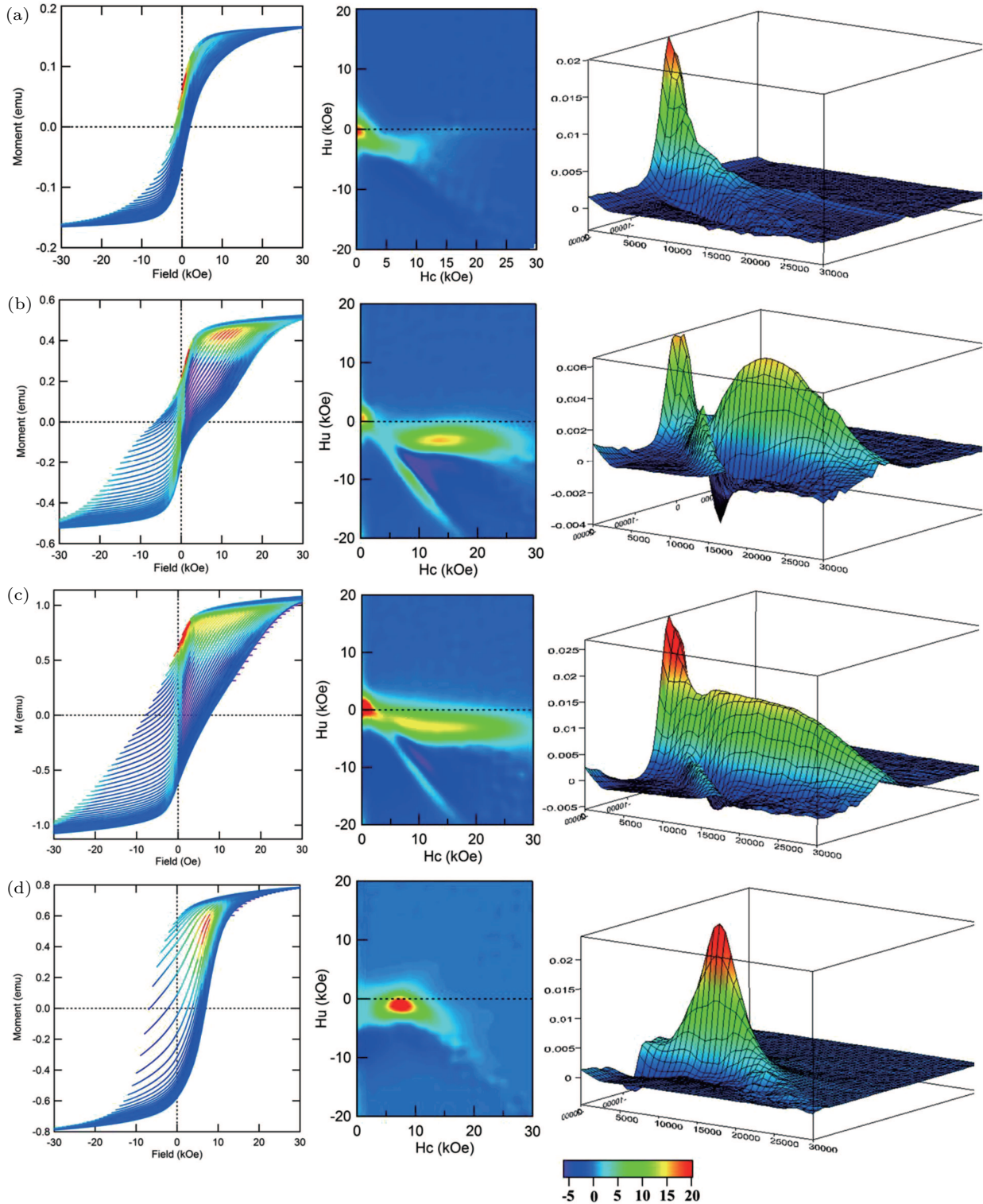


**Fig. 57.** (color online) The 2D and 3D FORC diagrams of the samples (a) without milling, and milled for (b) 30, (c) 60, and (d) 240 minutes after annealing at 525 °C for 30 minutes. Left column is the colored FORC curves with the FORC distribution plotted inside the hysteresis loop. The middle column is the 2D FORC diagrams and right column is 3D FORC diagrams.<sup>[272]</sup>

(iv) Extending milling time leads to further grain refinement and homogeneously distributed  $\alpha$ -Fe grains are obtained when the milling time is longer than 4 hours. The soft phase is completely exchange-coupled and thus there is only one major peak in the FORC diagram around  $\mu_0 H_c = 0.8$  T. The magnetic reversal happens simultaneously in both hard and soft magnetic phases, i.e., a single-phase magnetization reversal behavior is observed in the nanocomposite SmCo<sub>5</sub>/Fe system with homogeneously distributed magnetically soft phase.

Based on the analysis of FORC diagrams and microstructures, it is found that FORC can provide deeper information on the magnetic interactions inside of exchange-coupled magnets than the simple hysteresis loop, remanence enhancement and even Henkel plot, although the measurements of FORC diagram is usually time-consuming.

#### 4.6. Coercivity and microstructure parameters

Coercivity is one of the most important extrinsic parameters that characterizes permanent magnets, since it reflects the ability of the magnet to resist magnetization reversal under the application of an external field. For conventional sintered magnets, the coercivity mechanisms are dominant by either nucleation-type or domain-wall pinning-type. In nucleation-type magnets, such as Nd<sub>2</sub>Fe<sub>14</sub>B, SmCo<sub>5</sub>, or hard ferrite sintered magnets, the magnetic domain walls can move easily within the grains, so that the magnetization increases steeply even in small magnetizing fields for a thermal demagnetized magnet. However, a large demagnetizing field is required in order to form the nuclei of reversed domain in every saturated grain during demagnetizing process. In pinning-type magnets, the magnetic domain walls are pinned at phase boundaries, precipitates, or planar crystal defects, for instance, in Sm(CoCuFeZr)<sub>z</sub> sintered magnets. In order to saturate or demagnetize a pinning-type magnet, the domain walls must be removed from the pinning sites, which requires magnetizing fields larger than the pinning field strength. Therefore, a large magnetic field has to be applied in order to overcome the pinning force for both magnetizing and demagnetizing processes. The initial or virgin magnetizing curve of a magnetic material from the thermally demagnetized state indicates which coercivity mechanism prevails, as shown in Fig. 58. As one can see that the pinning-type magnet requires a field at least twice of the coercive field in order to fully saturate the magnet, while the nucleation-type magnet only needs a much smaller field, although a field strength of twice the saturated magnetization is still required to gain a perfect saturation technically.<sup>[273]</sup> Besides the virgin magnetizing curve, there are several methods could be used to identify the coercivity mechanism including the shape of minor hysteresis loop,<sup>[273]</sup> coercivity, and/or remanence of minor hysteresis loops as a function of applied field,<sup>[274–277]</sup> angular dependence of coercivity.<sup>[253,278,279]</sup> Unfortunately, these methods are not very effective to identify the

coercivity mechanism for nanocrystalline magnets especially for nanocomposite magnets. Since the melt-spun magnets are typically isotropic instead of anisotropic, probably only those grains whose easy axes are aligned parallel to the magnetizing field strength are easily saturated, whereas in all other grains the polarization must be rotated parallel to the magnetizing field. The rotation of the magnetization against the magnetocrystalline fields requires strong magnetizing fields. Therefore, there is only a flat increase in the magnetization from the thermally demagnetized state, while it does not mean the coercivity of the magnet is controlled by domain-wall pinning. On the other hand, the melt-spun magnets usually have a grain size at nanoscale, which is far smaller than the single domain size of about hundreds of nanometers. This means that each domain has multi-grains, therefore the grain boundaries and the intergrain exchange coupling affects the coercivity mechanism. In fact, the coercivity mechanism in most nanocrystalline and nanocomposite is a mixture of nucleation and domain-wall pinning.

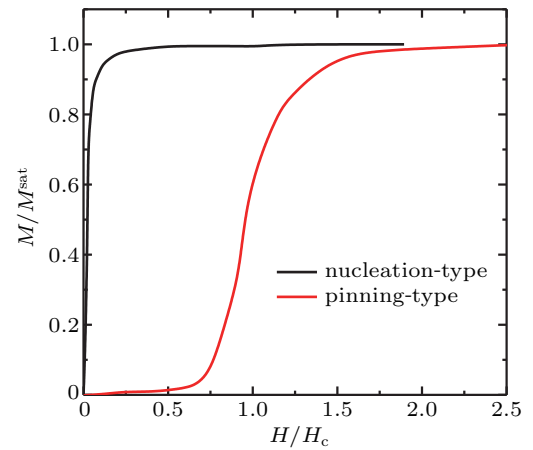


Fig. 58. (color online) Virgin magnetizing curves of typical nucleation-type and pinning-type sintered permanent magnets.

The general equation that proved to be applicable to a vast majority of hard-magnetic materials presents the coercivity as

$$H_c = \alpha H_A - N_{\text{eff}} M_s, \quad (8)$$

where the parameters  $\alpha$  and  $N_{\text{eff}}$  describe the effects of microstructure (including grain size, phase distribution, etc.) and the local stray fields (which are also dependent on the microstructure), respectively.  $H_A$  is the anisotropy field of the material, which can be expressed as  $H_A = 2K_1/\mu_0 M_s$ . The parameter  $\alpha$  can be written in the form  $\alpha = \alpha_k \times \alpha_\phi$ , where  $\alpha_k$  depends on the nature and size of the defect regions in which nucleation or pinning takes place, and  $\alpha_\phi$  takes account of the misalignment of the grains in the magnet. The discussions of how the defects and misalignment affect these two parameters have been discussed for sintered magnets in Refs. [280] and [281]. For typical isotropic ribbons, there is a rather good approximation  $\alpha_\phi$  for  $\phi = 45^\circ$ ; that is,  $\alpha_\phi = 0.5$ . However,

these parameters do not consider the effects of IGEC on the coercivity while IGEC may force magnetization deviation somewhat from the local easy axis, leading to decrease of effective anisotropy and coercivity. Zhang *et al.* proposed a coercivity formula for nanocrystalline magnets as follows:<sup>[282]</sup>

$$H_c = \frac{\alpha_k \alpha_\phi}{1 + \frac{6\beta_k l_{ex}}{d}} H_A - \frac{N_{eff}}{1 + \frac{6\beta_s l_{ex}}{d}} M_s, \quad (9)$$

where  $l_{ex}$  is the ferromagnetic exchange length,  $d$  is the grain size,  $\beta_k$  and  $\beta_s$  depend on the nature of the grains boundary concerning anisotropy field and stray field, respectively. Both the values of  $\beta_k$  and  $\beta_s$  are less than 1. As  $6l_{ex}/d \ll 1$ , the above equation can be expressed in the form of Eq. (8). As for the nanocomposite magnets, it is suggested that  $\beta_k = \beta_s = 1$ , due to the good exchange coupling between the hard and soft phases. In addition, as the demagnetizing behavior of the soft phase is similar to that of a mechanical spring in the nanocomposite magnet,  $l_{ex}/d$  can be approximately changed to the following expression if the magnetic soft phase is small enough which can be efficiently exchange coupled<sup>[283]</sup>

$$\frac{l_{ex}}{d} = \frac{l_{ex}^h + d_s}{2d_s + 2d_h}. \quad (10)$$

Equation (9) can be used to explain the dependence of coercivity on grain size. Figure 59 compares the normalized coercivity ( $H_c/H_A$ ) as a function of grain size for the FEA simulations<sup>[15]</sup> and their fitted curves using Eq. (9). Assuming the  $N_{eff}$  term is zero, the fitted microstructure parameter  $\alpha = \alpha_k \alpha_\phi$  is 0.297 and 0.186 for single-phase and nanocomposite magnets, respectively. As one can see that the FEA simulated and Eq. (9) predicted coercivities agree quite well. The small discrepancy between them may be attributed to the ignorance of  $N_{eff}$  term. It should be noted that the nanocomposite magnet does not give good fitting results using Eq. (10) because the magnetically soft grains cannot be well exchange coupled when the grain size is too large.

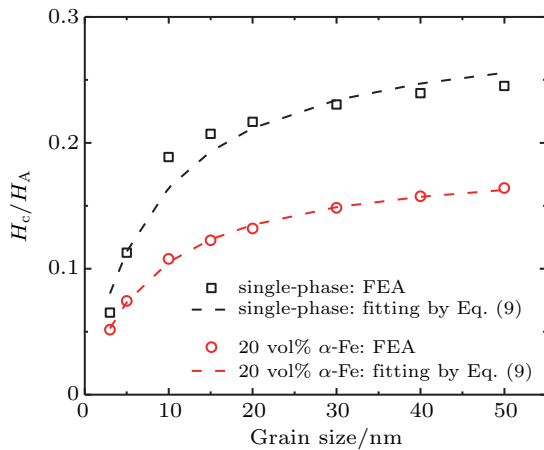


**Fig. 59.** (color online) Normalized coercivity ( $H_c/H_A$ ) as a function of grain size. The scattered squares and circles are the FEA simulation data<sup>[15]</sup> for single-phase and 20 vol%  $\alpha$ -Fe nanocomposite. The dashed lines are the fitting curves using Eq. (9).

#### 4.7. Reversible and irreversible magnetization

Magnetization reversal includes reversible and irreversible processes in nature. Irreversible processes are characterized by a free energy barrier which can only be overcome by increasing the applied field or through thermal activation. Reversible magnetization processes, on the other hand, do not require a critical field for initiation. The reversible magnetization is back to its original status after the applied field is removed. The reversible susceptibility can be determined at any point along a magnetization curve by the measurement of a minor loop associated with a small reversing field increment,  $\Delta H$ . The slope of the minor loop,  $\Delta M/\Delta H$  is defined as the incremental susceptibility and, in the limit of  $\Delta H \rightarrow 0$ , is equal to the reversible susceptibility  $\chi_{rev}$ .<sup>[284]</sup>

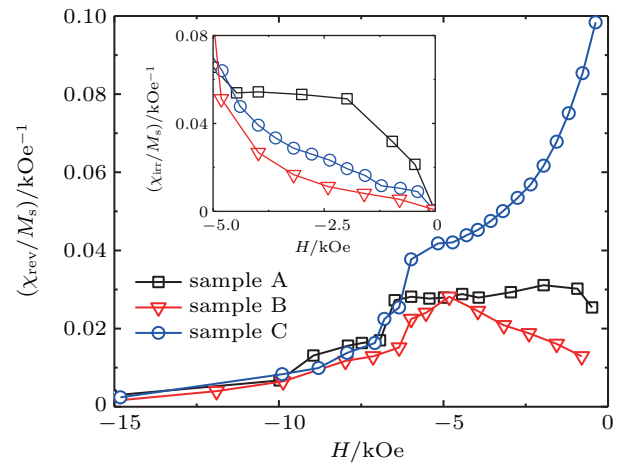


**Fig. 60.** (color online) The reversible susceptibility  $\chi_{rev}/M_s$  vs the applied field at room temperature for the  $\text{Pr}_9\text{Fe}_{85.5}\text{B}_{5.5}$  nanocomposite ribbons melt-spun at (A) 20.5, (B) 21.5, and (C) 23 m/s. The inset shows irreversible susceptibility  $\chi_{irr}/M_s$  vs the applied field.<sup>[285]</sup>

In nanocomposite magnets, reversible magnetization mainly originates from the effect of exchange coupling especially in the magnetically soft component, and irreversible magnetization results from magnetization reversal in magnetically hard grains. Therefore, the reversible or irreversible susceptibilities can be used to investigate the intergrain exchange coupling. Li *et al.* compares the reversible and irreversible susceptibilities of the under-quenched, optimal and over-quenched nanocomposite  $\text{Pr}_9\text{Fe}_{85.5}\text{B}_{5.5}$  magnets which are melt-spun at 20.5, 21.5, and 23 m/s, respectively.<sup>[285]</sup> The grain size of  $\text{Pr}_2\text{Fe}_{14}\text{B}$  is 21.9, 17.5, and 16.8 nm and that of  $\alpha$ -Fe is 18.7, 16.4, and 15.3 nm, respectively. Figure 60 compares the  $\chi_{rev}/M_s$  and  $\chi_{irr}/M_s$  versus applied field for all the three samples. For the over-quenched sample, the magnetization is most reversible at low applied field, suggesting the existence of exchange coupling. For the under-quenched sample, the magnetization is more reversible than that of optimal-quenched sample at low demagnetizing field, which should be attributed to the exchange coupling between soft-hard grains. However, the irreversible magnetization is the most dominant

at low demagnetizing field for the under-quenched sample, indicating a weak resistance against magnetization reversal in some magnetically hard grains and the decoupled effect between hard-hard grains, although the magnetically soft grains are still coupled with the hard grains. With these  $\chi_{\text{rev}} \sim H$  curves, the demagnetization process in the nanocomposite is clear.

The relationship between reversible and irreversible magnetizations can be used to distinguish the magnetic hardening mechanism of permanent magnets, which was proposed and applied to both  $\text{Sm}(\text{CoCuFeZr})_z$  and  $\text{NdFeB}$  magnets by Crew *et al.* [286–288] Rong *et al.* applied this method to analyze the coercivity mechanism of the  $\text{Sm}(\text{CoCuFeZr})_z$  melt-spun ribbons. [289,290] Figure 61 shows the normalized reversible magnetization  $m_{\text{rev}} (= M_{\text{rev}}/M_r)$  versus normalized irreversible magnetization  $m_{\text{irr}} (= M_{\text{irr}}/M_r)$  of the melt-spun  $\text{Sm}(\text{CoCuFeZr})_{6.5}$  ribbons at different temperatures. The curves display a behavior characteristic of domain wall pinning at temperature below 527 °C. At low field,  $m_{\text{rev}}$ , which is proportional to the amount of domain-wall bowing, increases due to the fast increases of the domain walls nucleate and the domain-wall area. After a certain stage in reversal, the total area of domain walls reaches a maximum and  $m_{\text{rev}}$  decreases as reversal proceeds further. Thus,  $m_{\text{rev}}$  versus  $m_{\text{irr}}$  curves exhibit a minimum and are very similar to the results of Crew *et al.* [288] It is interesting to note that the value of the minimum  $m_{\text{rev}}$  decreases with the increase of temperature. This means that the pinning field in the  $\text{Sm}(\text{CoCuFeZr})_{6.5}$  magnets weakens with elevating temperature. By further increasing the temperature above 527 °C,  $m_{\text{rev}}$  decreases linearly with increasing  $m_{\text{irr}}$ . This suggests that the reversal mechanism at high temperature is primarily associated with nucleation, and domain walls play a negligible role in the reversible magnetization component. The results successfully identified the transition of coercivity mechanism from low temperature to high temperature.

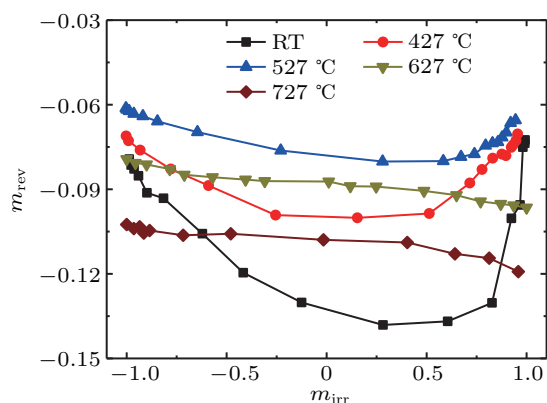


Fig. 61. (color online)  $m_{\text{rev}}$  vs.  $m_{\text{irr}}$  of  $\text{Sm}(\text{CoCuFeZr})_{6.5}$  melt-spun ribbons at different temperatures. [289,290]

## 5. Summary and outlook

The developments of single-phase nanocrystalline and nanocomposite magnets prepared by melt spinning technique have been reviewed in this article. Although partially crystallographic texture can be developed in the melt-spun ribbons with special controls on the process and composition, most nanocrystalline and nanocomposite are isotropic, which limits the energy product to  $\sim 25$  MGOe. While the concept of exchange coupling has been widely accepted, the magnetic phenomena in the nanocrystalline and nanocomposite magnets are not understood thoroughly. With the hot deformation of the single-phase melt-spun ribbons, desired texture could be developed in the magnets with an energy product approaching to  $\sim 50$  MGOe. However, no sufficient magnetically soft phase can be implanted into the magnetically hard phase matrix in order to form an anisotropic nanocomposite magnet with enhanced magnetic properties. Further studies are still required to understand the correlations between exchange coupling, thermal activation, and magnetic reversal in order to guide the future magnet design.

Although attempts to fabricate anisotropic nanocomposite bulk magnets have been made via hot deformation of the  $(\text{Nd, Pr, Dy})_2\text{Fe}_{14}\text{B}/\alpha\text{-Fe}$  nanocomposite materials, the energy product is still low. [291] Future success on the anisotropic nanocomposite magnets may be established on different technologies, but the main ideas are to align the magnetically hard phase and possibly increase the content of magnetically soft phase, while neither of them is technically easy. On the other hand, magnets with low cost always attract attention especially for industrial applications. Therefore, cheap *RE*-substituted magnets and even *RE*-free magnets should be a research topic as long as a trade-off on the magnetic properties is acceptable.

## References

- [1] Miroshnichenko I S and Salli I V 1959 *Ind. Laboratory* **25** 1463
- [2] Duwez P, Willens R H and Klement Jr W 1960 *J. Appl. Phys.* **31** 1136
- [3] Hirosawa S 2006 *Handbook Advanced Magn. Mater.* (Springer) p. 1064
- [4] Tsuei C C and Duwez P 1966 *J. Appl. Phys.* **37** 435
- [5] Luborsky F E 1983 *Amorphous Metallic Alloys* (Butterworth and Co: London, UK)
- [6] Herzer G 1989 *IEEE Trans. Magn.* **25** 3327
- [7] Yoshizawa Y and Yamauchi K 1990 *Mater. Trans. JIM* **31** 307
- [8] Croat J J, Herbst J F, Lee R W and Pinkerton F E 1984 *J. Appl. Phys.* **55** 2078
- [9] Sagawa M, Fujimura S, Togawa N, Yamamoto H and Matsuura Y 1984 *J. Appl. Phys.* **55** 2083
- [10] Stoner E C and Wohlfarth E P 1948 *Philos. Trans. R. Soc. London A: Math. Phys. Eng. Sci.* **240** 599
- [11] Manaf A, Zhang P Z, Ahmad I, Davies H A and Buckley R A 1993 *IEEE Trans. Magn.* **29** 2866
- [12] Schrefl T, Fidler J and Kronmüller H 1994 *Phys. Rev. B* **49** 6100
- [13] Kneller E F and Hawig R 1991 *IEEE Trans. Magn.* **27** 3588
- [14] Skomski R and Coey J M D 1993 *Phys. Rev. B* **48** 15812
- [15] Rong C B, Zhang H W, Chen R J, He S L and Shen B G 2006 *J. Magn. Magn. Mater.* **302** 126
- [16] Kronmüller H, Fischer R, Schrefl T and Fidler J 1996 *J. Magn. Magn. Mater.* **153** 35
- [17] Fischer R, Schrefl T, Kronmüller H and Fidler J 1995 *J. Magn. Magn. Mater.* **150** 329

- [18] Branagan D J and McCallum R W 1995 *J. Magn. Magn. Mater.* **146** 89
- [19] Marinescu M, Gabay A and Hadjipanayis G C 2007 *Handbook Magn. Advanced Magn. Mater.* **4**
- [20] Sagawa M, Hirotsawa S, Yamamoto H, Fujimura S and Matsuura Y 1987 *Jpn. J. Appl. Phys.* **26** 785
- [21] Tang Y L, Kramer M J, Dennis K W, McCallum R W and Lewis L H 2003 *J. Magn. Magn. Mater.* **267** 307
- [22] Zhang X F, Zhang W K, Li Y F, Liu Y L, Li Z B, Ma Q, Shi M F and Liu F 2016 *Rare Met.* **1**
- [23] Wang Z C, Davies H A and Zhou S Z 2002 *J. Appl. Phys.* **91** 3769
- [24] Li A H, Chiu C H, Chang H W, Chang W C and Li W 2007 *J. Alloys Compd.* **437** 197
- [25] Wu Q, Yu T, Guo S, Feng X C, Pan M X, Zhang P Y, Han B S, Ge H L and Yan A R 2012 *J. Appl. Phys.* **111** 07A730
- [26] Zhang W Y, Stoica M, Eckert J, Yu P and Jiang J Z 2008 *Intermetallics* **16** 341
- [27] Shen B G, Yang L Y and Guo H Q 1992 *Acta Phys. Sin.* **1** 57 (in Chinese)
- [28] Gutfleisch O 2000 *J. Phys. D: Appl. Phys.* **33** R157
- [29] Gutfleisch O, Bollero A, Handstein A, Hinz D, Kirchner A, Yan A, Muller K H and Schultz L 2002 *J. Magn. Magn. Mater.* **242** 1277
- [30] Sheng H C, Zeng X R, Hu Q and Deng F 2010 *J. Rare Earths* **28** 282
- [31] Shen B G, Yang L Y, Guo H Q and Zhao J G 1994 *J. Appl. Phys.* **75** 6312
- [32] Yang L Y, Shen B G, Zhang J X, Wo F, Ning T S, Zhao J G, Guo H Q and Zhan W S 1990 *J. Less Common Met.* **166** 189
- [33] Shen B G, Yang L Y, Guo H Q and Fu-ming Y 1992 *J. Magn. Magn. Mater.* **104** 2021
- [34] Yang L Y, Shen B G, Zhang J X, Zhao J G, Guo H Q and Fu-ming Y 1992 *J. Magn. Magn. Mater.* **104** 1191
- [35] Gu B X, Zhai H R and Shen B G 1990 *Phys. Rev. B* **42** 10648
- [36] Wang C, Yan M and Zhang W Y 2006 *J. Magn. Magn. Mater.* **306** 195
- [37] Shen B G, Zhang J X, Yang L Y, Wo F, Ning T S, Zhao J G, Guo H Q and Zhan W S 1991 *J. Less Common Met.* **167** 339
- [38] Gu B X, Shen B G and Zhai H R 2000 *J. Magn. Magn. Mater.* **218** 49
- [39] Hirotsawa S and Kanekiyo H 1996 *Mater. Sci. Eng. A* **217-218** 367
- [40] Zhang S Y, Xu H, Ni J S, Wang H L, Hou X L and Dong Y D 2007 *Phys. B: Condens. Matter* **393** 153
- [41] Gu B X, Shen B G, Methfessel S and Zhai H R 1989 *Solid State Commun.* **70** 933
- [42] Cheng Z H, Mao M X, Yang C L, Li F S, Shen B G, Zhang J X and Sun J J 1994 *J. Appl. Phys.* **76** 2981
- [43] Men K, Yu D, Luo Y, Jin J, Zhang K and Li K 2016 *AIP Adv.* **6** 025306
- [44] Zhang W and Inoue A 2002 *Appl. Phys. Lett.* **80** 1610
- [45] Pawlik P and Davies H A 2003 *Scr. Mater.* **49** 755
- [46] Marinescu M, Pawlik P C, Davies H A and Chiriac H 2004 *J. Optoelectronics Advanced Mater.* **6** 603
- [47] Cui X H, Liu Z W, Zhong X C, Yu H Y and Zeng D C 2012 *J. Appl. Phys.* **111** 07B508
- [48] Ormerod J 2015 *Magnetics Business & Technology* **8**
- [49] Zeng X R, Sheng H C, Zou J Z and Xie S H 2010 *Mater. Sci. Forum* **654** 1170
- [50] Narayan P, Van Vuong N, Rong C B and Liu J P 2011 *J. Phys. D: Appl. Phys.* **44** 335002
- [51] Liu J and Walmer M 2006 *Handbook Advanced Magnetic Materials*, Springer p. 1008
- [52] Lee Y I, Huang G Y, Chang S T, Shih C W, Chang W C, Chang H W and Chen Y J 2017 *IEEE Magn. Lett.* **8** 1
- [53] Li W, Wang H J, Lin M, Lai B, Li D and Pan W 2011 *J. Magn.* **16** 300
- [54] Saito T, Takeuchi T and Kageyama H 2004 *IEEE Trans. Magn.* **40** 2880
- [55] Yue M, Zhang J, Tian M and Liu X B 2006 *J. Appl. Phys.* **99** 08B502
- [56] Yue M, Zhang J, Xiao Y, Wang G and Li T 2003 *IEEE Trans. Magn.* **39** 3551
- [57] Yue M, Zhang J X, Liu W Q and Wang G P 2004 *J. Magn. Magn. Mater.* **271** 364
- [58] Rong C B, Nandwana V, Poudyal N, Liu J P, Saito T, Wu Y and Kramer M J 2007 *J. Appl. Phys.* **101** 09K515
- [59] Rao N V R, Gopalan R, Raja M M, Chandrasekaran V, Chakravarty D, Sundaresan R, Ranganathan R and Hono K 2007 *J. Magn. Magn. Mater.* **312** 252
- [60] Rong C, Zhang Y, Poudyal N, Wang D, Kramer M J and Liu J P 2011 *J. Appl. Phys.* **109** 07A735
- [61] Rong C B, Wu Y Q, Wang D, Zhang Y, Poudyal N, Kramer M J and Liu J P 2012 *J. Appl. Phys.* **111** 07A717
- [62] Chandramouli M, Thomas G and Nellis W J 1993 *J. Appl. Phys.* **73** 6494
- [63] Chen K H, Jin Z Q, Li J, Kennedy G, Wang Z L, Thadhani N N, Zeng H, Cheng S F and Liu J P 2004 *J. Appl. Phys.* **96** 1276
- [64] Jin Z Q, Thadhani N N, McGill M, Ding Y, Wang Z L, Chen M, Zeng H, Chakka V M and Liu J P 2005 *J. Mater. Res.* **20** 599
- [65] Noguchi M, Tomoshige R, Ikebe M, Kato A, Imamura K and Chiba A 1999 *J. Ceram. Soc. Jpn.* **107** 711
- [66] Jiang Y, Liu J, Suri P K, Kennedy G, Thadhani N N, Flannigan D J and Wang J P 2015 *Advanced Engineering Materials*
- [67] Ma B M, Lee D, Smith B, Gaiffi S, Owens B, Bie H and Warren G W 2001 *IEEE Trans. Magn.* **37** 2477
- [68] Mishra R K, Chu T Y and Rabenberg L K 1990 *J. Magn. Magn. Mater.* **84** 88
- [69] Li L and Graham Jr C D 1990 *J. Appl. Phys.* **67** 4756
- [70] Saito T, Fujita M, Kuji T, Fukuoka K and Syono Y 1998 *J. Appl. Phys.* **83** 6390
- [71] Hinz D, Kirchner A, Brown D N, Ma B M and Gutfleisch O 2003 *J. Mater. Process. Technol.* **135** 358
- [72] Dirba I, Sawatzki S and Gutfleisch O 2014 *J. Alloys Compd.* **589** 301
- [73] Bauer J, Seeger M, Zern A and Kronmüller H 1996 *J. Appl. Phys.* **80** 1667
- [74] Goll D, Seeger M and Kronmüller H 1998 *J. Magn. Magn. Mater.* **185** 49
- [75] Goll D and Kronmüller H 2000 *Naturwissenschaften* **87** 423
- [76] Hadjipanayis G C 1999 *J. Magn. Magn. Mater.* **200** 373
- [77] Pinkerton F E 1986 *J. Magn. Magn. Mater.* **54** 579
- [78] Hadjipanayis G C, Hazelton R C and Lawless K R 1983 *Appl. Phys. Lett.* **43** 797
- [79] Zhou Q Y, Liu Z, Guo S, Yan A R and Lee D 2015 *IEEE Trans. Magn.* **51** 1
- [80] Li Z B, Shen B G, Zhang M, Hu F X and Sun J R 2015 *J. Alloys Compd.* **628** 325
- [81] Zhang M, Li Z, Shen B, Hu F and Sun J 2015 *J. Alloys Compd.* **651** 144
- [82] Hussain M, Zhao L Z, Zhang C, Jiao D L, Zhong X C and Liu Z W 2016 *Phys. B: Condens. Matter* **483** 69
- [83] Buschow K H J 1997 *Handbook Magn. Mater.* **10** 463
- [84] Grössinger R, Krewenka R, Kou X C and Buschow K H J 1990 *J. Magn. Magn. Mater.* **83** 130
- [85] Buschow K H J 1988 *Handbook of Ferromagnetic Materials* **4** 1
- [86] Fidler J, Suess D and Schrefl T 2007 *Handbook of magnetism and advanced magnetic materials*
- [87] Fuerst C D, Herbst J F and Alson E A 1986 *J. Magn. Magn. Mater.* **54** 567
- [88] Wecker J and Schultz L 1987 *Appl. Phys. Lett.* **51** 697
- [89] Fuerst C D and Herbst J F 1988 *Appl. Phys. Lett.* **52** 1358
- [90] Fuerst C D, Herbst J F and Pinkerton F E 1988 *J. Appl. Phys.* **64** 5556
- [91] Coehoorn R, Duchateau J and Denissen C J M 1989 *J. Appl. Phys.* **65** 704
- [92] Zhang W Y, Zhang S Y and Shen B G 2002 *J. Alloys Compd.* **346** 269
- [93] Zhang W Y, Zhang J, Zhang S Y and Shen B G 2001 *J. Magn. Magn. Mater.* **234** 284
- [94] Zhang W Y, Rong C B, Zhang J, Shen B G, Du H I, Jiang J S and Yang Y C 2002 *J. Appl. Phys.* **92** 7647
- [95] Herbst J F, Fuerst C D, Mishra R K, Murphy C B and Van Wingerden D J 1991 *J. Appl. Phys.* **69** 5823
- [96] El-Moneim A A, Gebert A, Uhlemann M, Gutfleisch O and Schultz L 2002 *Corrosion Sci.* **44** 1857
- [97] Chen Z, Okumura H, Hadjipanayis G C and Chen Q 2001 *J. Alloys Compd.* **327** 201
- [98] Liu W, Liu Y, Skomski R and Sellmyer D J 2006 *Handbook of Advanced Magnetic Materials* (Springer) p. 182
- [99] Katter M, Wecker J, Kuhrt C, Schultz L and Grössinger R 1992 *J. Magn. Magn. Mater.* **117** 419
- [100] Strnat J K 1988 *Ferromagnetic Materials—a Handbook on the Properties of Magnetically Ordered Substances* North-Holland Physics Publishing, pp. 131–209
- [101] Takahashi M 1985 *J. Jpn. Inst. Met.* **49** 177
- [102] Ding J, McCormick P G and Street R 1995 *J. Alloys Compd.* **228** 102

- [103] Koppoju S, Chandrasekaran V and Gopalan R 2015 *AIP Adv.* **5** 077118
- [104] Yan A R, Zhang W Y, Zhang H W and Shen B G 2000 *J. Magn. Magn. Mater.* **210** 10
- [105] Coehoorn R and Duchateau J 1988 *Mater. Sci. Eng.* **99** 131
- [106] Zhang W Y, Shen B G, Cheng Z H, Li L, Zhou Y i and Li J Q 2001 *Appl. Phys. Lett.* **79** 1843
- [107] Li L, Zhang W Y, Zhou Y i, Li J Q, Shen B G and Zhang J 2002 *Appl. Phys. Lett.* **80** 2660
- [108] Tung I C, Zhang H W, Yao S Y, Shih J C, Shen B G and Chin T S 1999 *J. Phys. D: Appl. Phys.* **32** 1587
- [109] Yan A R, Zhang W Y, Zhang H W and Shen B G 2000 *J. Appl. Phys.* **88** 2787
- [110] Yan A R, Zhang W Y, Zhang H W and Shen B G 1999 *Mater. Sci. Eng.: B* **68** 111
- [111] Fukuzaki T, Iwane H, Abe K, Doi T, Tamura R and Oikawa T 2014 *J. Appl. Phys.* **115** 17A760
- [112] Saito H, Takahashi M and Wakiyama T 1987 *IEEE Trans. Magn.* **23** 2725
- [113] Gong W and Hadjipanayis G C 1996 *IEEE Trans. Magn.* **32** 4392
- [114] Fuerst C D, Herbst J F, Murphy C B and Van Wingerden D J 1993 *J. Appl. Phys.* **74** 4651
- [115] Du Z, Wang D and Zhang W 1999 *J. Alloys Compd.* **284** 206
- [116] Zhang W Y, Skomski R, Li X Z, Valloppilly S, Shield J and Sellmyer D J 2014 *J. Appl. Phys.* **115** 17A731
- [117] Fuerst C D and Brewer E G 1993 *J. Appl. Phys.* **74** 6907
- [118] Fuerst C D and Brewer E G 1994 *J. Appl. Phys.* **75** 6637
- [119] Yu H C, Li J Q, Bei Y Q, Zhou Y Q, Zhang J, Zhang W Y and Shen B G 2004 *J. Electron. Microscopy* **53** 37
- [120] Saito H, Takahashi M, Wakiyama T, Kido G and Nakagawa H 1989 *J. Magn. Magn. Mater.* **82** 322
- [121] Lefevre A, Cataldo L, Cohen-Adad M T and Mentzen B F 1997 *J. Alloys Compd.* **255** 161
- [122] Yang J, Mao O and Altounian Z 1996 *IEEE Trans. Magn.* **32** 4380
- [123] Guo Z H, Chang H W, Chang C W, Hsieh C C, Sun A C, Chang W C, Pan W and Li W 2009 *J. Appl. Phys.* **105** 07A731
- [124] Hsieh C C, Chang H W, Guo Z H, Chang C W, Zhao X G and Chang W C 2010 *J. Appl. Phys.* **107** 09A738
- [125] Hsieh C C, Shih C W, Liu Z, Chang W C, Chang H W, Sun A C and Shaw C C 2012 *J. Appl. Phys.* **111** 07E306
- [126] Feng D Y, Liu Z W, Zheng Z G, Zeng D C and Zhang G Q 2013 *J. Magn. Magn. Mater.* **347** 18
- [127] Du X B, Zhang H W, Rong C B, Zhang J, Zhang S Y, Shen B G, Yan Y and Jin H M 2003 *J. Phys. D: Appl. Phys.* **36** 2432
- [128] Rong C B, Zhang H W, Du X B, Zhang J, Zhang S Y and Shen B G 2004 *J. Rare Earths* **22** 161
- [129] Hsiao A, Aich S, Lewis L H and Shield J E 2004 *IEEE Trans. Magn.* **40** 2913
- [130] Li L and Xie W 2011 *Journal of Metallurgy*
- [131] Makridis S S, Litsardakis G, Panagiotopoulos I, Niarchos D, Zhang Y and Hadjipanayis G C 2002 *IEEE Trans. Magn.* **38** 2922
- [132] Kim D H and Hadjipanayis G C 1998 *J. Magn. Magn. Mater.* **190** 240
- [133] Zhang J, Wang F, Rong C B, Zhang H W, Zhang S Y and Shen B G 2003 *J. Appl. Phys.* **93** 9170
- [134] Zhang J, Shen B G, Zhang S Y, Wang Y Q and Duan X F 2002 *Appl. Phys. Lett.* **80** 1418
- [135] Kostogorova J and Shield J E 2006 *J. Appl. Phys.* **99** 08B514
- [136] Yan A R, Zhang W Y, Zhang H W and Shen B G 2000 *Mater. Sci. Eng. B* **76** 169
- [137] Yan A R, Sun Z G, Zhang W Y, Zhang H W and Shen B G 2000 *Appl. Phys. A* **71** 311
- [138] Chen C H, Kodat S, Walmer M H, Cheng S F, Willard M A and Harris V G 2003 *J. Appl. Phys.* **93** 7966
- [139] Yan A, Bollero A, Müller K H and Gutfleisch O 2002 *J. Appl. Phys.* **91** 8825
- [140] Crabbe M W, Davies H A and Buckley R A 1994 *IEEE Trans. Magn.* **30** 696
- [141] Coey J M D and Sun H 1990 *J. Magn. Magn. Mater.* **87** L251
- [142] Pinkerton F E and Fuerst C D 1992 *Appl. Phys. Lett.* **60** 2558
- [143] Katter M, Wecker J and Schultz L 1991 *J. Appl. Phys.* **70** 3188
- [144] Moukarika A, Papaefthymiou V, Bakas T, Psycharis V and Niarchos D 1996 *J. Magn. Magn. Mater.* **163** 109
- [145] Shield J E, Branagan D J, Li C P and McCallum R W 1998 *Faculty Publications from Nebraska Center for Materials and Nanoscience* **46**
- [146] Omatsuzawa R, Murashige K and Iriyama T 2004 *Trans. Magn. Soc. Jpn.* **4** 113
- [147] Cao L, Kong L S and Shen B G 1992 *J. Phys.: Condens. Matter* **4** L515
- [148] Kong L S, Cao L and Shen B G 1993 *J. Alloys Compd.* **191** 301
- [149] Cao L, Kong L S and Shen B G 1993 *J. Appl. Phys.* **73** 5887
- [150] Li F, Sun J, Xue D, Zhang X, Ge S, Zhang Y, Mao M, Shen B, Kong L and Cao L 1993 *J. Appl. Phys.* **73** 5893
- [151] Cao L, Kong L S and Shen B G 1993 *J. Phys.: Condens. Matter* **5** 2001
- [152] Kong L S, Shen B G, Cao L, Gong H Y and Chen Y L 1993 *J. Phys.: Condens. Matter* **5** 2415
- [153] Gong H Y, Shen B G, Kong L S, Cao L, Zhan W S, Cheng Z H and Wang F W 1994 *J. Appl. Phys.* **76** 6711
- [154] Shen B G, Kong L S, Cao L, Gong H Y, Wang F W, Cheng Z H and Zhao J G 1994 *J. Appl. Phys.* **76** 6714
- [155] Shen B G, Cao L, Guo H Q, Zhang J X, Kong L S, Gong H Y and Cheng Z H 1995 *J. Alloys Compd.* **222** 123
- [156] Kong L S, Shen B G, Cao L, Wang F W, Zhao J G, Zhang Z, Gong H Y and Chen Y L 1993 *Acta Phys. Sin.* **42** 1696 (in Chinese)
- [157] Shen B G, Kong L S, Cao L, Gong H Y, Wang F W, Zhan W S, Guo H Q and Zhao J G 1993 *Acta Phys. Sin.* **42** 1998 (in Chinese)
- [158] Shen B G, Wang F W, Kong L S and Cao L 1993 *J. Phys.: Condens. Matter* **5** L685
- [159] Shen B G, Kong L S, Wang F W and Cao L 1993 *Appl. Phys. Lett.* **63** 2288
- [160] Shen B G, Wang F W, Kong L S, Cao L and Zhan W S 1994 *J. Appl. Phys.* **75** 6253
- [161] Cheng Z H, Shen B G, Zhang J X, Gong H Y and Zhao J G 1994 *J. Phys.: Condens. Matter* **6** L185
- [162] Shen B G, Zhang H W, Zhang S Y and Cheng Z H 1999 *Advanced Mater.* **11** 1110
- [163] Shen B G, Liang B, Wang F W, Cheng Z H, Gong H Y, Guo H Q, Zhao J G and Zhang Z Y 1995 *Solid State Commun.* **95** 547
- [164] Shen B G, Gong H Y, Cheng Z H, Wang F W, Liang B, Kong L S, Guo H Q, Zhan W S and Zhao J G 1995 *J. Magn. Magn. Mater.* **151** 111
- [165] Cheng Z H, Shen B G, Wang F W, Zhang J X, Gong H Y and Zhan W S 1995 *J. Phys.: Condens. Matter* **7** 3195
- [166] Zhang S Y, Zhang H W, Shen B G and Chin T S 1998 *J. Phys. D: Appl. Phys.* **31** 3337
- [167] Zhang H W, Zhang W Y, Sun Z G, Yan A R and Shen B G 2001 *Mater. Sci. Eng.: A* **304** 965
- [168] Shen B G, Wang F W, Cheng Z H, Gong H Y, Liang B and Zhang J X 1995 *J. Magn. Magn. Mater.* **140** 975
- [169] Yan Q W, Zhang P L, Sun X D, Shen B G, Wang F W, Kong L S, Gou C, Chen D F and Cheng Y F 1994 *J. Phys.: Condens. Matter* **6** 3567
- [170] Wang F W, Kong L S, Cao L, Hu M, Shen B G and Zhao J G 1994 *J. Appl. Phys.* **75** 7111
- [171] Shen B G, Wang F W, Kong L S, Cao L, Zhang B and Zhao J G 1994 *J. Appl. Phys.* **75** 6259
- [172] Cheng Z H, Mao M X, Sun J J, Shen B G, Wang F W, Yang C L, Zhang Y D and Li F S 1995 *J. Phys.: Condens. Matter* **7** 2303
- [173] Shen B G, Gong H Y, Cheng Z H, Kong L S, Wang F W, Liang B, Zhang J X, Guo H Q and Zhao J G 1996 *J. Magn. Magn. Mater.* **153** 332
- [174] Zhang S Y, Sun Z G, Zhang H W, Han B S, Shen B G, De Boer F R and Buschow K H J 1999 *J. Phys. D: Appl. Phys.* **32** 2990
- [175] Zhang S Y, Sun Z G, Zhang H W, Han B S, Shen B G, De Boer F R and Buschow K H J 1999 *Appl. Phys. Lett.* **75** 546
- [176] Ahmad Z, Tao S, Ma T, Zhao G and Yan M 2011 *J. Alloys Compd.* **509** 8952
- [177] Zhang H W, Zhang S Y, Shen B G and Zhang L G 1998 *J. Appl. Phys.* **83** 4838
- [178] Wang Y, Hadjipanayis G C, Kim A, Liu N C and Sellmyer D J 1990 *J. Appl. Phys.* **67** 4954
- [179] Okada M, Kojima A, Yamagishi K and Homma M 1990 *IEEE Trans. Magn.* **26** 1376
- [180] Sugimoto S, Kojima A, Okada M and Homma M 1991 *Mater. Trans. JIM* **32** 1180
- [181] Tang Z X, Singleton E W and Hadjipanayis G C 1993 *J. Appl. Phys.* **73** 6254
- [182] Yang J and Yang Y 2006 *Journal of alloys and compounds* (Springer) p. 1414

- [183] Hadjipanayis G C, Zheng Y H, Murthy A S, Gong W and Yang F M 1995 *J. Alloys Compd.* **222** 49
- [184] Chen Z, Teo G, Brown D and Miller D 2008 *J. Appl. Phys.* **103** 07E128
- [185] Rani R, Hegde H, Navarathna A, Chen K and Cadieu F J 1992 *IEEE Trans. Magn.* **28** 2835
- [186] Saito T 2008 *Mater. Trans.* **49** 1446
- [187] Saito T, Miyoshi H and Nishio-Hamane D 2012 *J. Appl. Phys.* **111** 07E322
- [188] Guo X, Chen X, Altounian Z and Ström-Olsen J O 1992 *Phys. Rev. B* **46** 14578
- [189] Saha S, Obermyer R T, Zande B J, Chandhok V K, Simizu S, Sankar S G and Horton J A 2002 *J. Appl. Phys.* **91** 8525
- [190] Yang J B, Yang Y B, Chen X G, Ma X B, Han J Z, Yang Y C, Guo S, Yan A R, Huang Q Z, Wu M M and Chen D F 2011 *Appl. Phys. Letter* **99** 082505
- [191] Cui J, Choi J P, Li G, Polikarpov E, Darsell J, Overman N, Olszta M, Schreiber D, Bowden M and Droubay T 2014 *J. Phys.: Condens. Matter* **26** 064212
- [192] Kharel P, Shah V R, Li X Z, Zhang W Y, Skomski R, Shield J E and Sellmyer D J 2013 *J. Phys. D: Appl. Phys.* **46** 095003
- [193] Balamurugan B, Das B, Zhang W Y, Skomski R and Sellmyer D J 2014 *J. Phys.: Condens. Matter* **26** 064204
- [194] Zhang W Y, Li X Z, Valloppilly S, Skomski R, Shield J E and Sellmyer D J 2013 *J. Phys. D: Appl. Phys.* **46** 135004
- [195] McGuire M A, Rios O, Ghimire N J and Koehler M 2012 *Appl. Phys. Lett.* **101** 202401
- [196] Zhang W, Ma D, Li Y, Yubuta K, Liang X and Peng D 2014 *J. Alloys Compd.* **615** S252
- [197] Liu Z W, Chen C, Zheng Z G, Tan B H and Ramanujan R V 2012 *J. Mater. Sci.* **47** 2333
- [198] Löwe K, Dürrschnabel M, Molina-Luna L, Madugundo R, Frincu B, Kleebe H J, Gutfleisch O and Hadjipanayis G C 2016 *J. Magn. Magn. Mater.* **407** 230
- [199] Coehoorn R, De Mooij D B, Duchateau J and Buschow K H J 1988 *Le Journal De Physique Colloques* **49** C8
- [200] Coehoorn R, de Mooij D B and de Waard C 1989 *J. Magn. Magn. Mater.* **80** 101
- [201] Coehoorn R and De Waard C 1990 *J. Magn. Magn. Mater.* **83** 228
- [202] Shen B G, Zhang J X, Yang L, Wo F, Ning T S, Ji S Q, Zhao J G, Guo H Q and Zhan W S 1990 *J. Magn. Magn. Mater.* **89** 195
- [203] Shen B G, Yang L Y, Zhang J X, Gu B X, Tai-shan N, Wo F, Zhao J G, Guo Hui q and Wen-shan Z 1990 *Solid State Commun.* **74** 893
- [204] Shen B G, Yang L, Zhang J X, Wo F, Ning T S, Zhao J G, Guo H Q and Zhan W s 1991 *J. Magn. Magn. Mater.* **96** 335
- [205] Bader S D 2006 *Rev. Mod. Phys.* **78** 1
- [206] Kim H T, Kim Y B and Park W S 2002 *J. Magn. Magn. Mater.* **239** 430
- [207] Cheng Z H, Shen B G, Mao M X, Sun J J and Li F S 1995 *Phys. Rev. B* **52** 9427
- [208] Kanekiyo H and Hirosawa S 1998 *J. Appl. Phys.* **83** 6265
- [209] Xiao Q F, Zhao T, Zhang Z D, Brück E, Buschow K H J and de Boer F R 2001 *J. Magn. Magn. Mater.* **223** 215
- [210] Yang C J, Park E B, Hwang Y S and Kim E C 2000 *J. Magn. Magn. Mater.* **212** 168
- [211] Kanekiyo H, Uehara M and Hirosawa S 1993 *IEEE Trans. Magn.* **29** 2863
- [212] Ping D H, Hono K, Kanekiyo H and Hirosawa S 1999 *Acta Mater.* **47** 4641
- [213] Rajasekhar M, Akhtar D, Ram S, Ghoshray A and Bandyopadhyay B 2008 *AIP Conf. Proc.* **1003** 52
- [214] Cheng Z H, Shen B G, Zhang F W, Cao L, Zhao J G, Zhan W S, Mao M X, Sun J J and Li F S 1995 *Phys. Rev. B* **51** 12433
- [215] Davies H A, Manaf A, Leonowicz M, Zhang P Z, Dobson S J and Buckley R A 1993 *Nanostructured Mater.* **2** 197
- [216] Manaf A, Buckley R A and Davies H A 1993 *J. Magn. Magn. Mater.* **128** 302
- [217] Betancourt R J I and Davies H A 1999 *J. Appl. Phys.* **85** 5911
- [218] Zhang W Y, Zhang S Y, Yan A R, Zhang H W and Shen B G 2001 *J. Magn. Magn. Mater.* **225** 389
- [219] Wang Z, Zhang M, Li F, Zhou S, Wang R and Gong W 1997 *J. Appl. Phys.* **81** 5097
- [220] Chang W C, Chiou D Y, Wu S H, Ma B M and Bounds C O 1998 *Appl. Phys. Lett.* **72** 121
- [221] Chang W C, Chang J K, Chang H W and Chen S K 2003 *Phys. B: Condens. Matter* **327** 296
- [222] Chen Z, Wu Y Q, Kramer M J, Smith B R, Ma B M and Huang M Q 2004 *J. Magn. Magn. Mater.* **268** 105
- [223] Zhang W Y, Kharel P, Al-Omari I A, Shield J E and Sellmyer D J 2016 *Philos. Mag.* **96** 2800
- [224] Zhang P Y, Hiergeist R, Albrecht M, Braun K F, Sievers S, Lüdke J and Ge H L 2009 *J. Appl. Phys.* **106** 073904
- [225] Zeng X R, Sheng H C, Deng F and Liu J 2009 *Phys. B: Condens. Matter* **404** 3739
- [226] Hashino H, Tazaki Y, Ino H, Ohkubo T and Hono K 2004 *J. Magn. Magn. Mater.* **278** 68
- [227] Liu J F and Davies H A 1996 *Journal of magnetism and magnetic materials* **157** 29
- [228] Ji Q G, Gu B X and Du Y W 2000 *J. Appl. Phys.* **88** 7230
- [229] Ma Y L, Shen Q, Liu X B, Qiu Y, Li C H, Zhou A R, Sun J C and Chen D M 2014 *J. Appl. Phys.* **115** 17A704
- [230] Van Nguyen V, Rong C, Ding Y and Liu J P 2012 *J. Appl. Phys.* **111** 07A731
- [231] Nguyen X T, Vu H K, Do H M, Nguyen V K and Nguyen V V 2013 *Advances in Materials Science and Engineering* **2013**
- [232] Mendoza-Suarez G and Davies H A 1998 *J. Alloys Compd.* **281** 17
- [233] Wang Z, Zhou S, Zhang M and Qiao Y 2000 *J. Appl. Phys.* **88** 591
- [234] Chen Z, Okumura H, Hadjipanayis G C and Chen Q 2001 *J. Appl. Phys.* **89** 2299
- [235] Zhang W Y, Yan A R, Zhang H W and Shen B G 2001 *J. Alloys Compd.* **315** 174
- [236] Chang H W, Chiu C H, Chang C W, Chen C H, Chang W C, Yao Y D and Sun A C 2006 *J. Alloys Compd.* **407** 53
- [237] Yang B, Shen B G, Zhao T Y and Sun J R 2007 *Mater. Sci. Eng. B* **145** 11
- [238] Yang B, Shen B G, Zhao T Y and Sun J R 2008 *J. Magn. Magn. Mater.* **320** 2406
- [239] Zhang W Y, Zhang J, Cheng Z H, Zhang S Y and Shen B G 2001 *J. Phys.: Condens. Matter* **13** 3859
- [240] Mendoza-Suarez G, Davies H A and Escalante-Garcia J I 2000 *J. Magn. Magn. Mater.* **218** 97
- [241] Cheng Z H, Zhang J X, Guo H Q, Van Lier J, Kronmüller H and Shen B G 1998 *Appl. Phys. Lett.* **72** 1110
- [242] Cheng Z H, Kronmüller H and Shen B G 1998 *Appl. Phys. Lett.* **73** 1586
- [243] Zhang H W, Zhang S Y, Shen B G and Lin C 1999 *J. Appl. Phys.* **85** 4660
- [244] Zhang X Y, Zhang J W and Wang W K 2001 *J. Appl. Phys.* **89** 477
- [245] Liu J F and Walmer M H 2005 *IEEE Trans. Electron. Devices* **52** 899
- [246] Liu J F, Chui T, Dimitrov D and Hadjipanayis G C 1998 *Appl. Phys. Lett.* **73** 3007
- [247] Liu S, Yang J, Doyle G, Potts G and Kuhl G E 2000 *J. Appl. Phys.* **87** 6728
- [248] Liu S S 2006 *Handbook of Advanced Magnetic Materials* (Springer) p. 1329
- [249] Goll D, Kleinschroth I, Sigle W and Kronmüller H 2000 *Appl. Phys. Lett.* **76** 1054
- [250] Yan A, Bollero A, Müller K H and Gutfleisch O 2002 *Appl. Phys. Lett.* **80** 1243
- [251] Yan A, Gutfleisch O, Gemming T and Müller K H 2003 *Appl. Phys. Lett.* **83** 2208
- [252] Rong C B, Zhang H W, Zhang J, Du X B, Zhang S Y and Shen B G 2005 *J. Appl. Phys.* **97** 033907
- [253] Rong C B, He S L, Chen R J, Zhang H W and Shen B G 2005 *Chin. Phys. B* **14** 2122
- [254] Rong C B, Zhang H W, He S L, Chen R J and Shen B G 2005 *Appl. Phys. Lett.* **86** 122506
- [255] Rong C B, Zhang H W, Chen R J, Shen B G, He S L and Liu J P 2006 *J. Phys. D: Appl. Phys.* **39** 437
- [256] Rong C, Zhang Y, Poudyal N, Xiong X, Kramer M J and Liu J P 2010 *Appl. Phys. Lett.* **96** 102513
- [257] Rong C, Zhang Y, Poudyal N, Szlufarska I, Hebert R J, Kramer M J and Liu J P 2011 *J. Mater. Sci.* **46** 6065
- [258] Zhang H W, Zhao T Y, Rong C B, Zhang S Y, Han B S and Shen B G 2003 *J. Magn. Magn. Mater.* **267** 224
- [259] Zhao G P, Ong C K, Feng Y P, Lim H S and Ding J 1999 *J. Magn. Magn. Mater.* **192** 543

- [260] Schrefl T, Fidler J and Kronmüller H 1994 *Phys. Rev. B* **49** 6100
- [261] Rong C B, Zhang H W, Chen R J, He S L, Zhang S Y and Shen B G 2004 *Acta Phys. Sin.* **53** 4353 (in Chinese)
- [262] Zhang H W, Rong C B, Du X B, Zhang J, Zhang S Y and Shen B G 2003 *Appl. Phys. Lett.* **82** 4098
- [263] Rong C B, Nandwana V, Poudyal N, Liu J P, Kozlov M E, Baughman R H, Ding Y and Wang Z L 2007 *J. Appl. Phys.* **102** 023908
- [264] Rong C B, Li D, Nandwana V, Poudyal N, Ding Y, Wang Z L, Zeng H and Liu J P 2006 *Advanced Mater.* **18** 2984
- [265] Rong C B, Liu Y and Liu J P 2008 *Appl. Phys. Lett.* **93** 042508
- [266] Rong C B and Liu J P 2009 *J. Appl. Phys.* **105** 07A714
- [267] Rong C B and Liu J P 2009 *Appl. Phys. Lett.* **94** 172510
- [268] Zheng B, Zhang H W, Zhao S F, Chen J L and Wu G H 2008 *Appl. Phys. Lett.* **93** 182503
- [269] Li Z B, Shen B G and Sun J R 2013 *J. Appl. Phys.* **113** 013902
- [270] Pike C R, Roberts A P and Verosub K L 1999 *J. Appl. Phys.* **85** 6660
- [271] Roberts A P, Pike C R and Verosub K L 2000 *J. Geophys. Res.: Solid Earth* **105** 28461
- [272] Rong C B, Zhang Y, Kramer M J and Liu J 2011 *Phys. Lett. A* **375** 1329
- [273] Rodewald W 2007 *Handbook of Magnetism and Advanced Magnetic Materials*
- [274] Zhang H W, Rong C B, Zhang J, Zhang S Y and Shen B G 2002 *Phys. Rev. B* **66** 184436
- [275] Rong C B, Zhang J, Du X B, Zhang H W, Zhang S Y and Shen B G 2004 *Chin. Phys. B* **13** 1144
- [276] Rong C B, Zhang J, Zhang H W, Du X B, Zhang S Y and Shen B G 2004 *J. Magn. Mater.* **279** 143
- [277] Rong C B, Chen R J, Zhang H W, Jian Z, Zhang S Y and Shen B G 2004 *J. Phys. D: Appl. Phys.* **37** 3285
- [278] Kronmüller H, Durst K D and Martinek G 1987 *J. Magn. Magn. Mater.* **69** 149
- [279] Martinek G and Kronmüller H 1990 *J. Magn. Magn. Mater.* **86** 177
- [280] Kronmüller H 1987 *Phys. Status Solidi (b)* **144** 385
- [281] Kronmüller H, Durst K D and Sagawa M 1988 *J. Magn. Magn. Mater.* **74** 291
- [282] Zhang H W, Sun Z G, Zhang S Y, Han B S, Shen B G, Tung I C and Chin T S 1999 *Phys. Rev. B* **60** 64
- [283] Zhang H W, Li B H, Wang J, Zhang J, Zhang S Y and Shen B G 2000 *J. Phys. D: Appl. Phys.* **33** 3022
- [284] Cammarano R, McCormick P G and Street R 1996 *J. Phys. D: Appl. Phys.* **29** 2327
- [285] Li Z B, Zhang M, Wang L C, Shen B G, Zhang X F, Li Y F, Hu F X and Sun J R 2014 *Appl. Phys. Lett.* **104** 052406
- [286] Crew D C, McCormick P G and Street R 1999 *J. Appl. Phys.* **86** 3278
- [287] Crew D C, McCormick P G and Street R 1999 *Appl. Phys. Lett.* **74** 591
- [288] Crew D C, Woodward R C and Street R 1999 *J. Appl. Phys.* **85** 5675
- [289] Rong C B, Zhang H W, Shen B G and Liu J P 2006 *Appl. Phys. Lett.* **88** 042504
- [290] Rong C B, Zhang H W, Chen R J, Shen B G and He S L 2006 *J. Appl. Phys.* **100** 123913
- [291] Lee D, Hilton J S, Liu S, Zhang Y, Hadjipanayis G C and Chen C H 2003 *IEEE Trans. Magn.* **39** 2947